



NASA TM-78739

NASA Technical Memorandum 78739

NASA-TM-78739 19790019967

THE EFFECT OF CANARD RELATIVE SIZE AND VERTICAL LOCATION ON  
THE SUBSONIC LONGITUDINAL AND LATERAL-DIRECTIONAL STATIC  
AERODYNAMIC CHARACTERISTICS FOR A MODEL WITH A SWEPT FORWARD WING

JARRETT K. HUFFMAN AND CHARLES H. FOX, JR.

FOR INFORMATION

NOT TO BE TAKEN FROM THIS ROOM

July 1979

LIBRARY COPY

1979

LANGLEY RESEARCH CENTER  
LIBRARY, NASA  
HAMPTON, VIRGINIA



National Aeronautics and  
Space Administration

Langley Research Center  
Hampton, Virginia 23665





## INTRODUCTION

In the late 1940's, as aircraft speeds were approaching Mach one, investigations were conducted to evaluate swept forward and swept back wings as a means of delaying the onset of transonic compressibility effects. (See references 1-3). Sweeping the wings, either forward or back, delayed the drag rise to a higher Mach number; however, an aeroelastic divergence problem was found to be associated with swept forward wings. (See references 4 and 5.) This structural instability problem could be eliminated, but the resulting swept forward wing was significantly heavier than a corresponding swept back wing. As a consequence of this fact, most of the subsequent research was concentrated on swept back wings.

Recently, research interest in forward sweep has been renewed. This is partly a result of studies, such as reference 6, which indicate that proper tailoring of composite materials may produce a divergence-free swept forward wing with minimal weight penalty. Forward sweep is being studied in relation to a variety of configurations. When applied to fighter aircraft, the forward sweep concept offers a possible potential for improved transonic maneuver performance.

Experimental studies have been initiated to expand the existing data base on swept forward wings. (See references 7 and 8.) The present study was conducted to obtain the effect on static aerodynamic characteristics of the relative size and vertical location of a swept back canard in combination with a swept forward wing.

It should be noted that the model was built up from wing and canard model parts previously constructed for swept back configurations. These lifting surfaces had circular arc airfoil sections which allowed their use in the reversed or forward sweep condition. It should be also noted that, because of the flow separation at the sharp leading edges, the present data will be generally more applicable to the study of the high angle-of-attack characteristics.

The tests were performed in the Langley 7- by 10-foot high speed tunnel at a Mach number of 0.3. The angle-of-attack range was from approximately  $-4^{\circ}$  to  $48^{\circ}$  at sideslip angles of  $0^{\circ}$ ,  $-5^{\circ}$ , and  $5^{\circ}$ .

## SYMBOLS

The International System of Units, with the U.S. Customary Units presented in parenthesis, is used for the physical quantities in this report (See reference 9). The measurements and calculations were made in the U.S. Customary Units. The data presented in this report are referred to the stability axis system. The reference center for moments is shown in Figure 1(a).

b	wing reference span, .508 m (20.000 in.)
$\bar{c}$	wing reference chord, .233 m (9.185 in.)
$C_D$	total drag coefficient, $\frac{\text{Total Drag}}{qS}$
$C_{D_2}$	nose drag coefficient, $\frac{\text{Nose Drag}}{qS}$
$C_L$	total lift coefficient, $\frac{\text{Total Lift}}{qS}$
$C_{L_2}$	nose lift coefficient, $\frac{\text{Nose Lift}}{qS}$
$C_{\ell}$	total rolling moment coefficient, $\frac{\text{Total Rolling moment}}{qSb}$
$C_{\ell_2}$	nose rolling moment coefficient, $\frac{\text{Nose Rolling moment}}{qSb}$
$C_{\ell_\beta}$	beta derivative of total rolling moment coefficient computed between $\beta = 5^\circ$ and $\beta = -5^\circ$ .
$C_{\ell_{\beta_2}}$	beta derivative of nose rolling moment coefficient computed between $\beta = 5^\circ$ and $\beta = -5^\circ$ .

$C_m$	total pitching moment coefficient, $\frac{\text{Total Pitching moment}}{qS\bar{c}}$
$C_{m_2}$	nose pitching moment coefficient, $\frac{\text{Nose Pitching moment}}{qS\bar{c}}$
$C_n$	total yawing moment coefficient, $\frac{\text{Total Yawing moment}}{qSb}$
$C_{n_2}$	nose yawing moment coefficient, $\frac{\text{Nose Yawing moment}}{qSb}$
$C_{n\beta}$	beta derivative of total yawing moment coefficient computed between $\beta = 5^\circ$ and $\beta = -5^\circ$
$C_Y$	total side force coefficient, $\frac{\text{Total Side force}}{qS}$
$C_{Y_2}$	nose side force coefficient, $\frac{\text{Nose Side force}}{qS}$
$C_{Y\beta}$	beta derivative of total side force coefficient computed between $\beta = 5^\circ$ and $\beta = -5^\circ$
$C_{Y\beta_2}$	beta derivative of nose side force coefficient computed between $\beta = 5^\circ$ and $\beta = -5^\circ$
$M$	free stream Mach number
$q$	free stream dynamic pressure, Pa (lb/ft <sup>2</sup> )
$S$	wing reference area, .1032 m <sup>2</sup> (1.11109 ft <sup>2</sup> )
$\alpha$	angle of attack of the model, degrees
$\alpha_2$	angle of attack of the fuselage nose, degrees
$\beta$	angle of sideslip of the model, degrees
$\beta_2$	angle of sideslip of the fuselage nose, degrees

## DESCRIPTION OF MODEL

Drawings of the model tested are presented in Figure 1. Photographs of the model installed in the 7- by 10-foot high speed tunnel are presented in Figure 2. The basic model consisted of a main fuselage with a vertical tail and a wing and a fuselage nose with a canard. The main fuselage was sting mounted on a six-component strain gage main balance which measured the total forces and moments on the configuration. The fuselage nose section was mounted on a six component strain gage nose balance which measured only the forces and moments on the nose and canard. The metric break is shown in figure 1.

The uncambered and untwisted wing, canard, and vertical tail employed circular arc airfoil sections with a thickness ratio of 6 percent at the fuselage juncture and 4 percent at the tip. The wing had a sharp leading edge with a nominal forward sweep of  $32^\circ$ . (See figure 1(d)). Figure 1(a) shows the high-, mid, and low-wing positions. The fuselage was modified to a locally rectangular upper or lower section for the high- or low-wing positions so that the span was equal to the mid-wing span. The canards had sharp leading edges with a nominal aft sweep of  $51.7^\circ$ . (See Figure 1(e)). Figure 1(b) shows the high-, mid-, and low-canard positions of the medium size canard and the high position of the large size canard. The fuselage was modified to a locally rectangular upper or lower section for the high- or low-canard positions so that the span was equal to the mid-canard span. Figure 1(c) shows the mid position of the medium and small size canards. The exposed areas of the canards were 15.8, 22.2, and 28.7 percent of the wing reference area. The centerline mounted vertical tail had a  $51.7^\circ$  swept sharp leading edge and had an exposed area of 14 percent of the wing reference area. (See Figure 1(f)).

## APPARATUS, TESTS, AND CORRECTIONS

The investigation was conducted in the Langley 7- by 10-foot high speed tunnel in the solid wall test section configuration (See reference 10). Forces and moments were measured on two six component strain gage balances mounted internally in the model. The test was run at a Mach number of 0.3 corresponding to a Reynolds number of  $1.4 \times 10^6$  based on the wing reference chord. The model was tested over an angle of attack range from  $-4^\circ$  to approximately  $48^\circ$  at sideslip angles of  $0^\circ$ , and  $\pm 5^\circ$ . The angles of attack and sideslip have been corrected for the effects of sting and balance bending under load. It should be noted that the sting support system which permits testing over this large angle range is designed specifically for stability testing. This sting mechanism incorporates a large structure downstream of the model (see fig. 2). It is felt that this large body behind the model may cause a change in the pressure on the outer lines of the aft fuselage. Therefore the level of the drag data may be questionable for use in performance analysis.

Jet boundary and blockage corrections have been applied to the data based on references 11 and 12, respectively. The main balance chamber pressure was measured and the total drag measurements were adjusted to a condition of free-stream static pressure acting over the base of the model. The nose balance base and chamber pressure were also measured and the nose drag measurements were adjusted to a condition of free stream static pressure acting at the base of the nose. Transition strips 0.16 cm (.0625 in.) in width of No. 120 Carborundum grains were placed 2.54 cm (1.0 in.) aft of the leading edge of the wings, canards, and vertical tail as well as 3.05 cm (1.2 in.) aft of the nose of the fuselage (reference 13).

## PRESENTATION OF RESULTS

The longitudinal and lateral-directional aerodynamic characteristics at  $0^\circ$  sideslip are presented in the following figures:

	<u>Figure</u>
Effect of wing height	3
Effect of canard height	4
Effect of component breakdown with low canard	5
Effect of component breakdown with high canard	6
Effect of Mid-canard size	7
Effect of High-canard size	8
Lift interference effect for the high and low canard position	22

The lateral-directional aerodynamic stability derivative characteristics are presented in the following figures:

	<u>Figure</u>
Effect of wing height	9
Effect of canard height	10
Effect of component breakdown with low canard	11
Effect of component breakdown with high canard	12
Effect of mid-canard size	13

Surface oil flow photographs at  $0^\circ$  sideslip are presented in the following figures:

	<u>Figure</u>
Basic mid-wing	14
Basic high-wing	15
Basic low-wing	16
Basic medium size high-canard	17
Basic medium size low-canard	18
Mid-wing small size mid-canard	19
Mid-wing large size high-canard	20
Mid-wing large size low-canard	21

Note that no force measurements were obtained on the configuration presented in figure 21.



## DISCUSSION

The fuselage used for this investigation was designed to allow versatility in model geometry and is used in a number of general research programs. Therefore, this fuselage does not represent the fuselage of an actual high performance aircraft. Also the wing, horizontal and vertical tails have biconvex airfoil sections with sharp leading and trailing edges which would be expected to result in leading edge separation at relatively low angles of attack. The data, however should be of interest with regard to component interference effects particularly in the high angle of attack range encountered by maneuvering aircraft.

### Longitudinal and Lateral-Directional Characteristics

The effect of wing vertical location on the aerodynamic characteristics is shown in figure 3. The data indicate that only above 30 degrees angle of attack is there any appreciable effect and these effects are limited to the high-wing location configuration. The noted effects may be caused by the juncture of the wing and fuselage (see oil flow pictures, Figures 14, 15, and 16). The data along with the oil flow information show that because of the sharp leading edge, separation along the leading edge is generally independent of wing vertical location.

Figure 4 shows the effect of medium-size canard vertical location on the aerodynamic characteristics of the configuration utilizing the mid-wing location. The data show that the canard in the high position produces the maximum canard lift (see Figure 4(b)) and has a more linear pitching moment coefficient versus angle of attack. These effects are seen also in the total aerodynamic characteristics of the configuration (see figure 4(a)) as

higher total lift and more linear pitching moment. The loss in lift of the canard in the low position is most probably caused by the reduced body induced upwash and a loss of carry-over lift on the body.

The effect of model component on the aerodynamic characteristics for the low- and high-canard position utilizing the mid-wing location configuration are shown in Figure 5 and 6, respectively, and summarized in Figure 22 as interference effects. The data in Figure 22 show that the canard lift increment for the high canard in the presence of the wing is considerably larger than that for the low canard. However, both canard positions exhibited adverse effects on the wing and after-body lift at low angle of attack which diminished at high angles. Favorable interference effects of the wing on the high canard are noted, but in general, no favorable effects were noted for the low canard. These general trends were also reported in reference 14 for a configuration utilizing a swept-back wing and a swept-back canard. The absence of favorable interference effects of the wing on the low canard may be caused by forebody interference effects as indicated by the early stall of the canard-body alone configuration (see Figure 22). The oil flow data of Figures 14, 18, 20, and 21 indicate these trends.

Figure 7 shows the effect of canard size on the aerodynamic characteristics of the configuration utilizing the mid-canard location and mid-wing location. The data, as would be expected, show the large canard producing the larger lift increment and the more unstable longitudinal

moment. However, from the preceding discussion and data of reference 14 it appears that the interference effect of the canard on the wing is generally small and therefore, the lift interference increment noted is that due to increased area and favorable interference of the wing on the canard (see oil flow data, Figure 19).

Figure 8 shows the effect of the canard size on the aerodynamic characteristics of the configuration utilizing the mid-wing and the high-canard location. These data show the same basic trends as the data for the mid-canard location. It should be noted at this point that for the test configuration the low position for the canard indicated no favorable interference effect.

#### Lateral-Directional Stability Derivatives

The effect of wing height on the lateral-directional characteristics of the wing-body configuration is shown in Figure 9. The data show that for the high-wing location the vertical tail produces a stabilizing increment in  $C_{n\beta}$ , up to the highest test angle-of-attack, while the mid- and low-wing location exhibited a destabilizing increment in the high angle-of-attack range. In all cases the increment is altered by an adverse flow field and decreases with increasing angle of attack. A possible cause of this altered flow field is a combination of wing wake and forebody vortex. Above about 14 degrees angle of attack, addition of the vertical tail results in a destabilizing effect on the effective dihedral parameter ( $C_{l\beta}$ ).

Figure 10 shows the effect of the vertical height of the medium-size canard on the lateral-directional characteristics of the configuration utilizing the mid-wing location. The data show a markedly lower  $C_{n\beta}$  for the high-canard configuration and no significant improvement in the vertical tail effectiveness as the canard moves from the high to low position, other than a slight increase in the angle of attack before instability occurs. For all canard heights tested, the effect of the vertical tail on  $C_{l\beta}$  was destabilizing between 12 and 18 degrees angle of attack.

Figure 11 shows the effect of the vertical tail on the mid-wing configuration with and without the medium size canard located in the low position. The data indicates that addition of the canard caused a small increase in the vertical tail effectiveness up to approximately 20° angle of attack, and a marked decrease at higher angles. Also, the canard contribution to  $C_{n\beta}$  is destabilizing at high angles-of-attack. This effect may be caused by the canard vortex system changing the sidewash angle of the vertical tail, as well as the canard downwash altering the wing wake in the region of the vertical tail. This can also be seen by the reversal in  $C_{Y\beta}$ .

Figure 12 shows the effect of the vertical tail on the mid-wing configuration with and without the medium size canard in the high position. The data show the same trends as for the low position data. However, directional instability occurs at a lower angle of attack.

Figure 13 shows the effect of the vertical tail on the mid-wing and mid-canard configuration for the small and medium size canards. The

data show that, as the canard size increases, the vertical tail effectiveness decreases. This appears to indicate that the downwash from the canard is indeed altering the wing wake in the region of the vertical tail along with the canard vortex system altering the sidewash angle of the vertical tail. This is also indicated by the  $C_{Y\beta}$  reversal at about the same angle of attack at which the effectiveness becomes zero. The  $C_{l\beta}$  was not effected by canard size.

#### SUMMARY OF RESULTS

A study to determine the effect on the static aerodynamic characteristics of the relative size and vertical location of a swept back canard in combination with a swept forward wing as well as the effect of the vertical location of the wing on the wing body characteristics yields the following results:

1. With the canard off, varying the wing vertical location results in no appreciable effect on the longitudinal aerodynamic characteristics except for the high wing location above about  $30^\circ$  angle of attack.
2. No canard vertical location or canard size tested showed a favorable lift interference effect of the canard on the wing. However, the high-canard location indicated a sizeable favorable lift interference effect of the wing on the canard, while the low canard location generally showed no effect.
3. With the canard off, the vertical tail produced a stabilizing increment in directional stability up to the highest angle of attack tested for the high wing configuration; while the mid-

and low-wing configurations exhibited negative directional stability at substantially lower angles of attack.

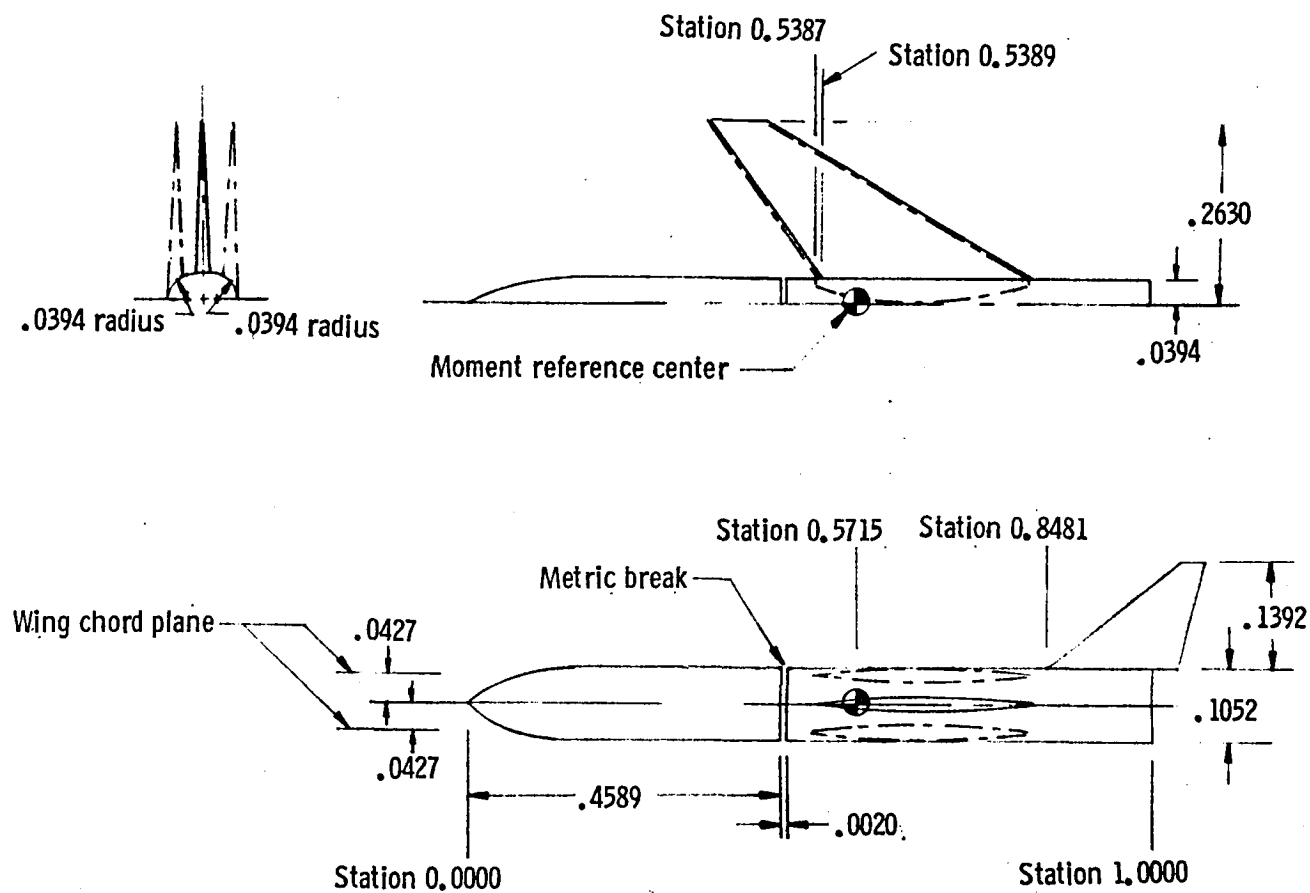
4. Addition of the canard to the mid-wing configuration reduced the directional stability and resulted in lower angles of attack for onset of directional instability.
5. For the configuration with the mid-wing and the medium-size canard, no significant improvement in directional stability occurred as the canard was moved from the high to the low position, other than a slight increase in the angle of attack for onset of instability.
6. As the canard size increased, directional instability occurred at a lower angle of attack.

## REFERENCES

1. Wright, J. B., and Loving, D. L., High Speed Wind Tunnel Tests of 1/16-Scale Model of the D-558 Research Airplane, NACA RM L6J09, 1947.
2. Whitcomb, R. T., An Experimental Study at Moderate and High Subsonic Speeds of the Flow Over Wings with  $30^\circ$  and  $45^\circ$  of Sweep-Forward in Conjunction with a Fuselage, NACA RM L50K28, 1950.
3. Whitcomb, R. T., An Experimental Study at Moderate and High Subsonic Speeds of the Flow Over Wings with  $30^\circ$  and  $45^\circ$  of Sweep-Back in Conjunction with a Fuselage, NACA RM L50K27, 1951.
4. Diederick, F. W.; and Budiansky, B.: Divergence of Swept Wings, ACA Technical Note 1680, 1948.
5. Bisplinghoff, R. L.; and Ashley, H.: Principles of Aeroelasticity, John Wiley and Sons, Inc., New York, 1962.
6. Krone, N. J., Lt. Co., Divergence Elimination with Advanced Composites, AIAA Paper No. 75-1009, Aircraft Systems and Technology Meeting, Los Angeles, California, August 1975.
7. Huffman, Jarrett K., and Fox, Charles H., Jr.; Subsonic Longitudinal and Lateral-Directional Static Aerodynamic Characteristics for a Close-coupled Wing-Canard Model in Both Swept Back and Swept Forward Configurations NASA TM-74092, 1978.
8. Huffman, Jarrett K., and Fox, Charles H., Jr.: Subsonic Longitudinal and Lateral-Directional Static Aerodynamic Characteristics for a Model with Swept Back and Swept Forward Wings. NASA TM-74093, 1978.
9. Mechtly, E. A.: The International System of Units. NASA SP-7012, 1964.

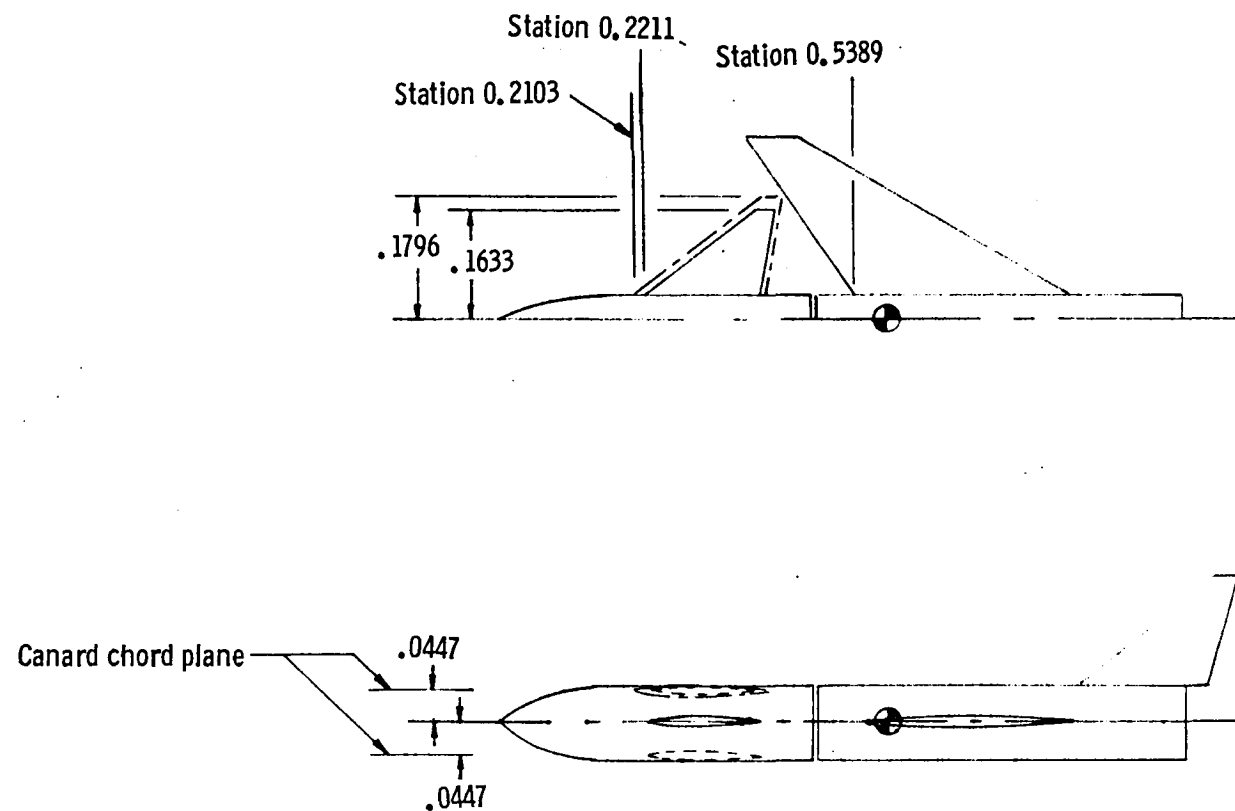
10. Fox, Charles H., Jr., and Huffman, Jarrett K.: Calibration and Test Capabilities of the Langley 7- by 10-foot High Speed Tunnel. NASA TM X-74027, 1977.
11. Gillis, Clarence L.; Polhamus, Edward C., and Gray, Joseph L., Jr.: Charts for Determining Jet-Boundary Corrections for Complete Models in 7- by 10-foot Closed Rectangular Wing Tunnels. NACA WR-L-123, 1945.
12. Herriott, John G.: Blockage Corrections for Three-Dimensional-Flow Closed-Throat Wind Tunnels, with Consideration of the Effect of Compressibility. NACA Report 995, 1950.
13. Braslow, Albert L.; Hicks, Raymond M.; and Harris, Roy V., Jr.: Use of Grit-type Boundary-Layer Transition Trips on Wind Tunnel Models. NASA TN D-3579, 1966.
14. Gloss, Blair B.: Effect of Wing Planform and Canard Location and Geometry on the Longitudinal Aerodynamic Characteristics of a Close-Coupled Canard Wing Model at Subsonic Speeds. NASA TN D-7910, 1975.



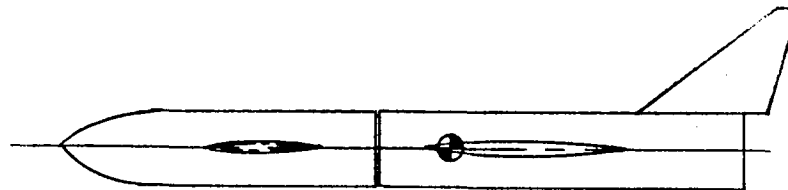
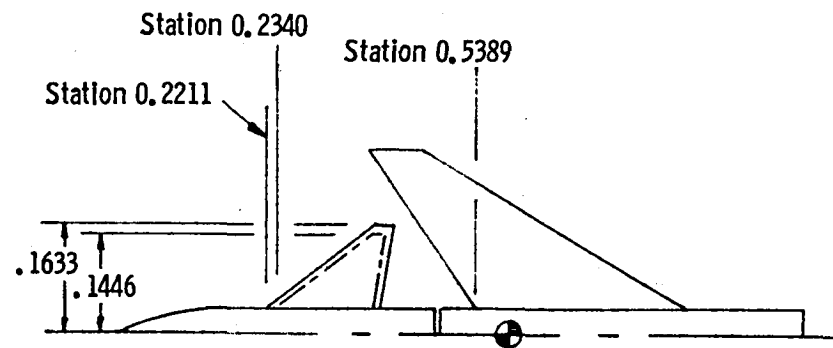


(a) General arrangement showing wing height variation.

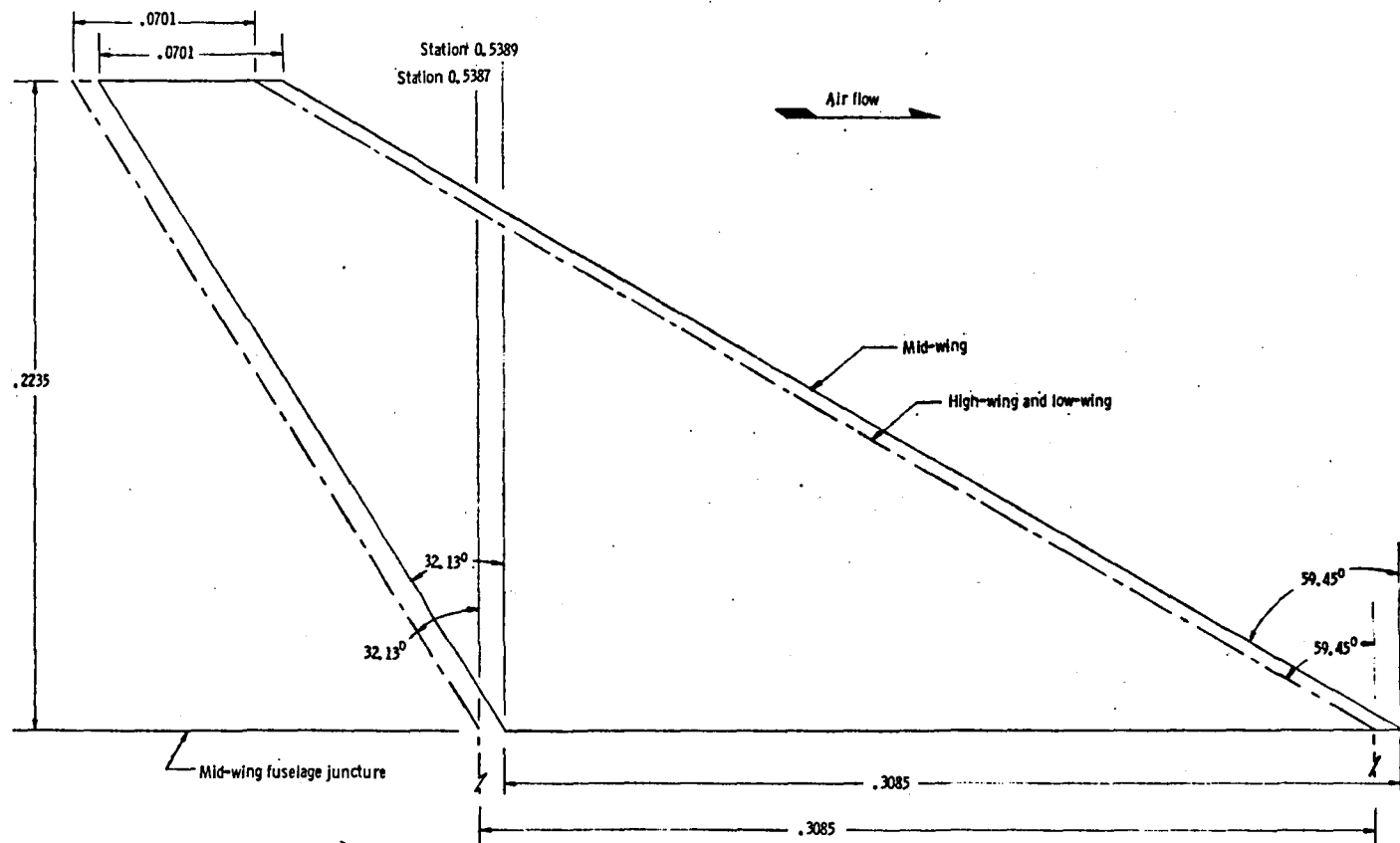
Figure 1. Drawings of the models tested. All dimensions are normalized by a fuselage length of 0.96589 m. (38.027 in.)



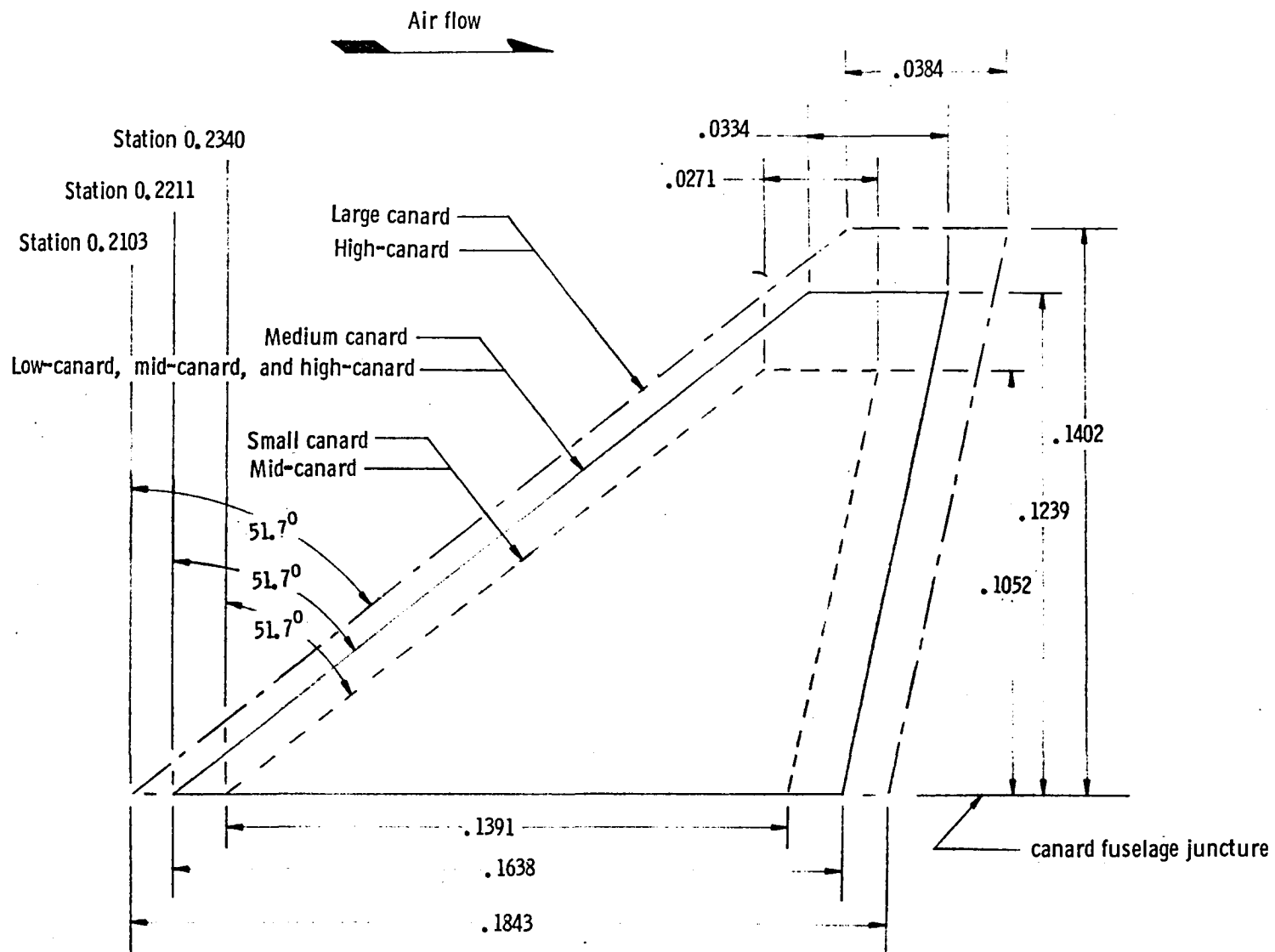
(b) General arrangement showing canard height variation.  
Figure 1. Continued.



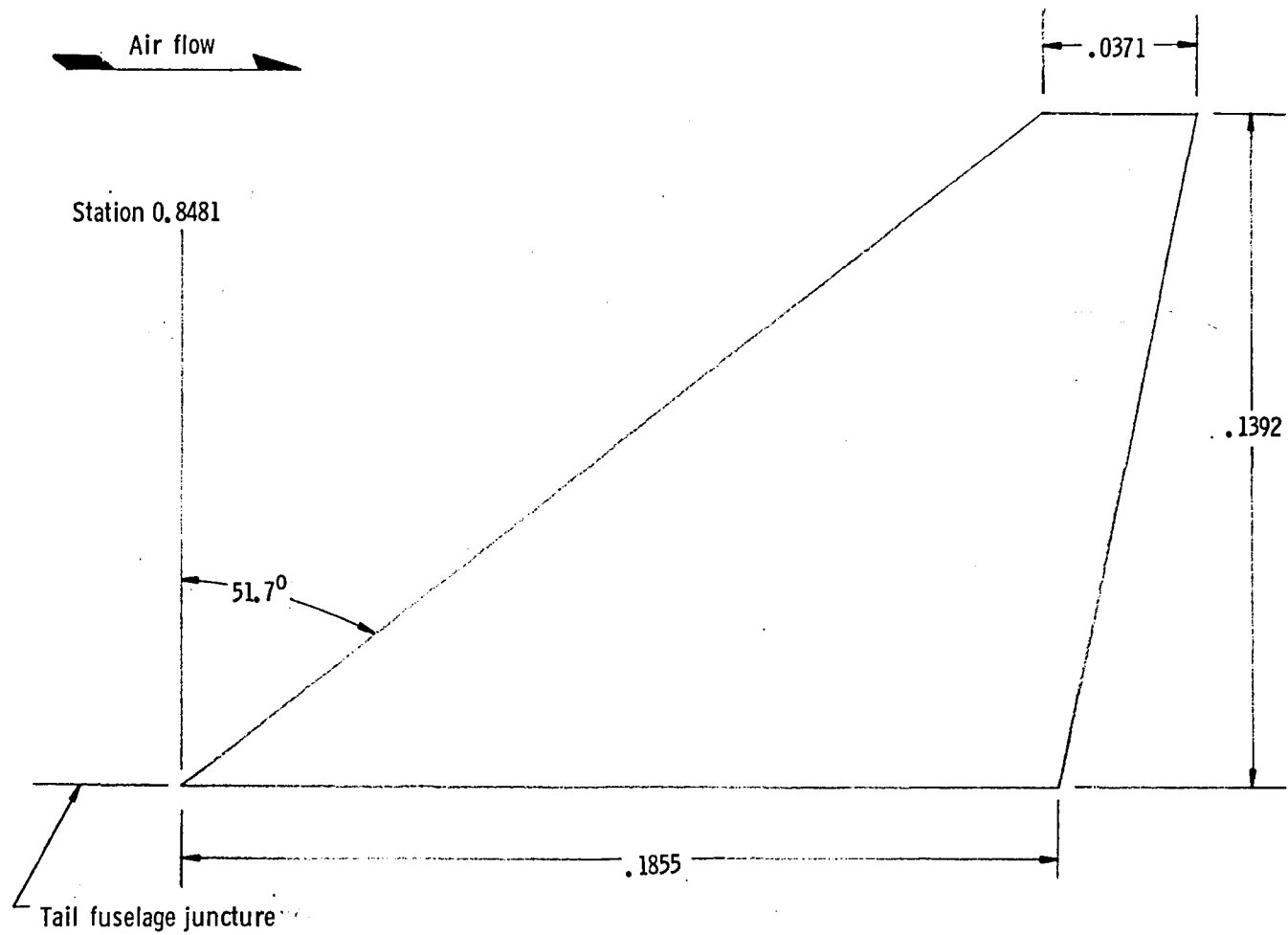
(c) General arrangement showing canard size variation.  
Figure 1. Continued.



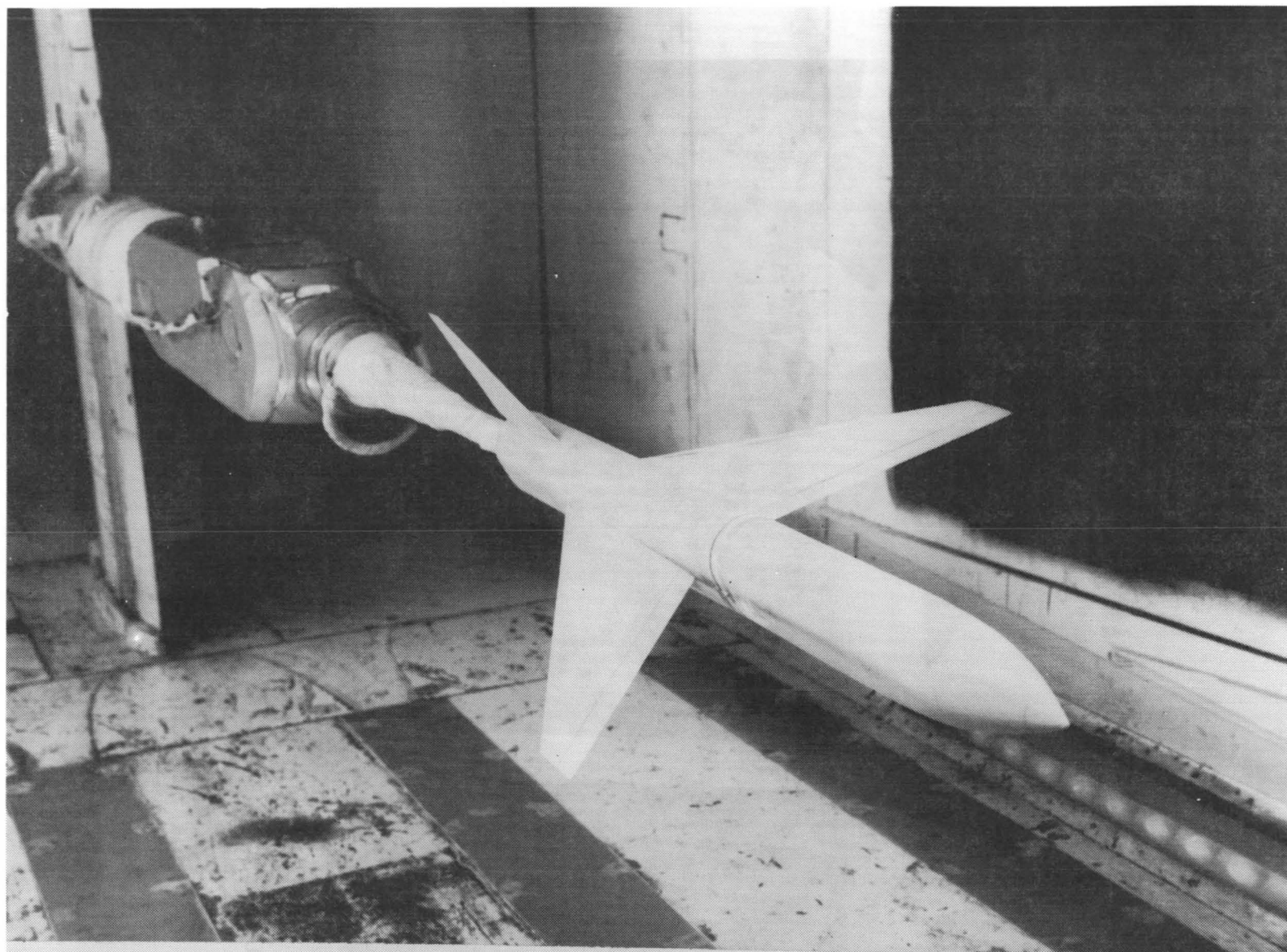
(d) Details of the wings.  
Figure 1, Continued.



(e) Details of the canards.  
Figure 1. Continued.

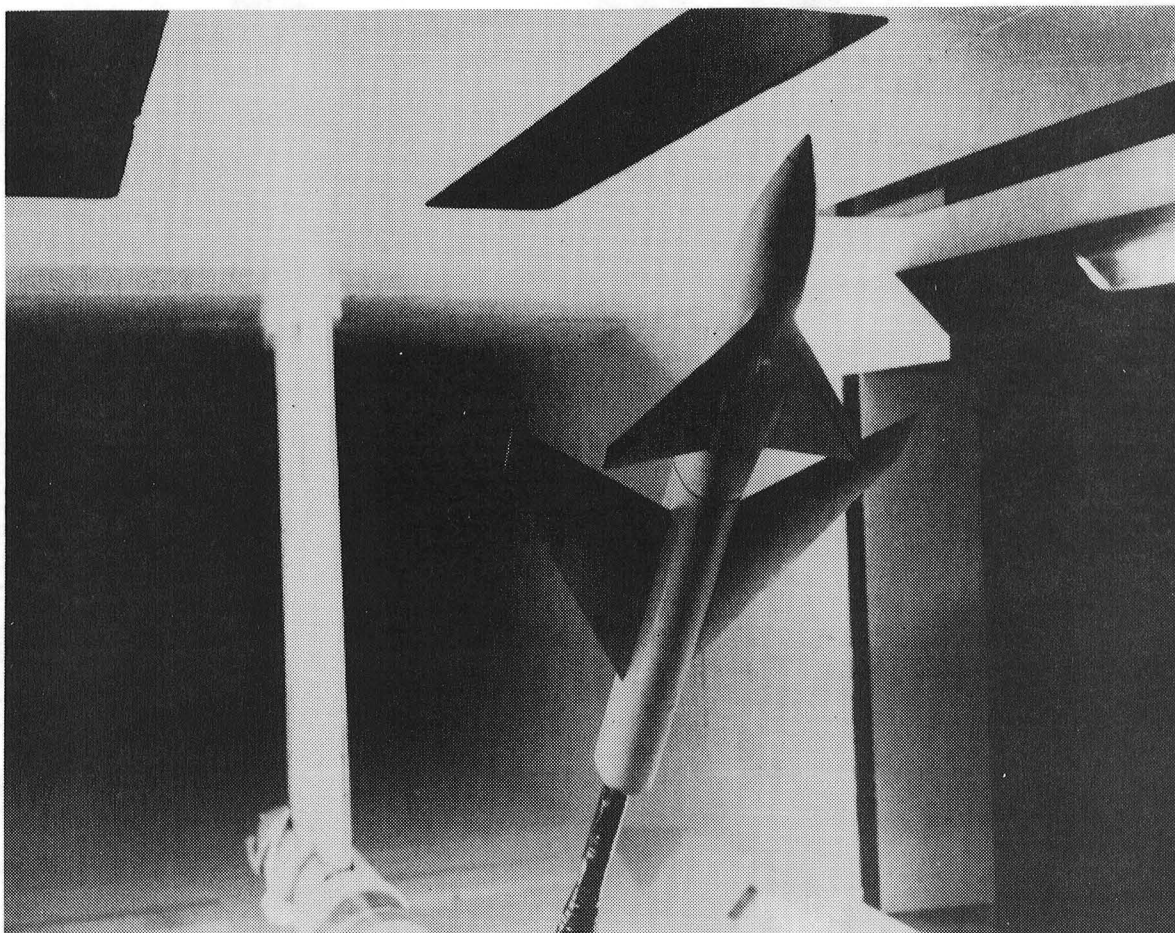


(f) Details of the vertical tail.  
Figure 1. Concluded.



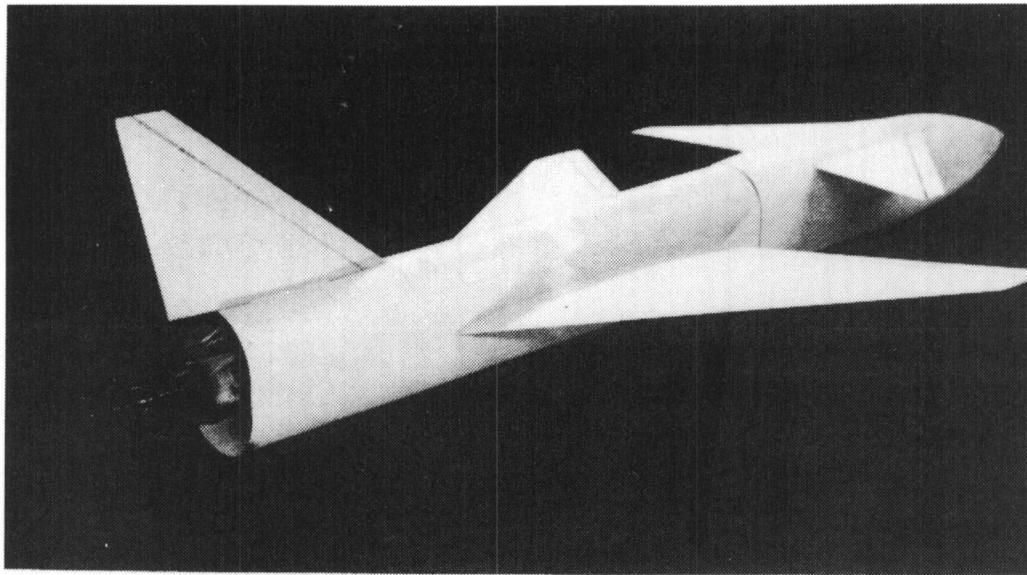
(a) Basic mid-wing configuration

Figure 2. Photographs of the model installed in the Langley 7- by 10-foot high speed tunnel.



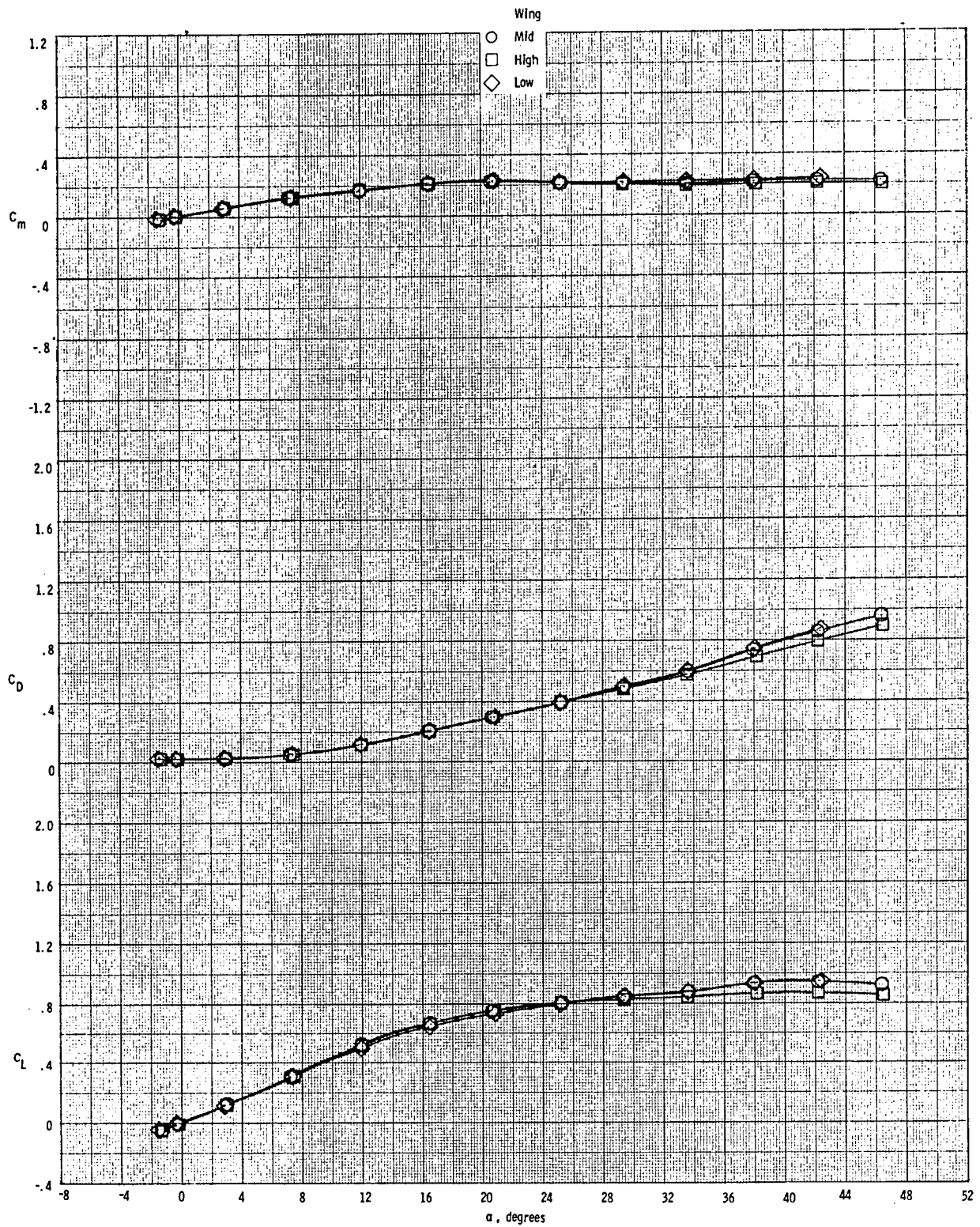
(b) Mid-wing medium size low-canard configuration  
Figure 2. Continued.



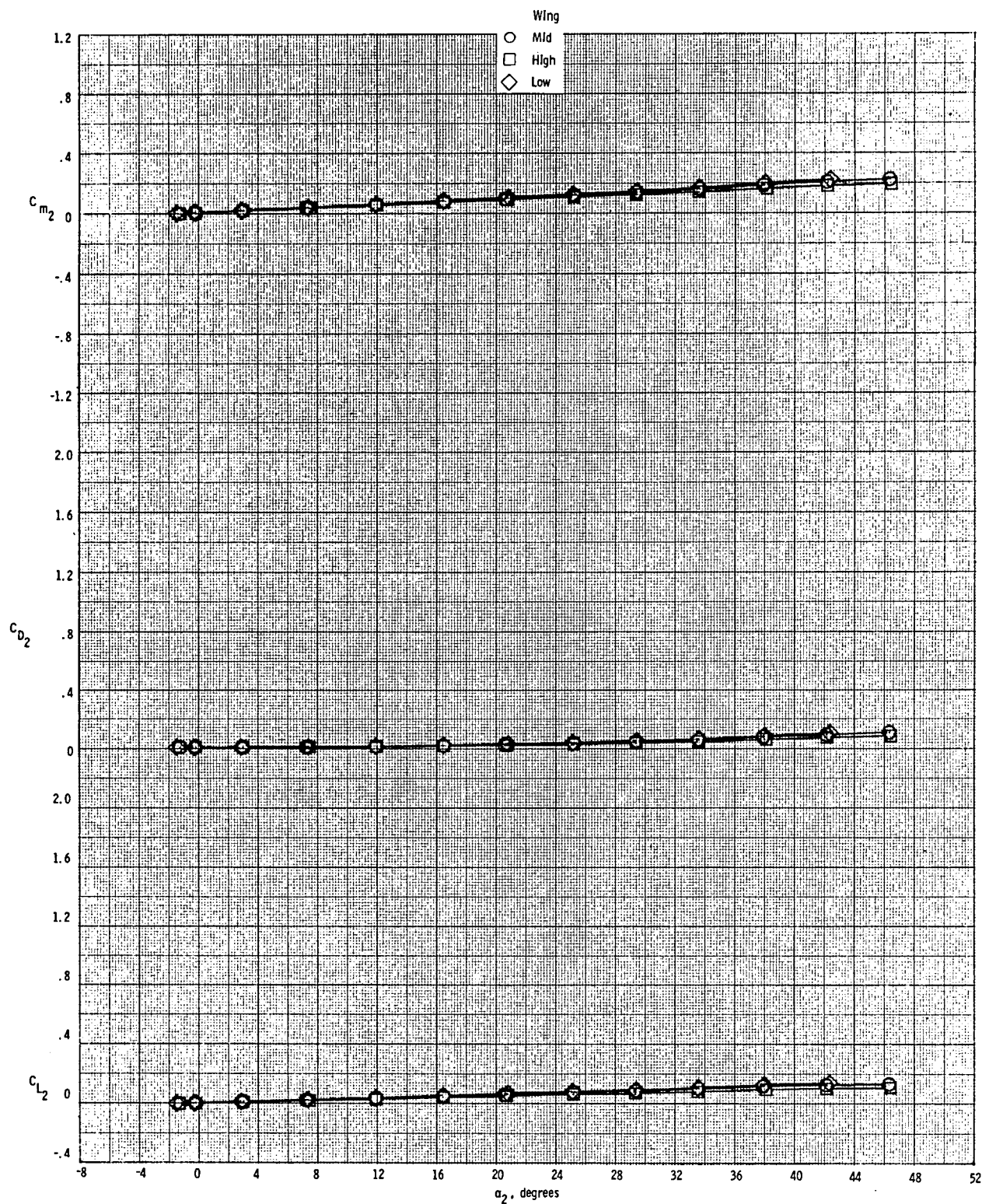


(c) Mid-wing medium size high-canard configuration  
Figure 2. Concluded.

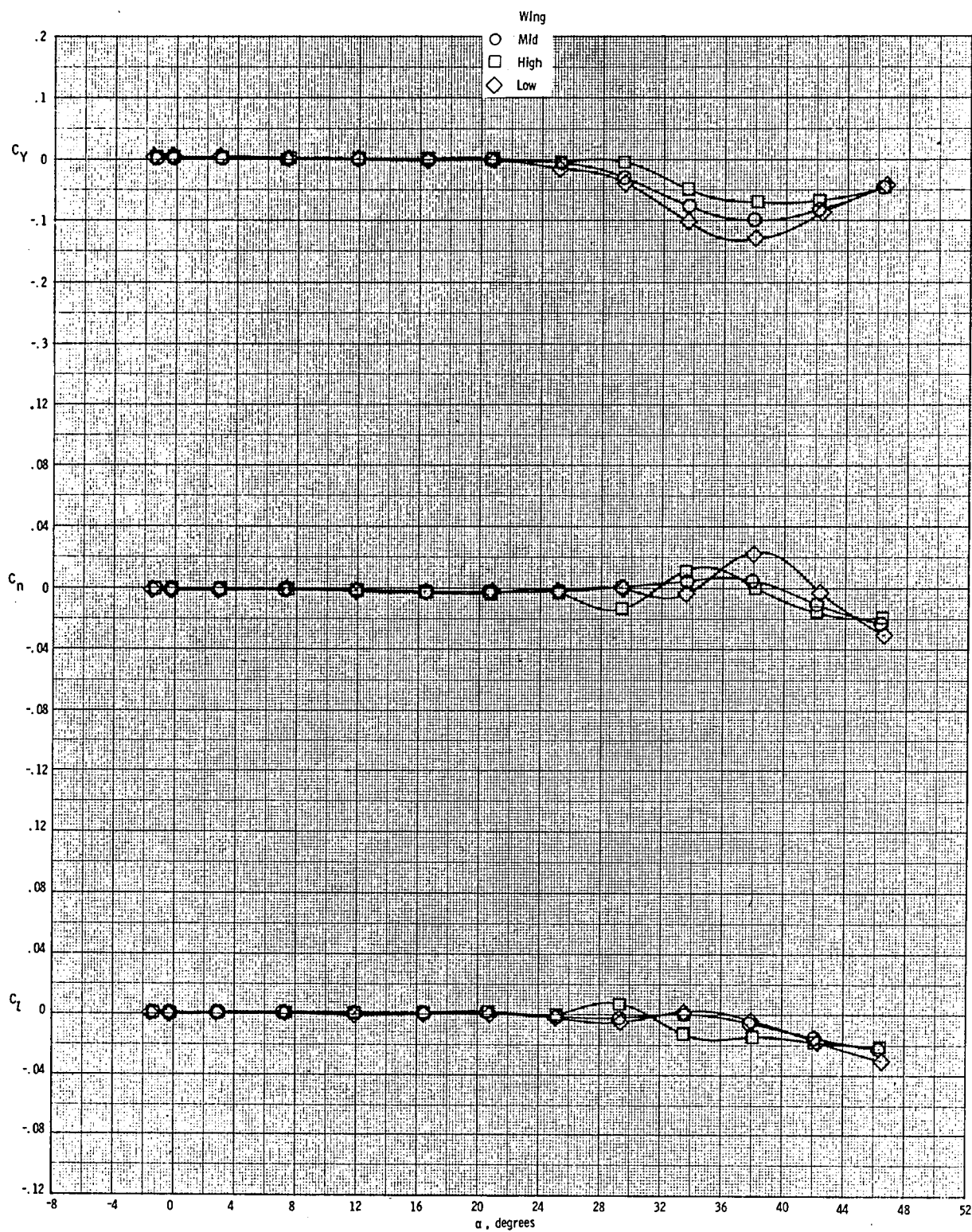




(a) Main balance longitudinal data  
 Figure 3. Effect of wing height on the aerodynamic characteristics of the basic wing body configuration with the vertical tail on.  $M = 0.3, \beta = 0^\circ$ .

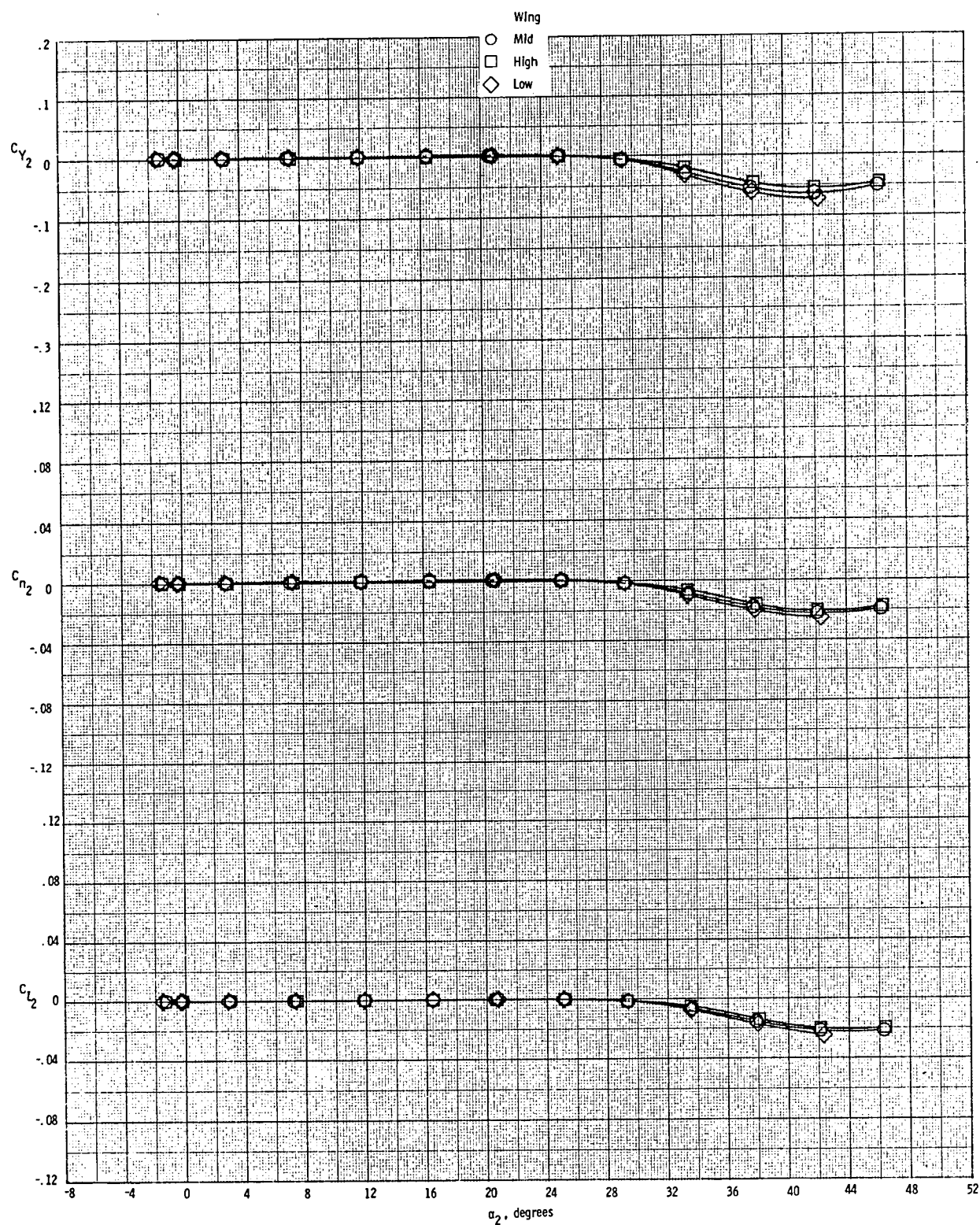


(b) Nose balance longitudinal data  
Figure 3. Continued.

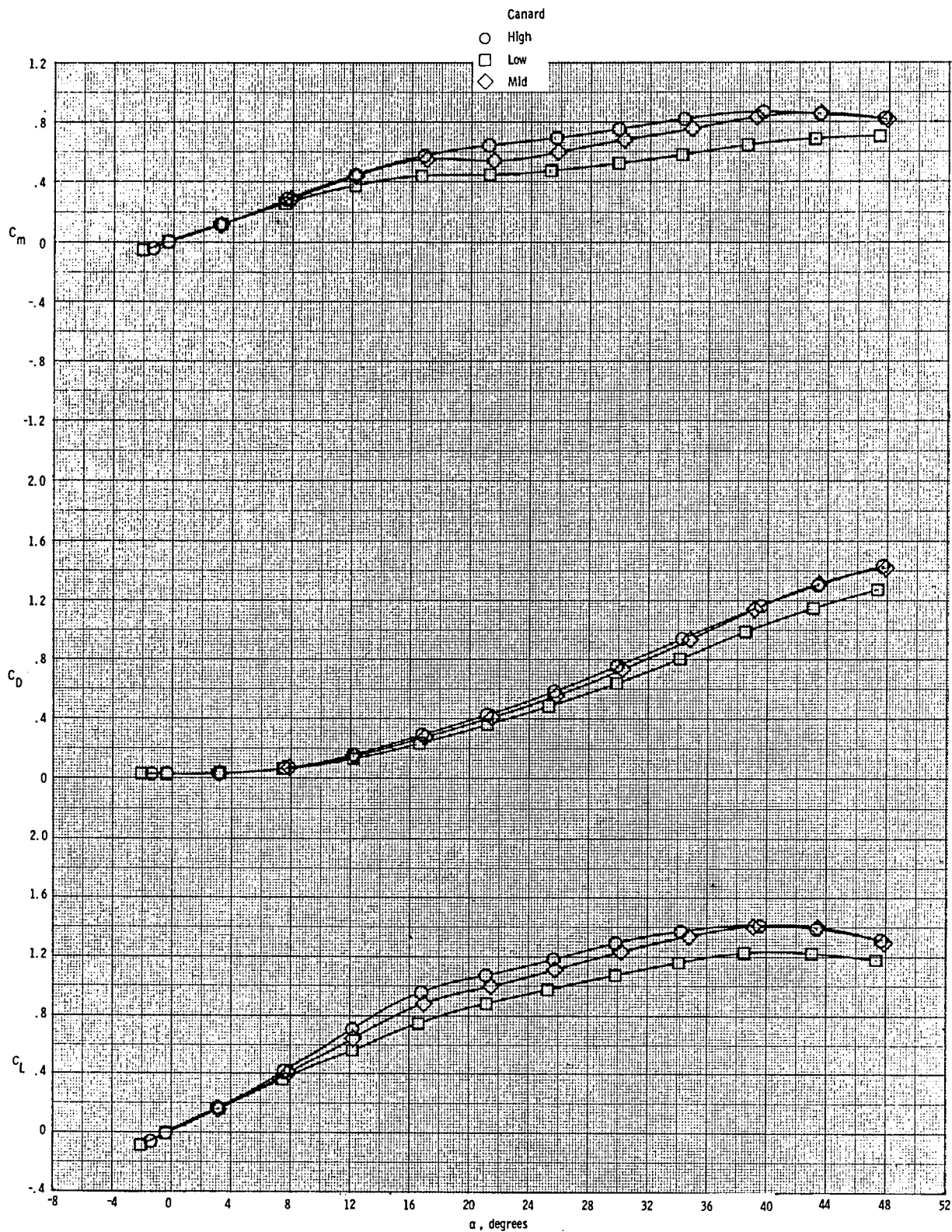


(c) Main balance lateral-directional data  
 Figure 3. Continued.

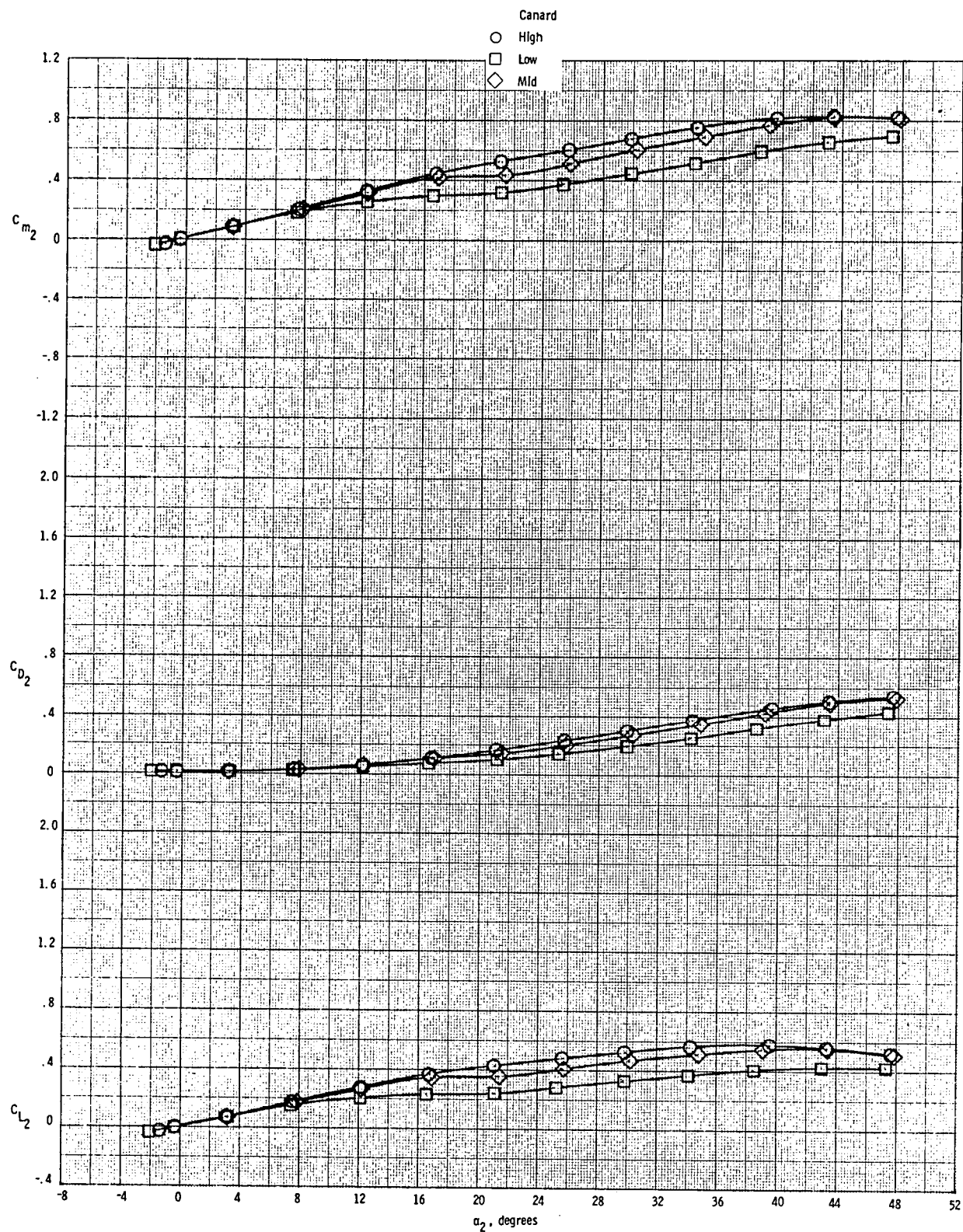




(d) Nose balance lateral-directional data  
Figure 3. Concluded.

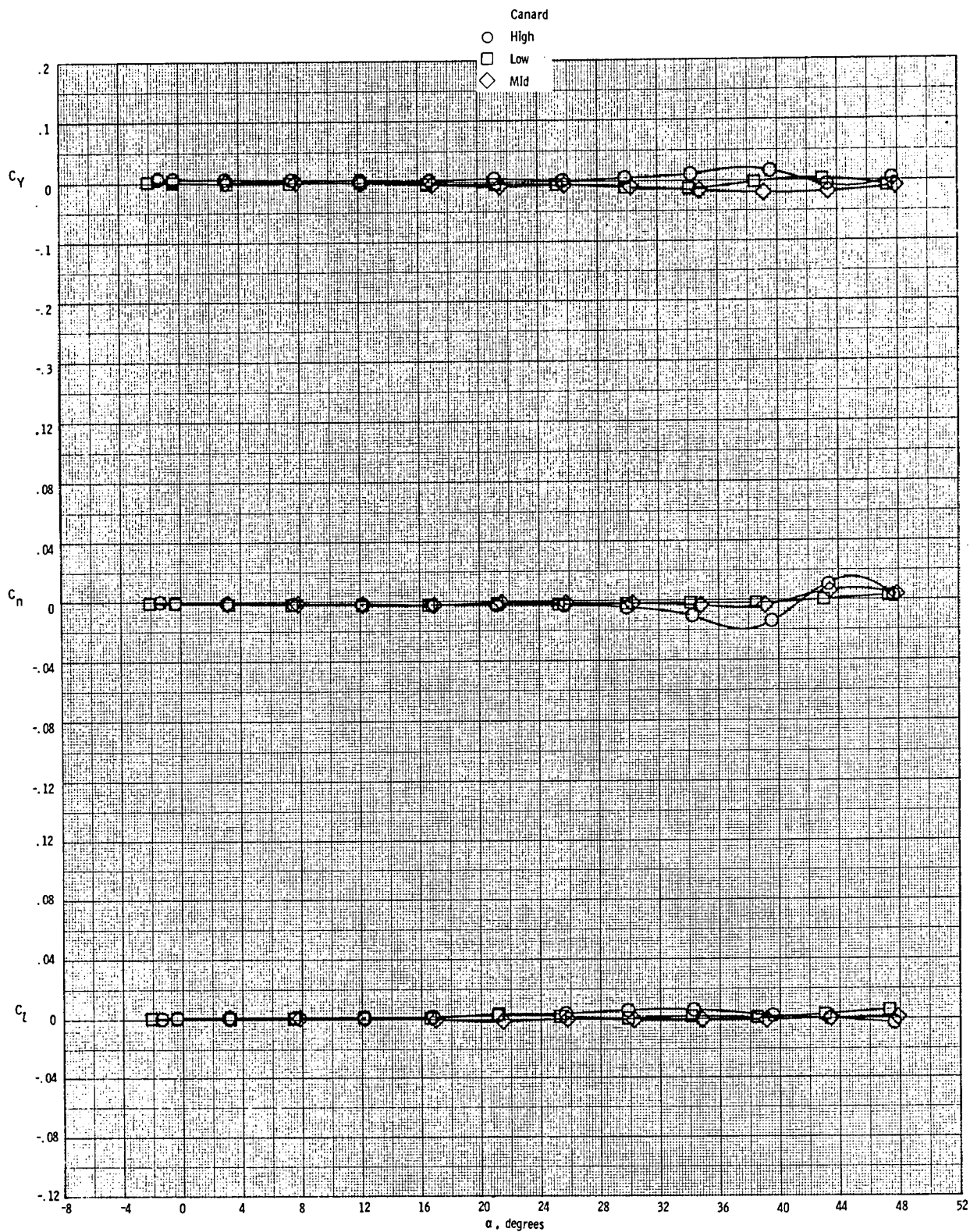


(a) Main balance longitudinal data  
 Figure 4.- Effect of canard height on the aerodynamic characteristics of the mid-wing medium canard configuration with the vertical tail on.  $M = 0.3$ ,  $\beta = 0^\circ$ .

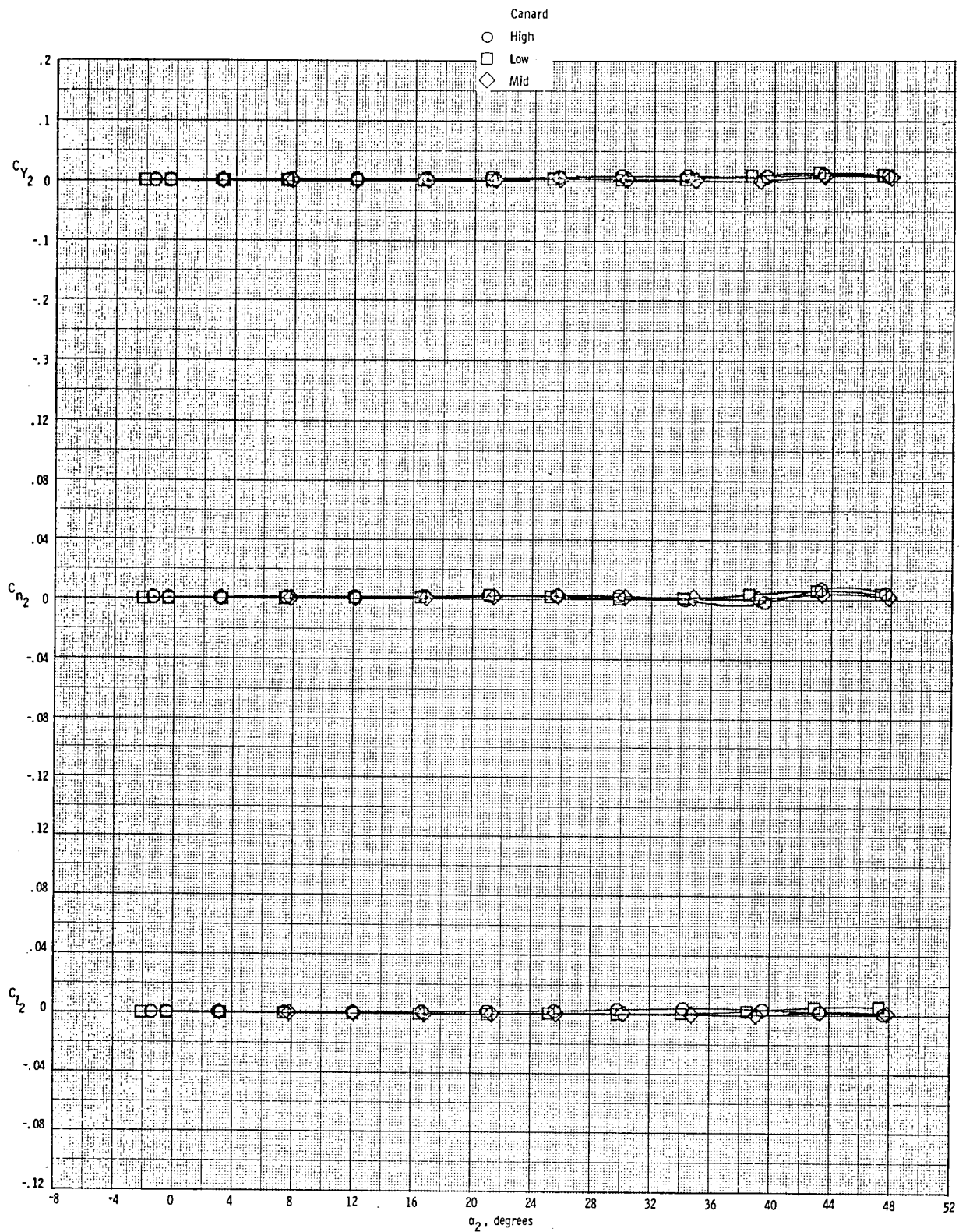


(b) Nose balance longitudinal data  
Figure 4.- Continued.

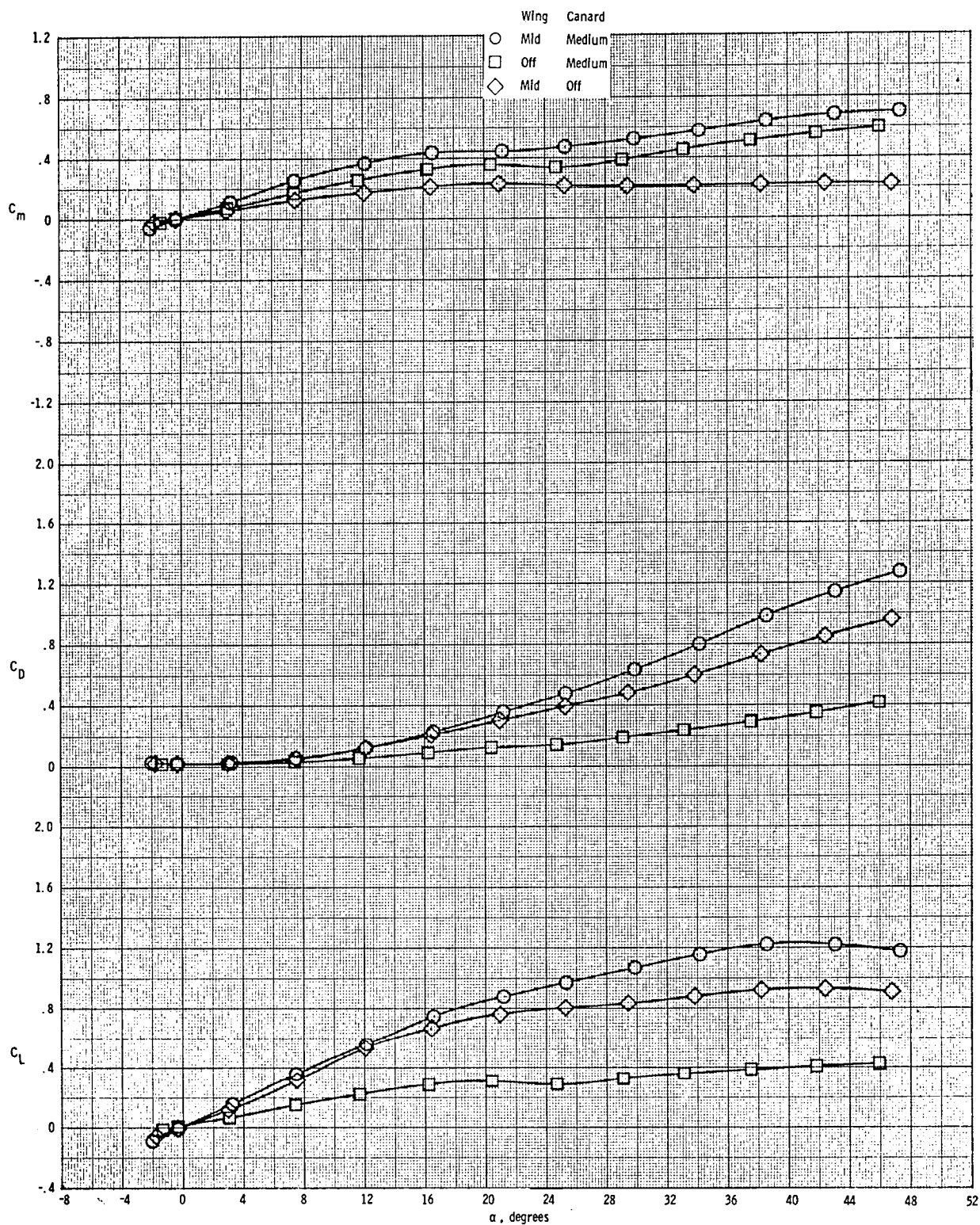




(c) Main balance lateral-directional data  
Figure 4.- Continued.

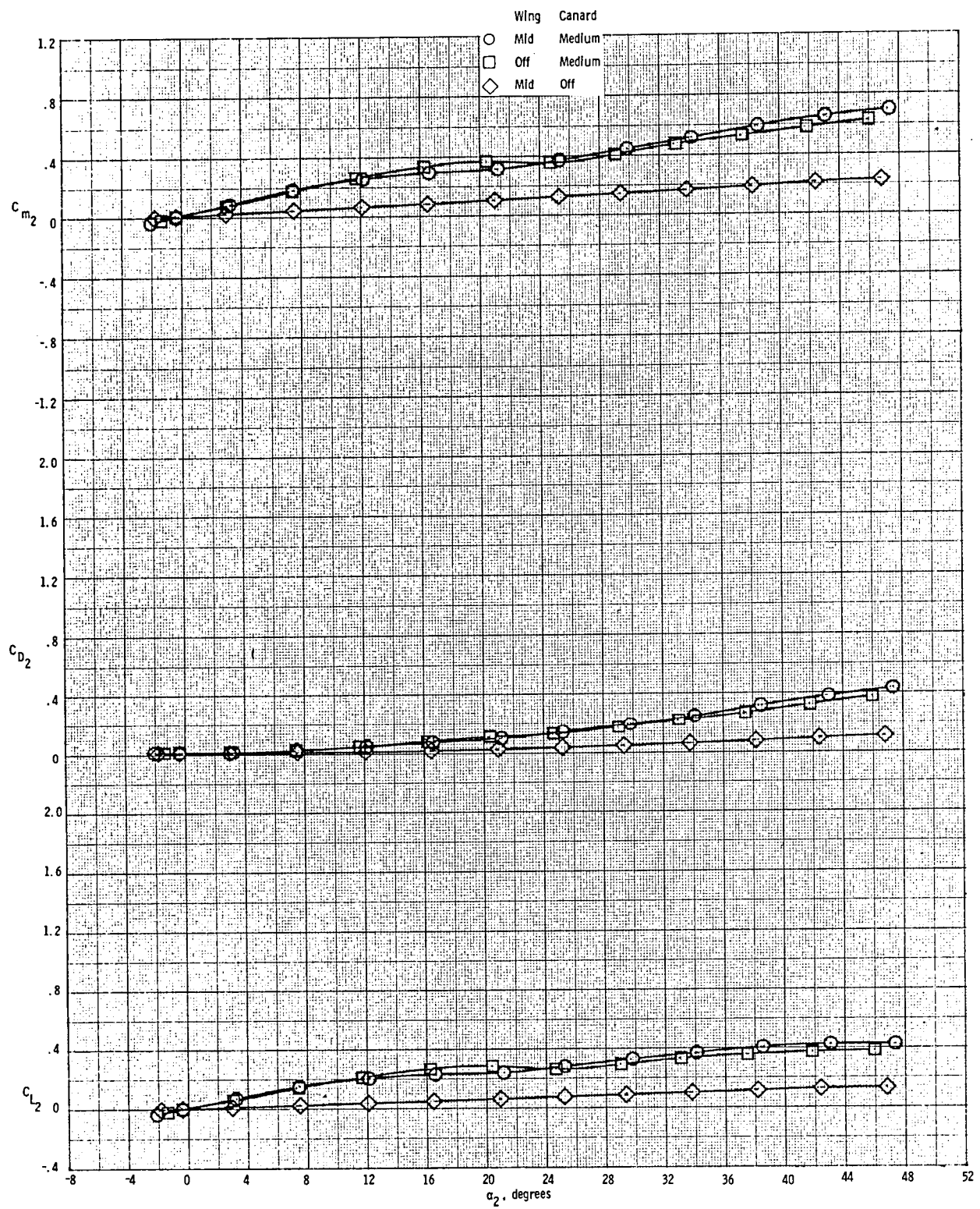


(d) Nose balance lateral-directional data  
Figure 4.- Concluded.



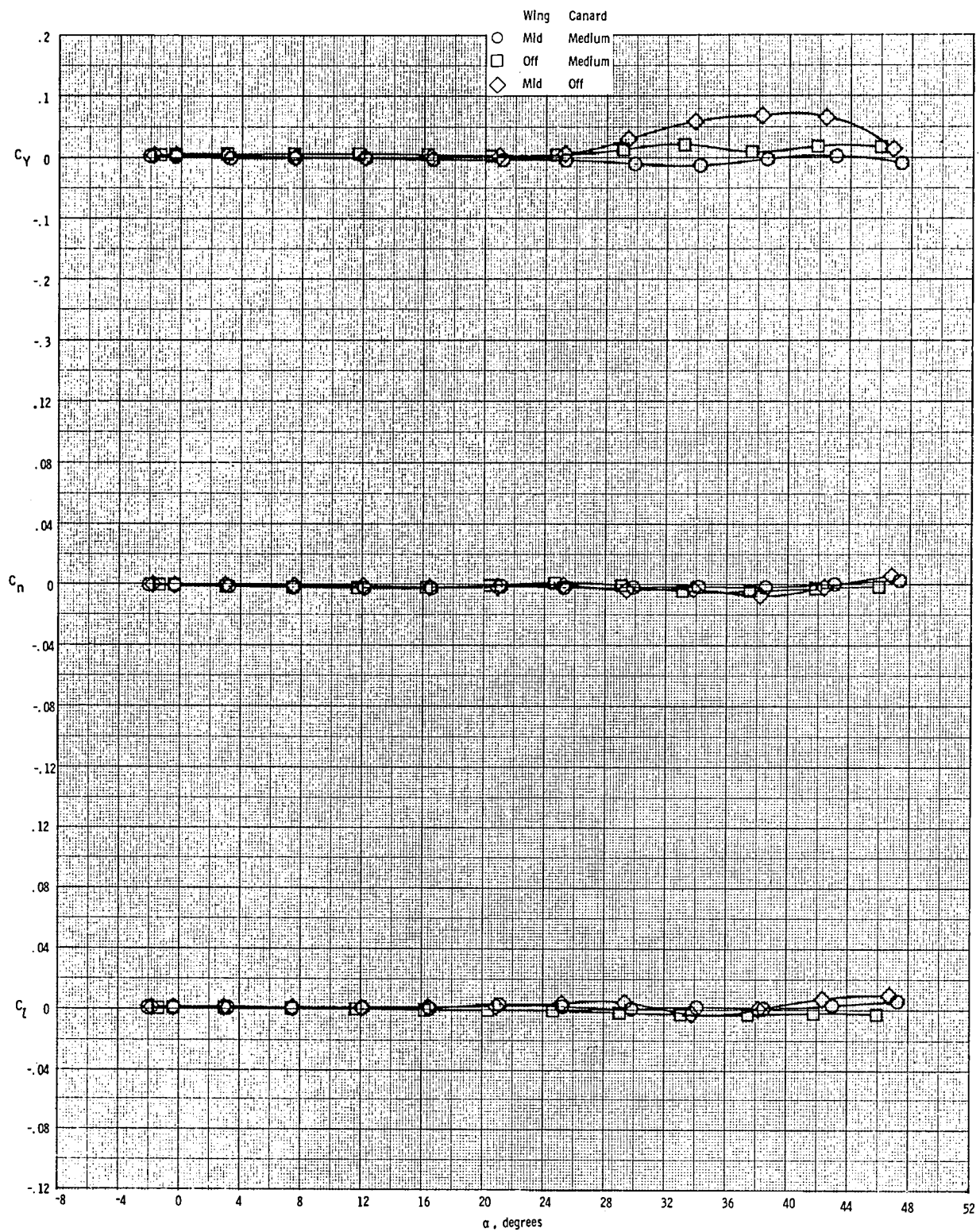
(a) Main balance longitudinal data

Figure 5.- Effect of component breakdown on the aerodynamic characteristics of the low canard configuration with the vertical tail on.  $M = 0.3$ ,  $\beta = 0^\circ$ .

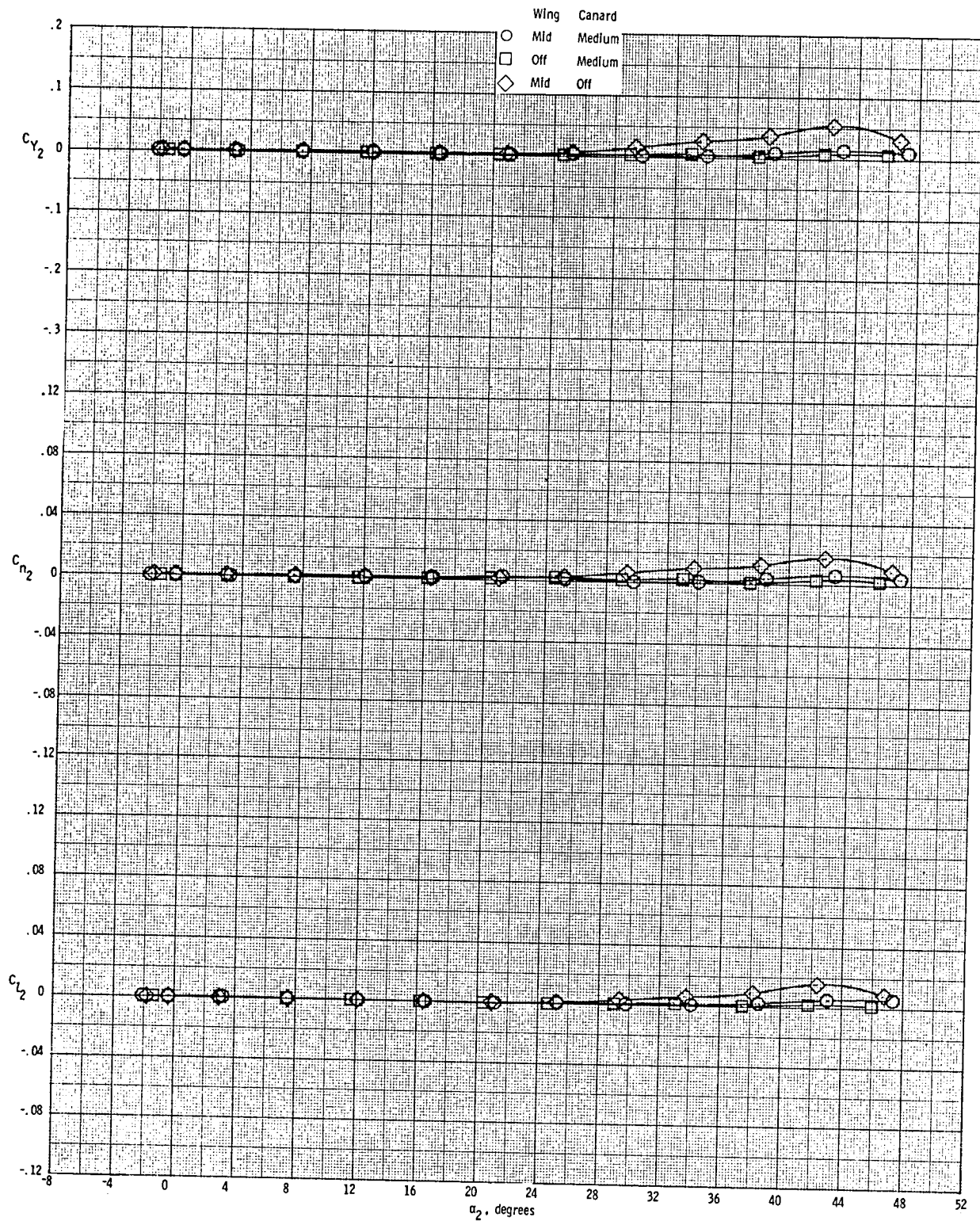


(b) Nose balance longitudinal data  
Figure 5.- Continued.

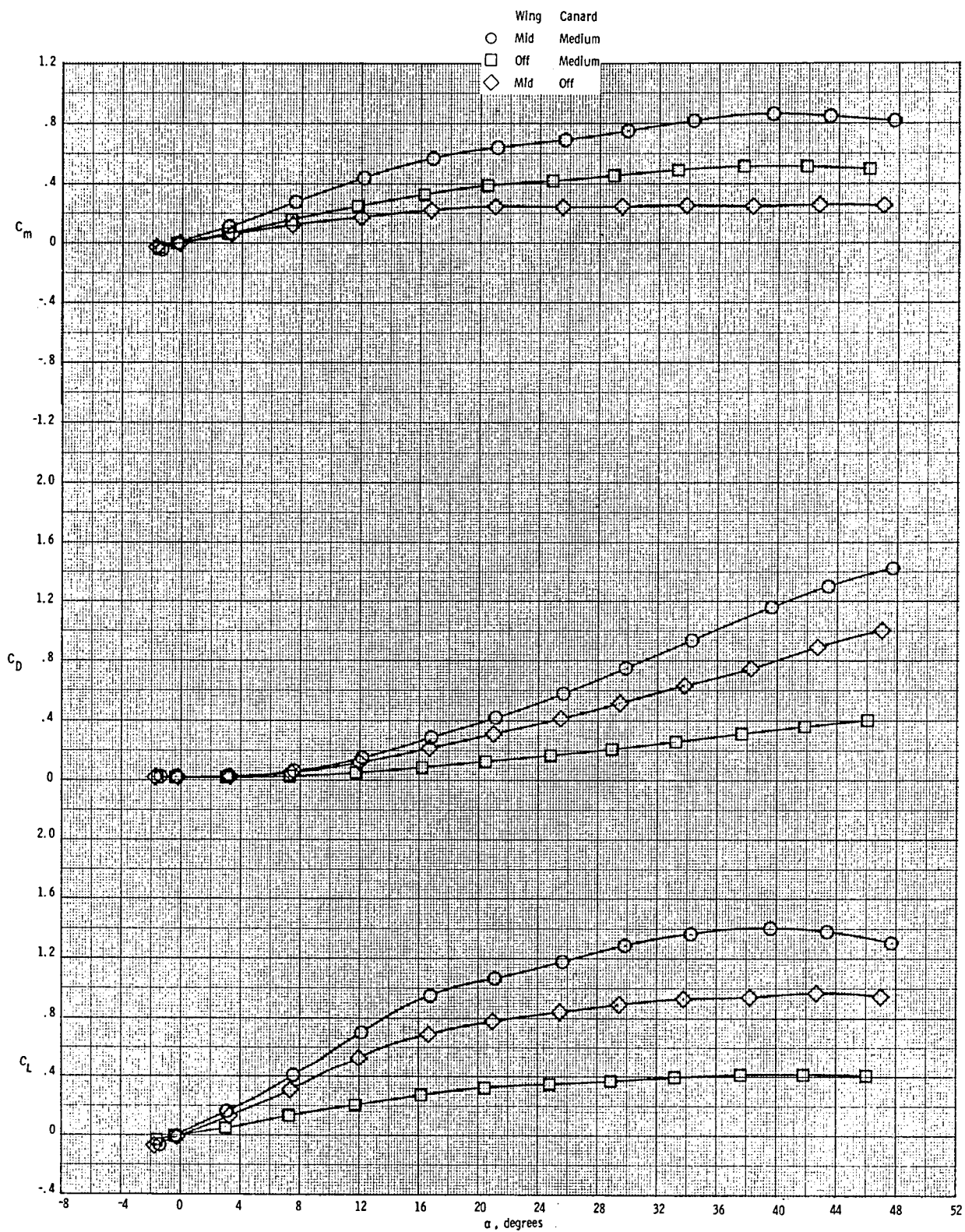




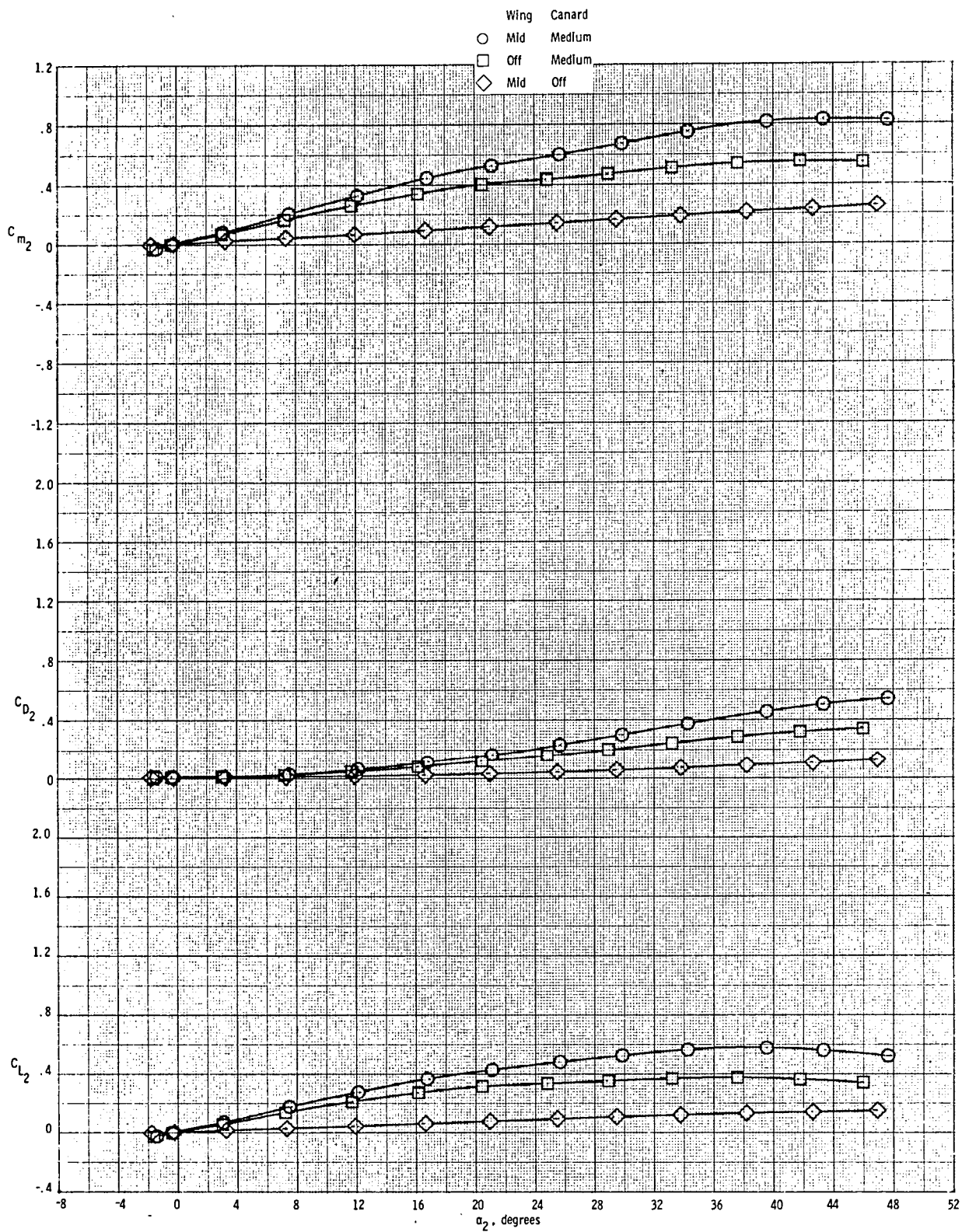
(c) Main balance lateral-directional data  
Figure 5.-Continued.



(d) Nose balance lateral-directional data  
Figure 5.- Concluded.

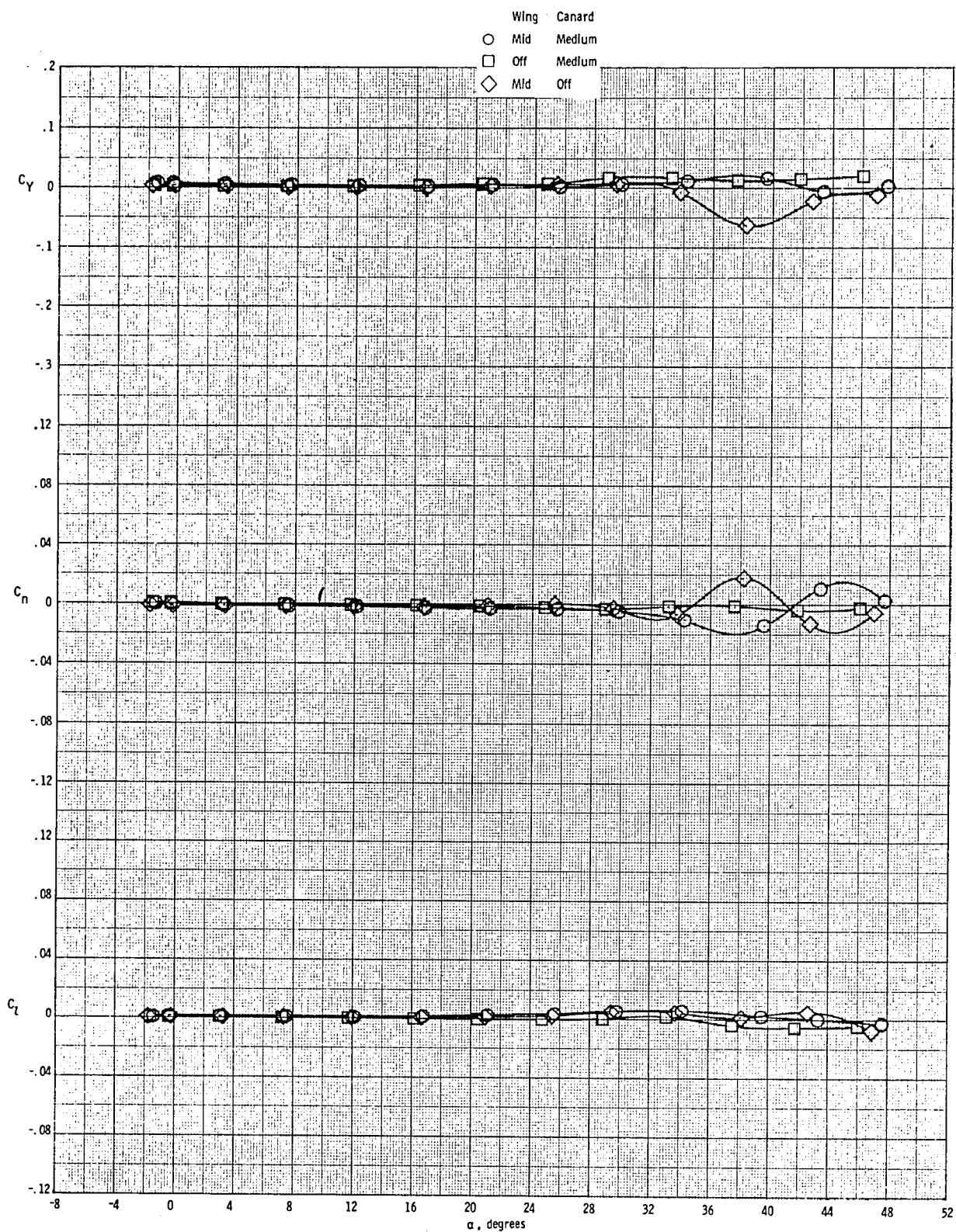


(a) Main balance longitudinal data  
 Figure 6.- Effect of component breakdown on the aerodynamic characteristics of the high canard configuration with the vertical tail on.  $M = 0.3$ ,  $\beta = 0^\circ$ .

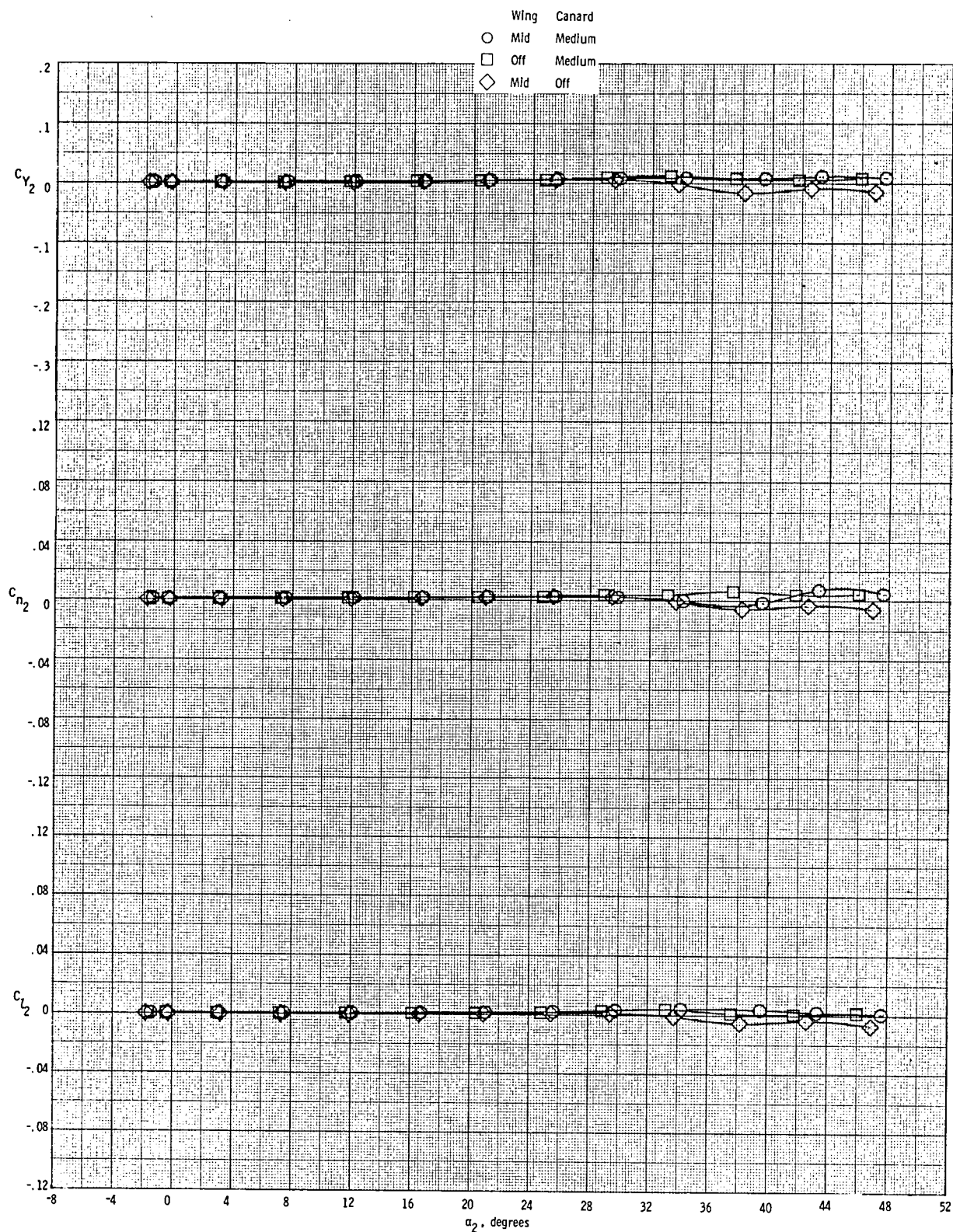


(b) Nose balance longitudinal data  
 Figure 6. - Continued.

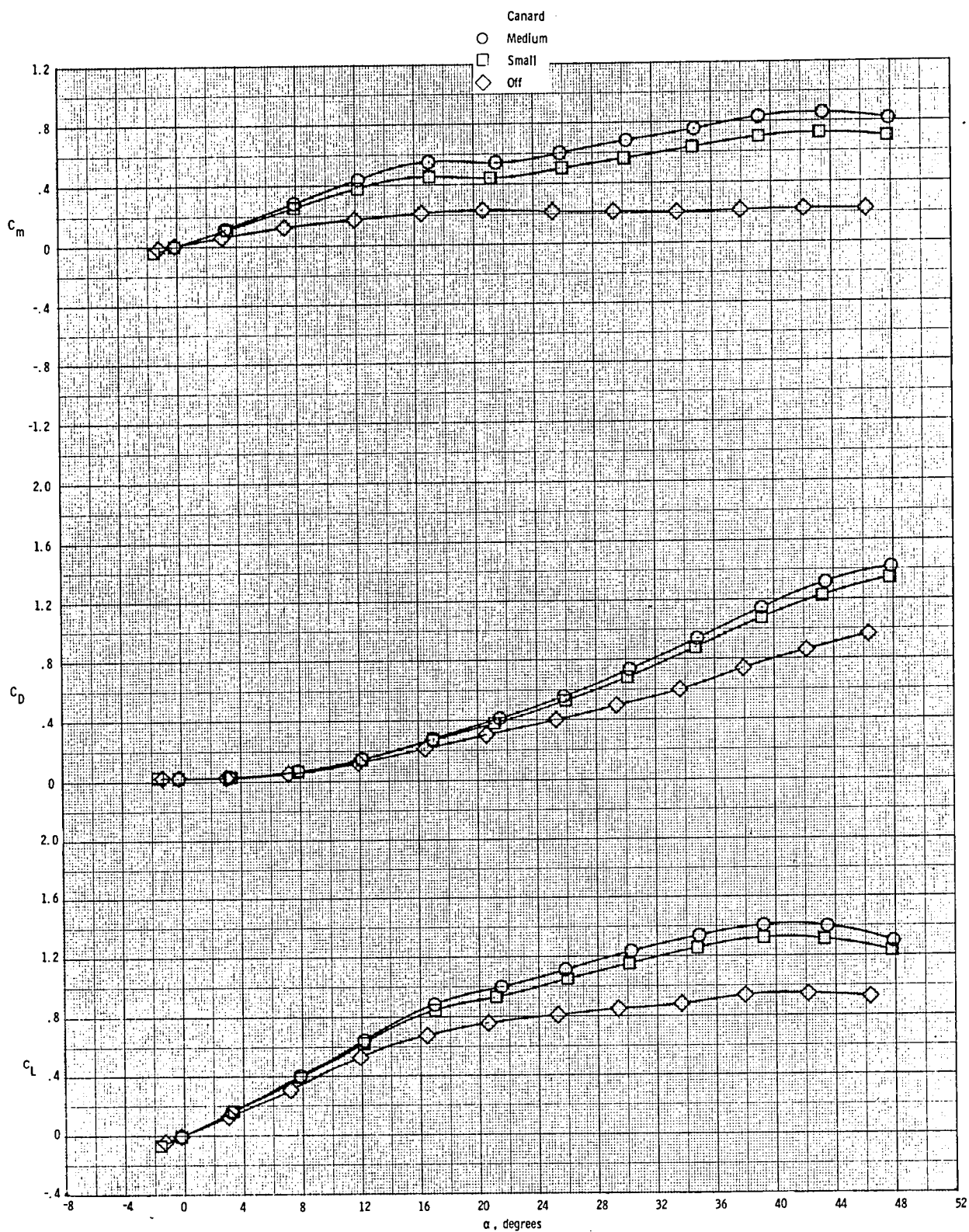




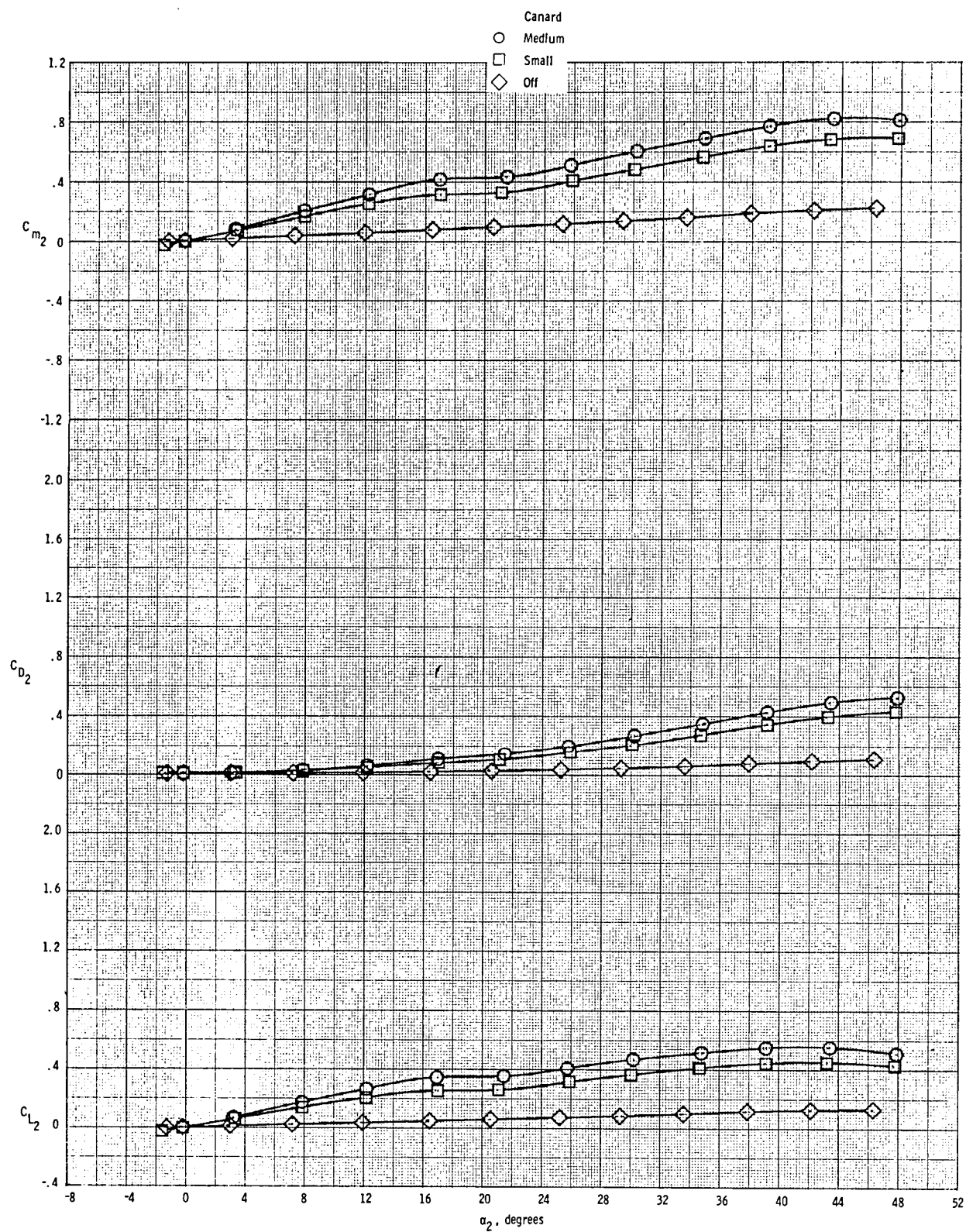
(c) Main balance lateral-directional data  
 Figure 6.- Continued.



(d) Nose balance lateral-directional data  
Figure 6. - Concluded.

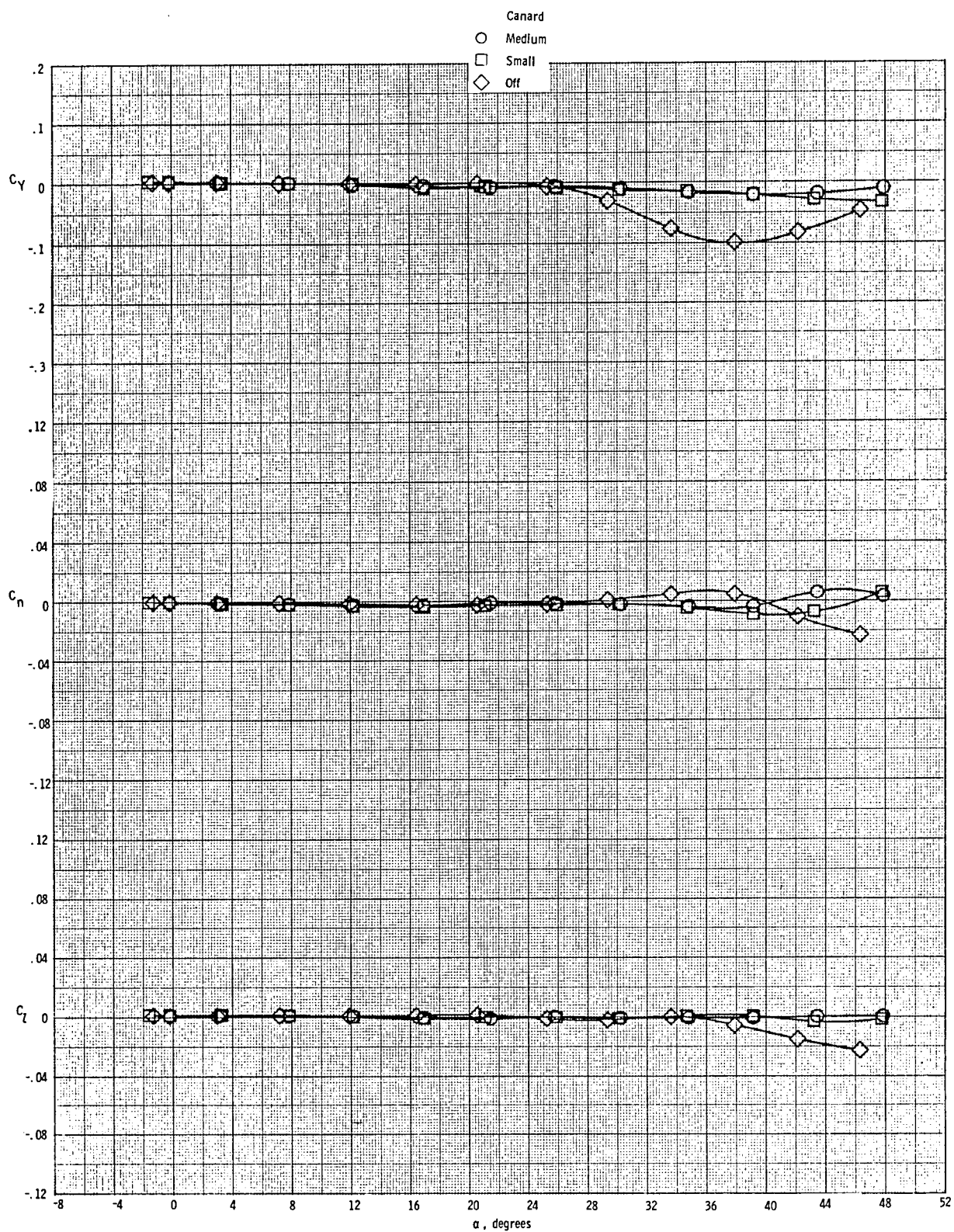


(a) Main balance longitudinal data  
 Figure 7.- Effect of canard size on the aerodynamic characteristics of the mid-wing mid-canard configuration with the vertical tail on.  $M = 0.3$ ,  $\beta = 0^\circ$ .

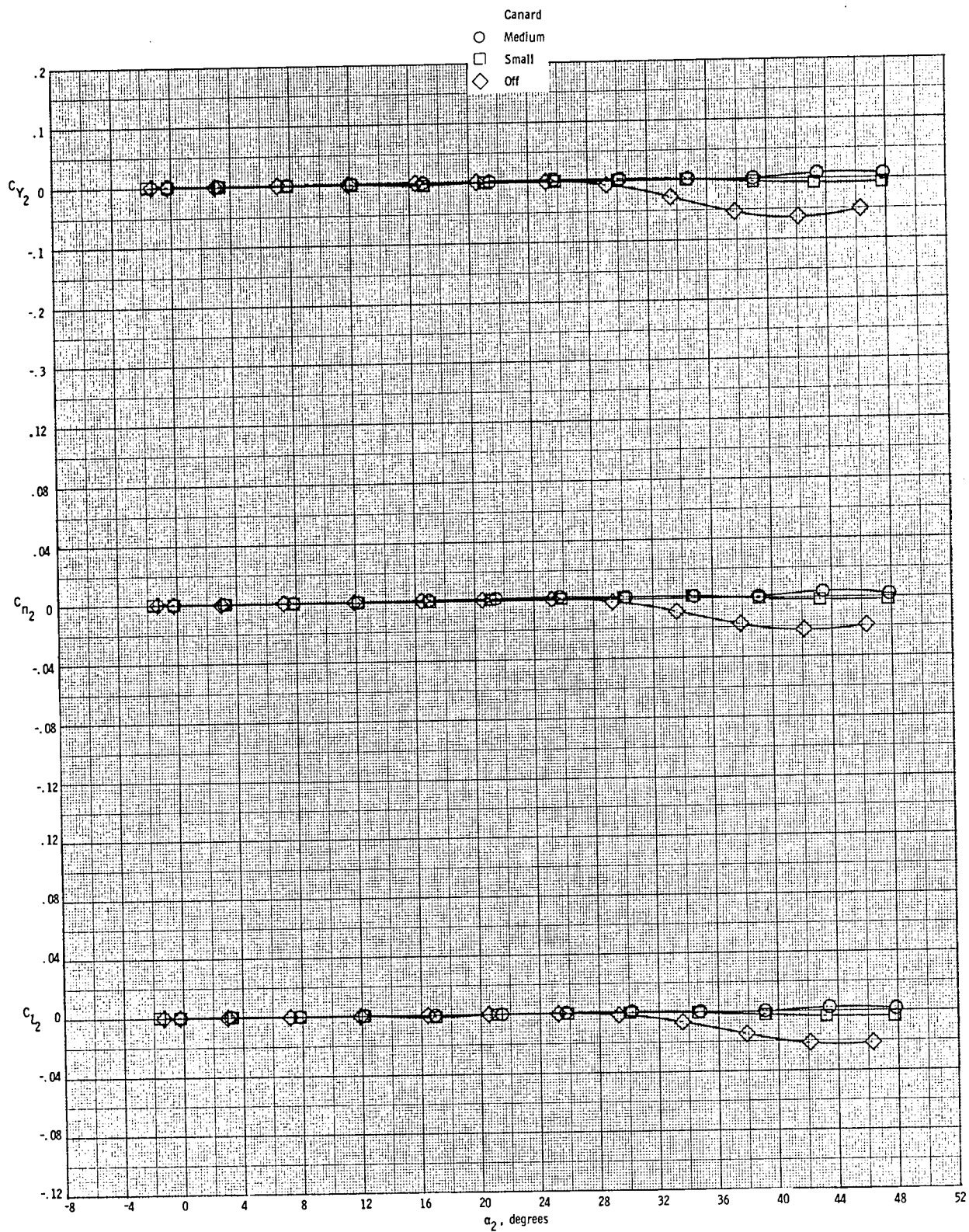


(b) Nose balance longitudinal data  
Figure 7.- Continued.

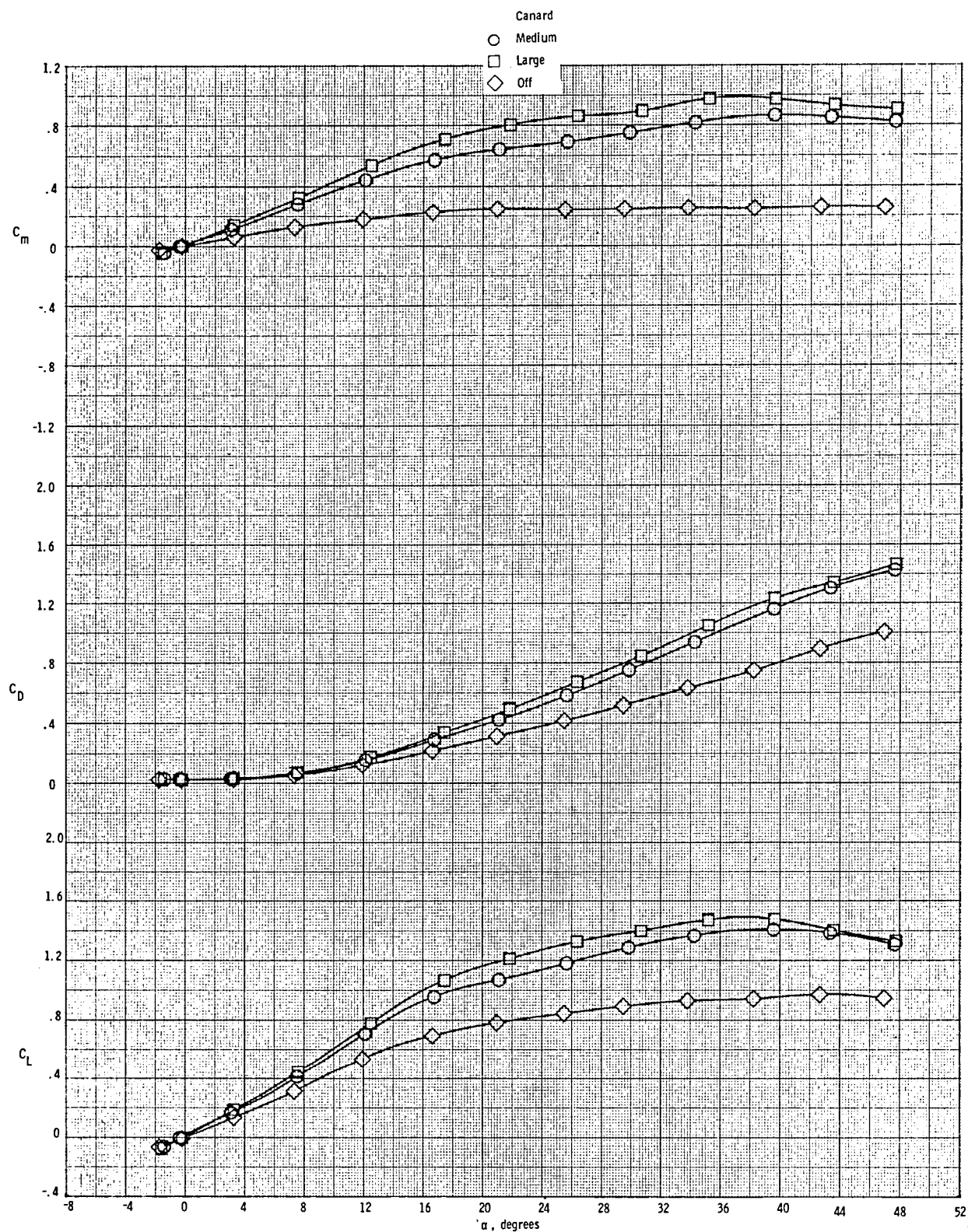




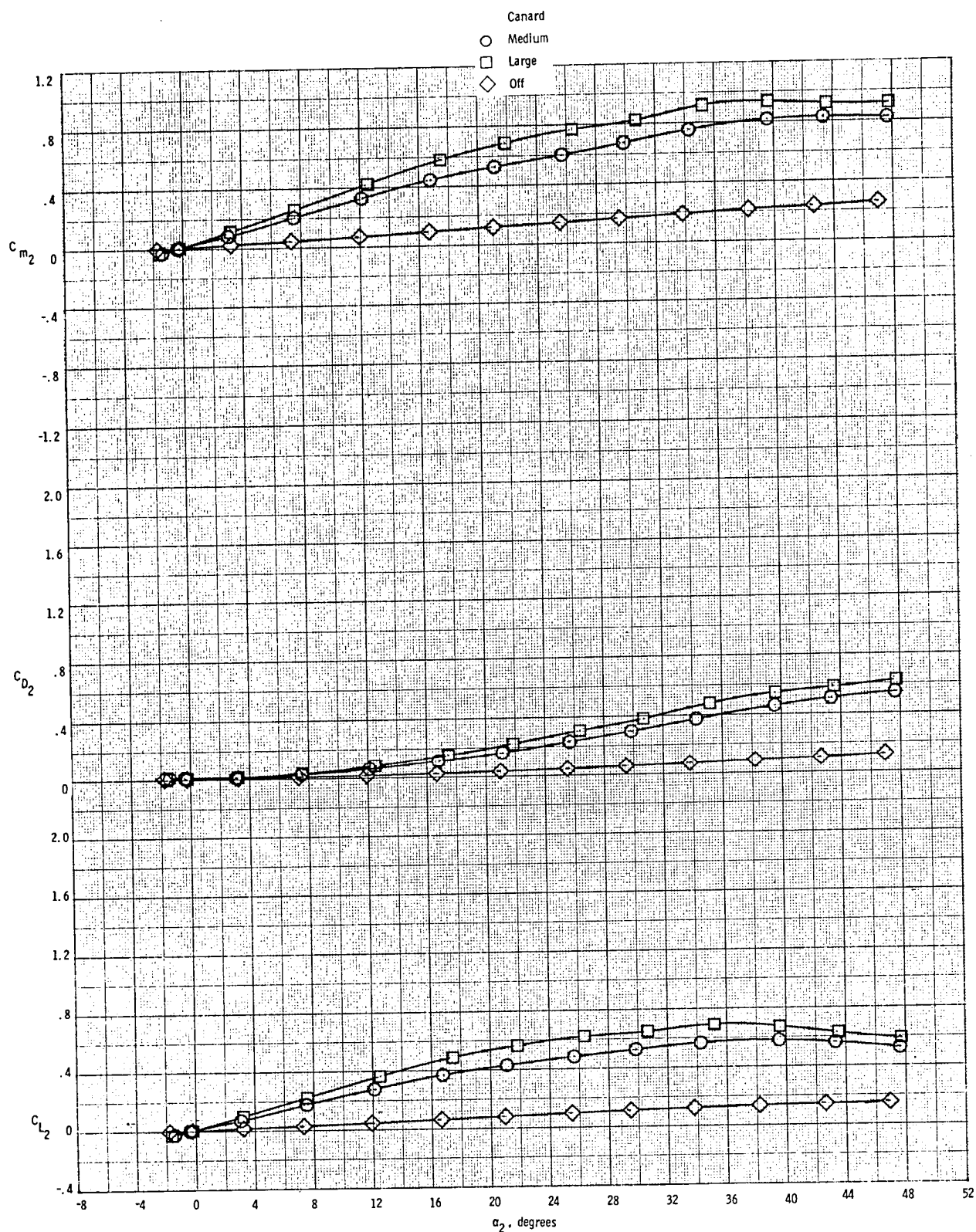
(c) Main balance lateral-directional data  
Figure 7.- Continued.



(d) Nose balance lateral-directional data  
Figure 7.- Concluded.

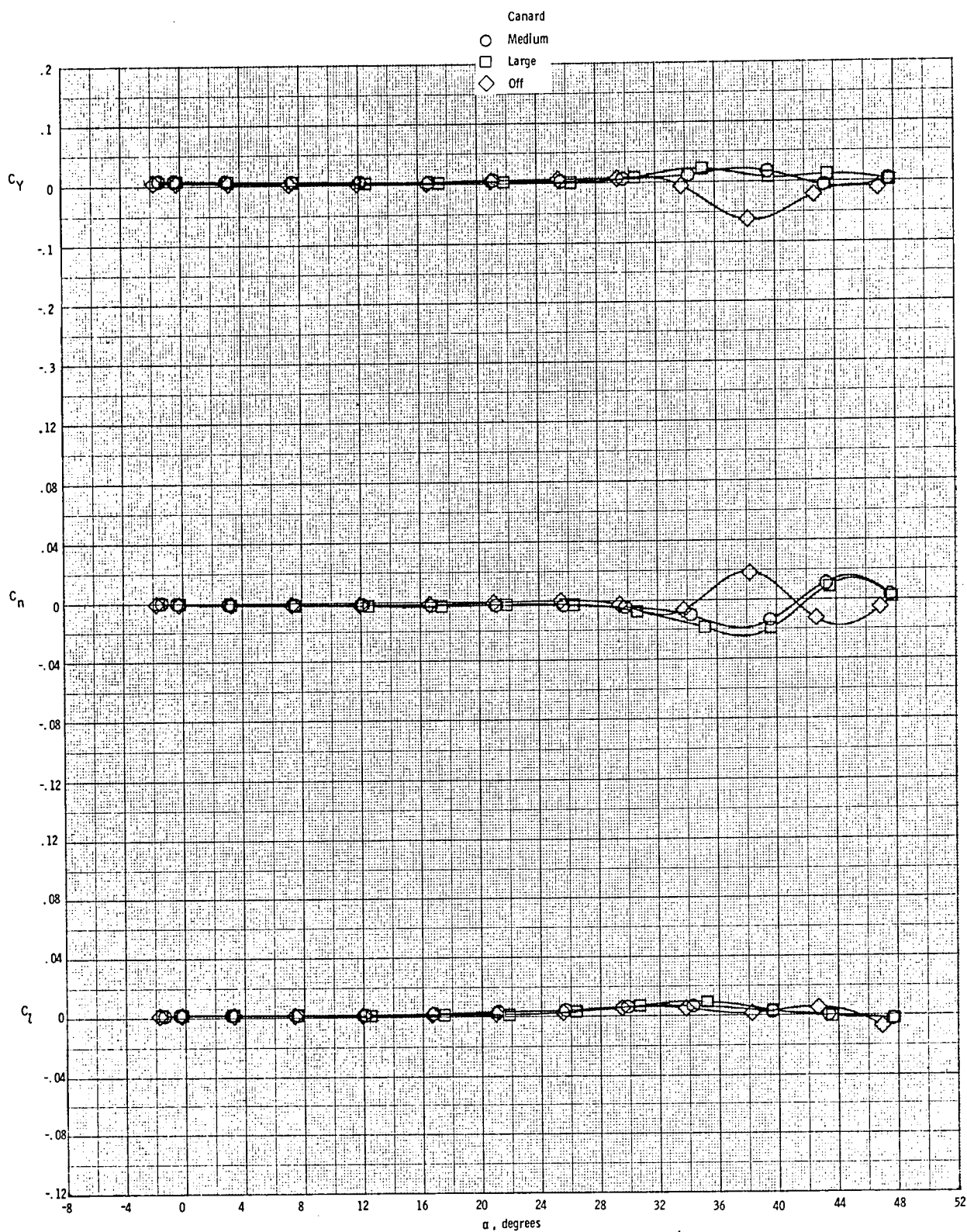


(a) Main balance longitudinal data  
 Figure 8.- Effect of canard size on the aerodynamic characteristics of the mid-wing high-canard configuration with the vertical tail on.  $M = 0.3$ ,  $\beta = 0^\circ$ .

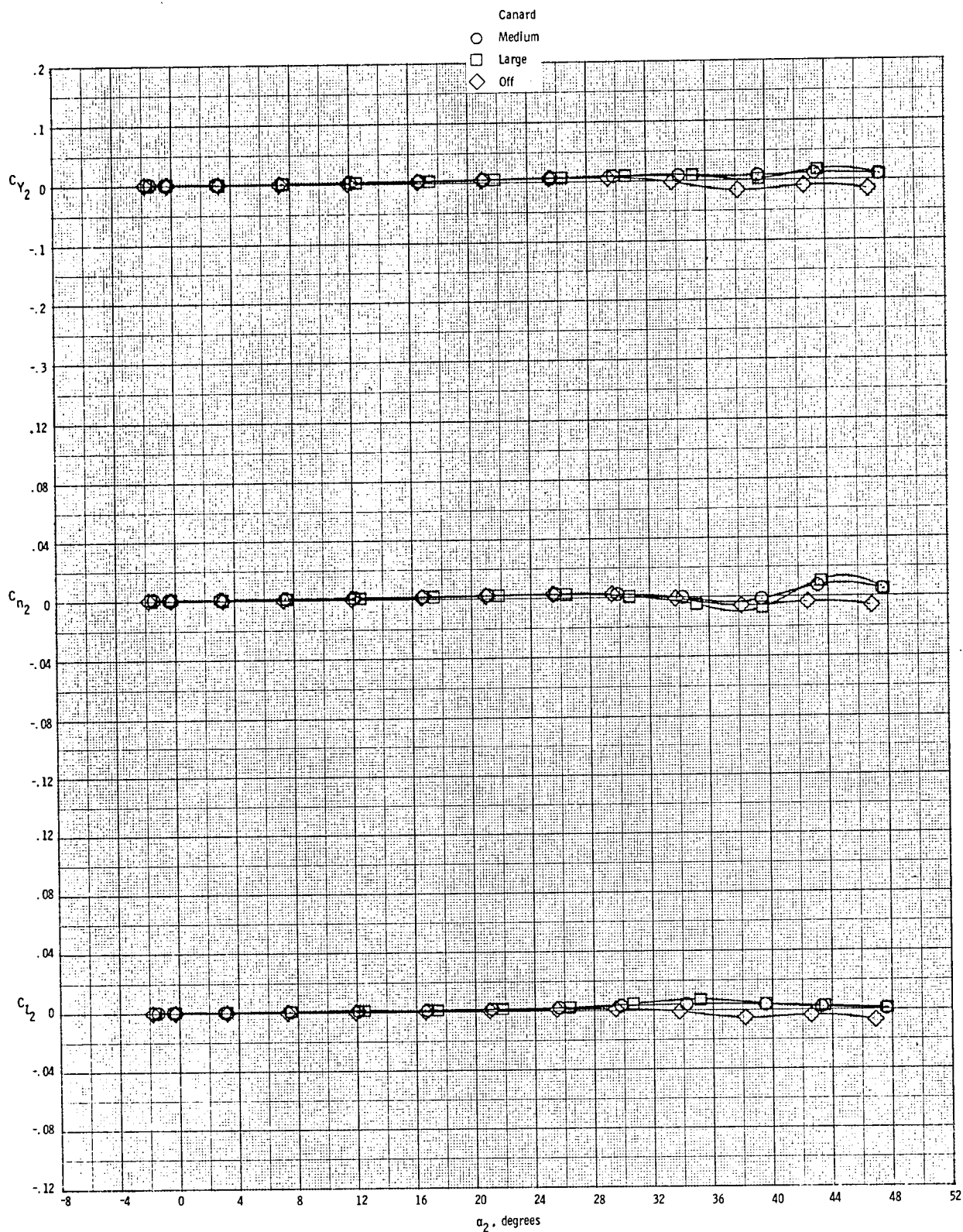


(b) Nose balance longitudinal data  
Figure 8. - Continued

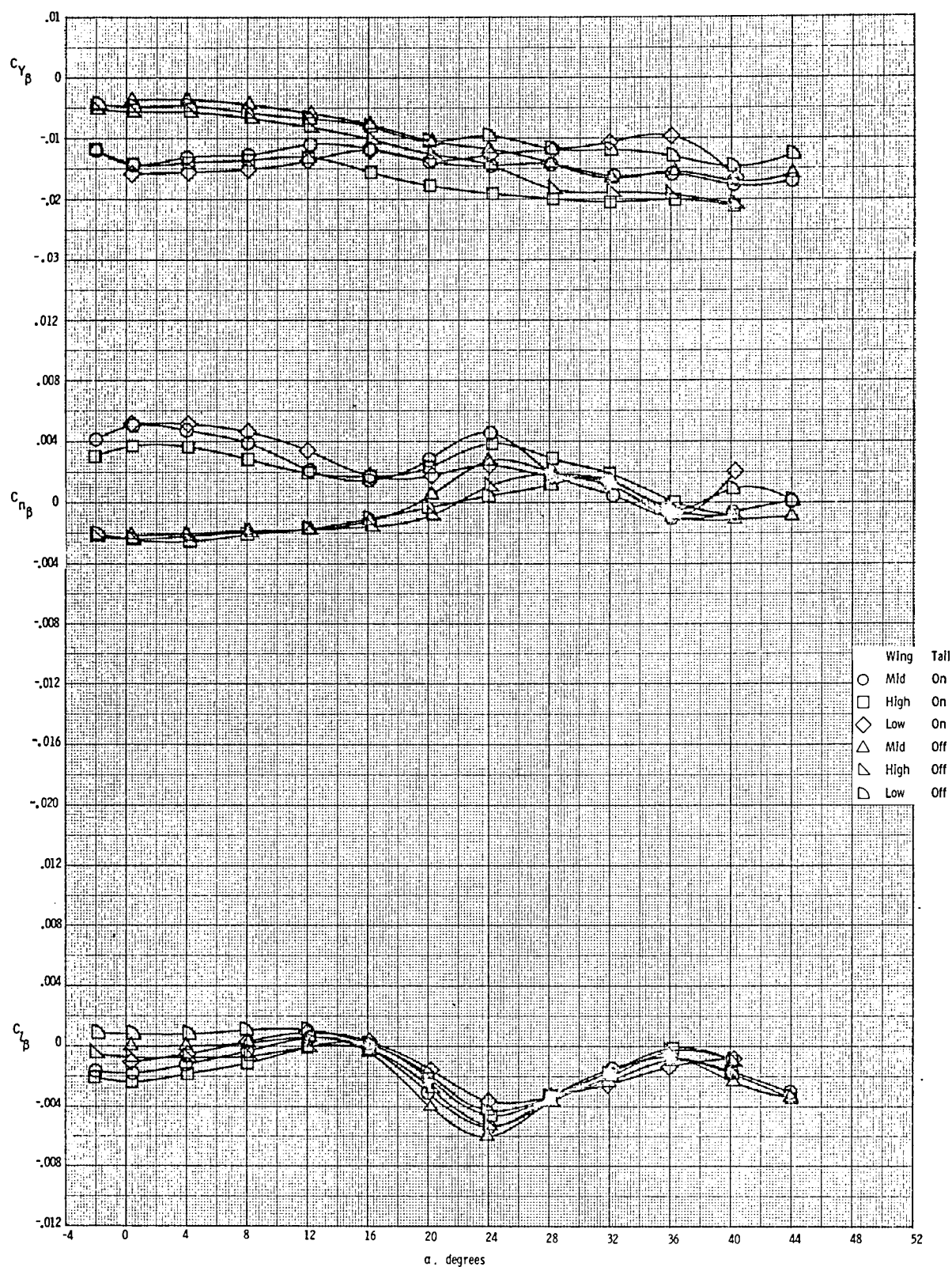




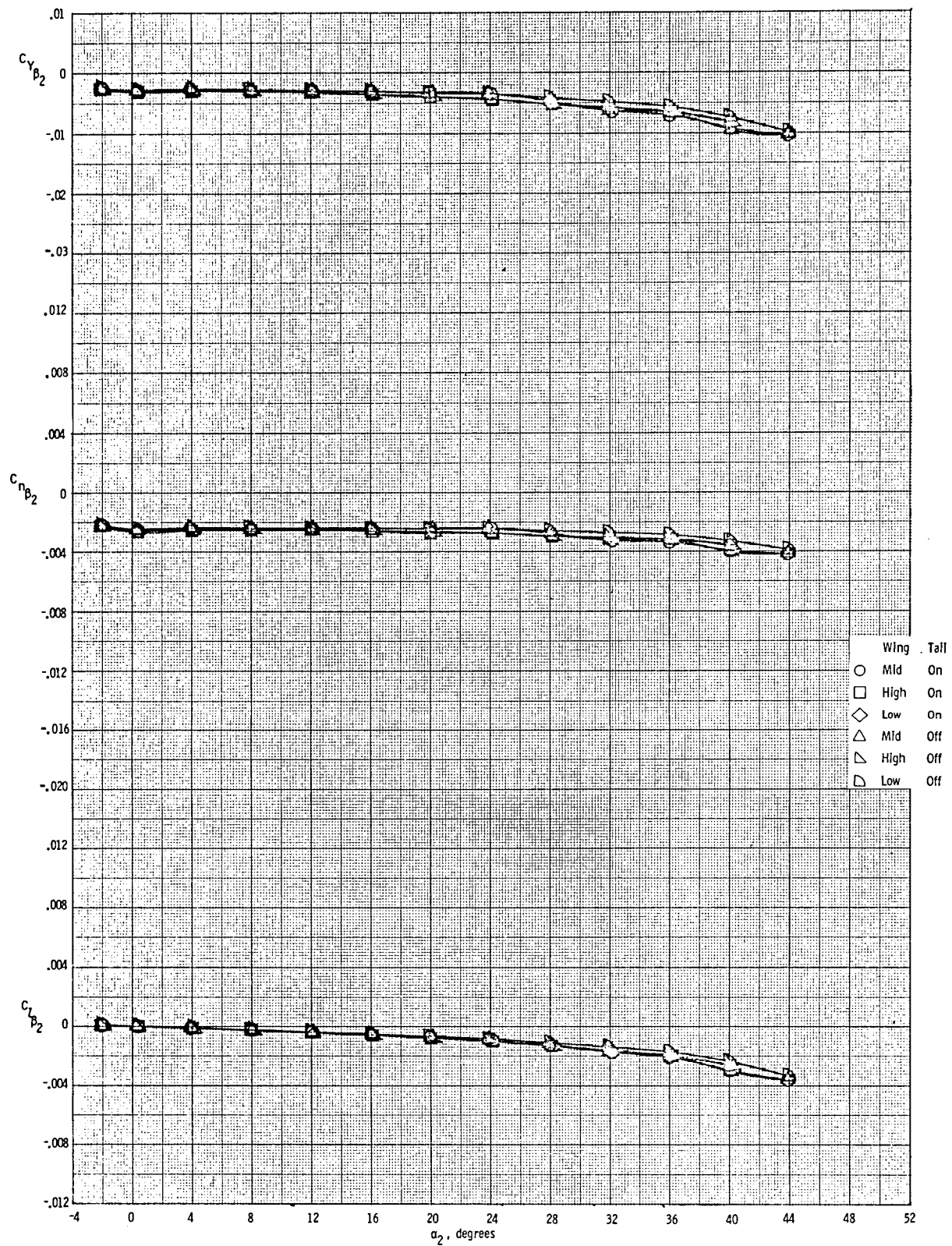
(c) Main balance lateral-directional data  
Figure 8.- Continued.



(d) Nose balance lateral-directional data  
Figure 8. - Concluded.

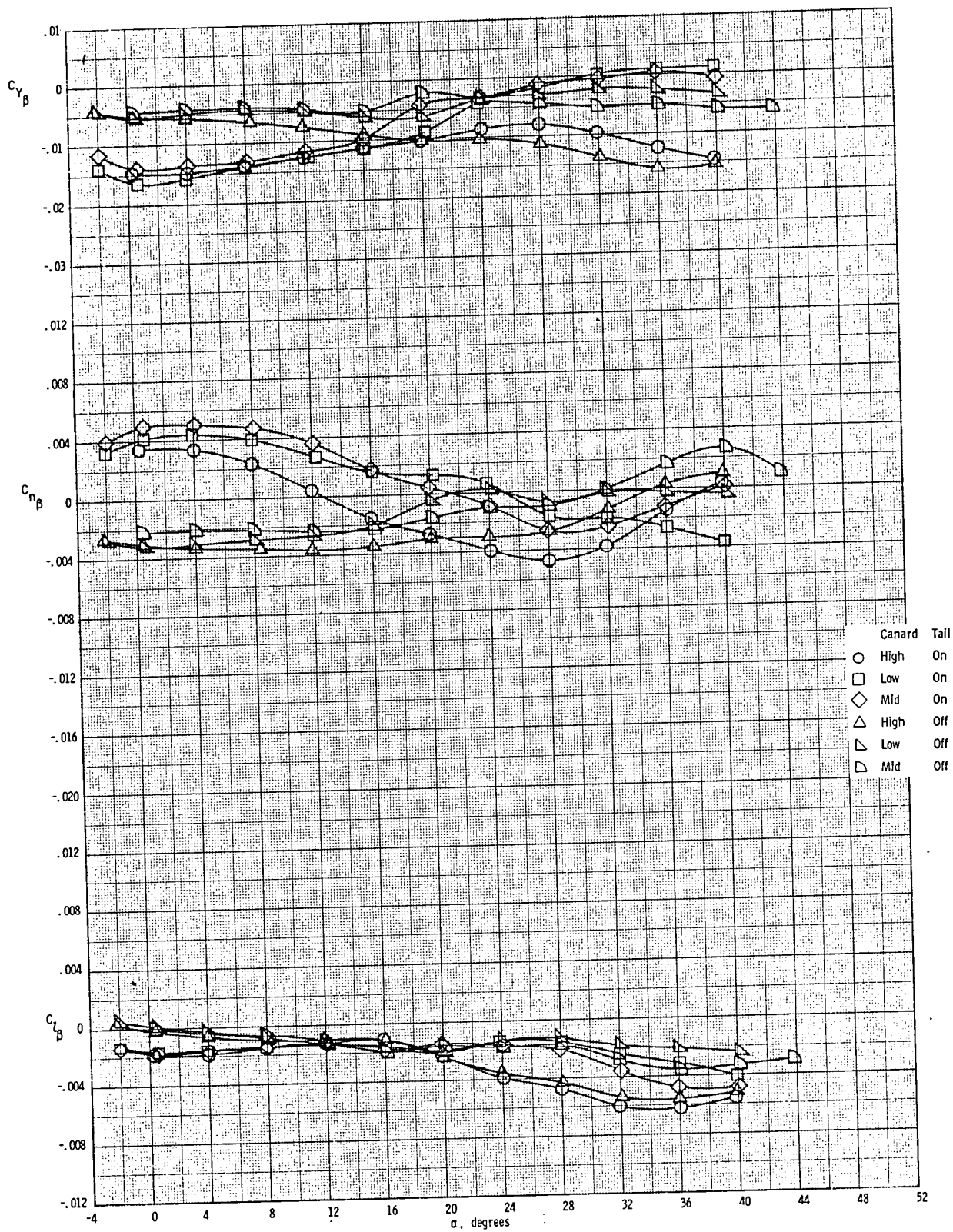


(a) Main balance data  
 Figure 9. - Effect of wing height on the lateral-directional aerodynamic stability derivative characteristics of the basic wing body configuration,  $M = 0.3$ .

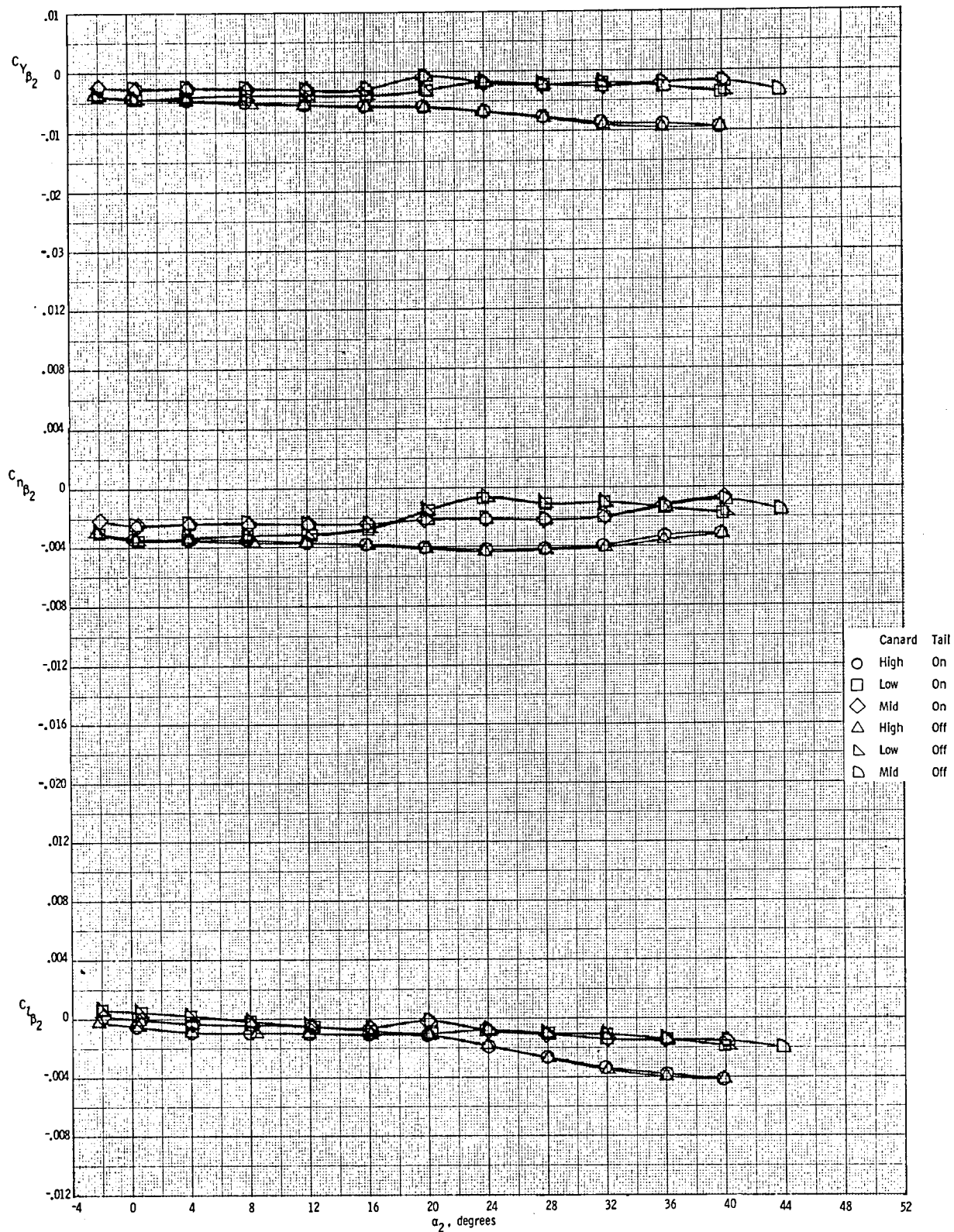


(b) Nose balance data  
Figure 9.- Concluded.

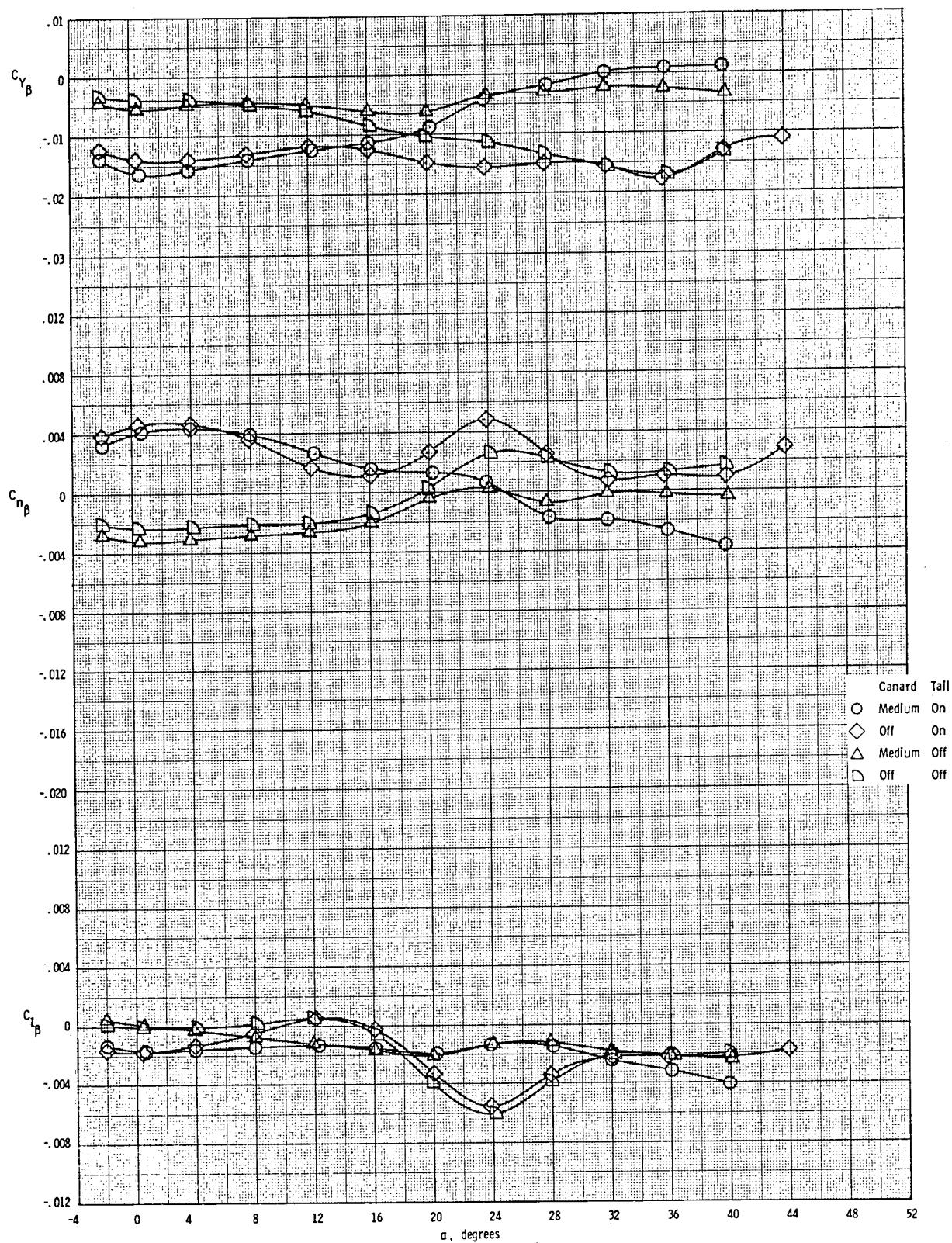




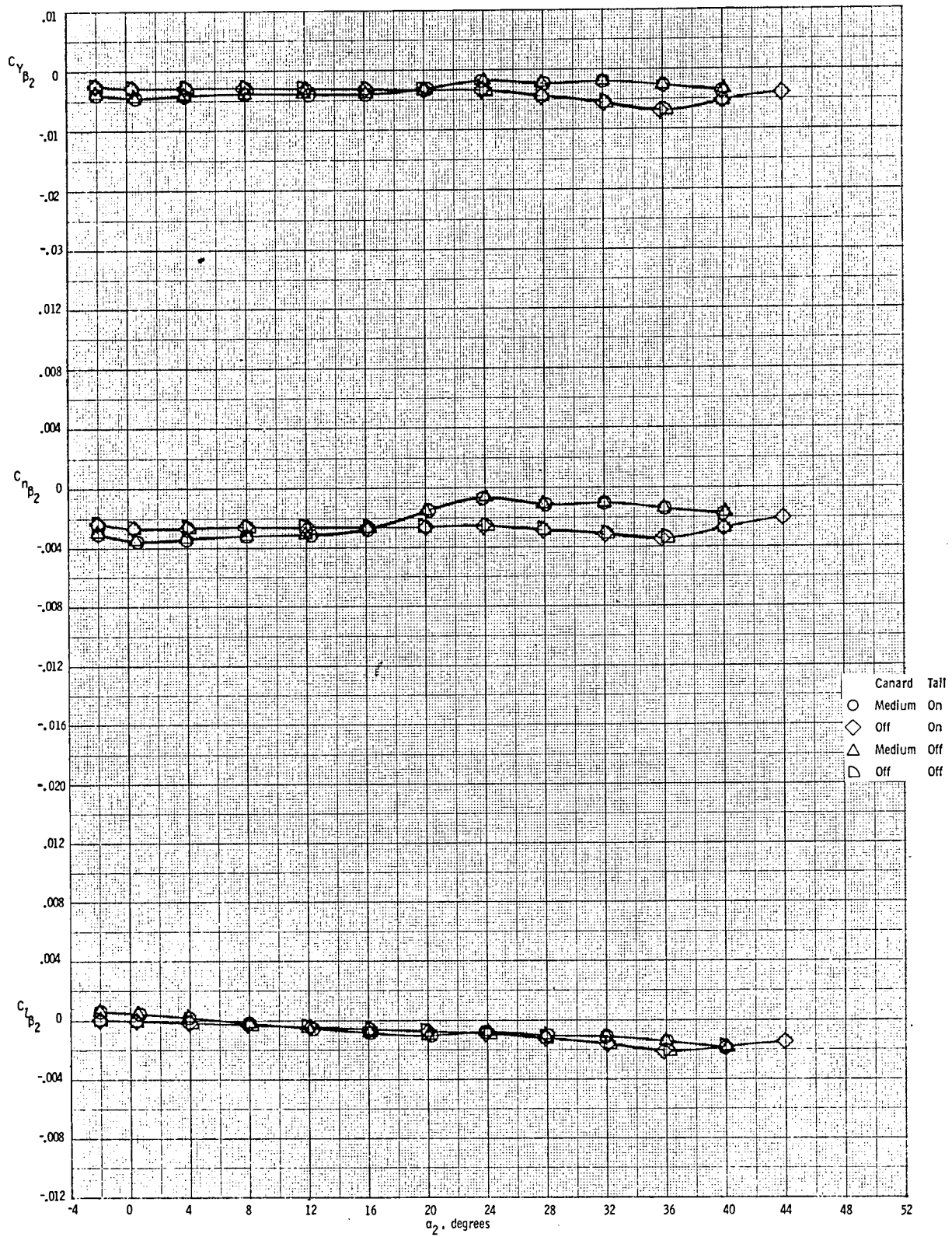
(a) Main balance data  
Figure 10.- Effect of canard height on the lateral-directional aerodynamic stability derivative characteristics of the mid-wing medium canard configuration.  $M = 0.3$ .



(b) Nose balance data  
Figure 10.- Concluded

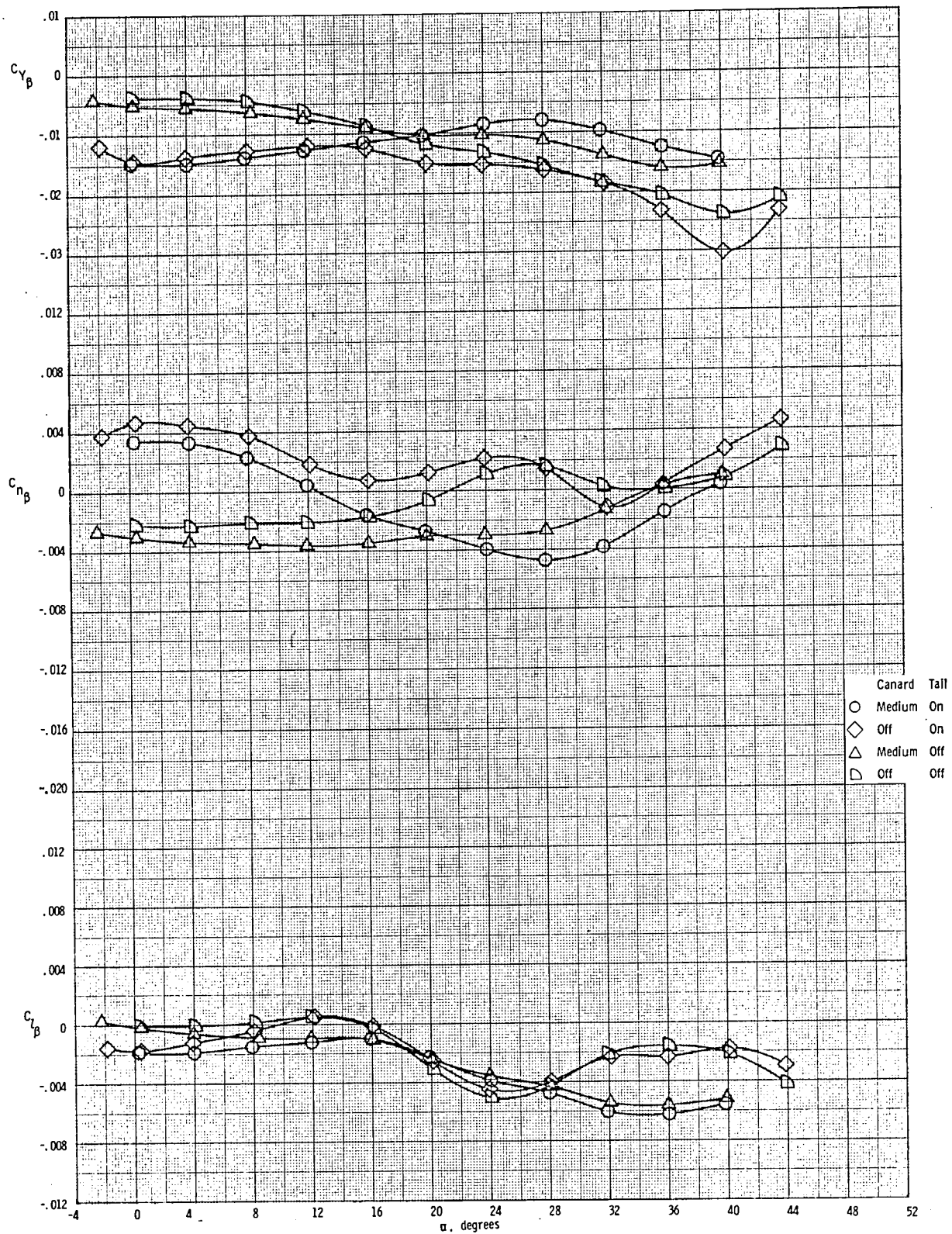


(a) Main balance data  
 Figure 11.- Effect of component breakdown on the lateral-directional aerodynamic stability derivative characteristics of the mid-wing low canard configuration, -  $M = 0.3$ .

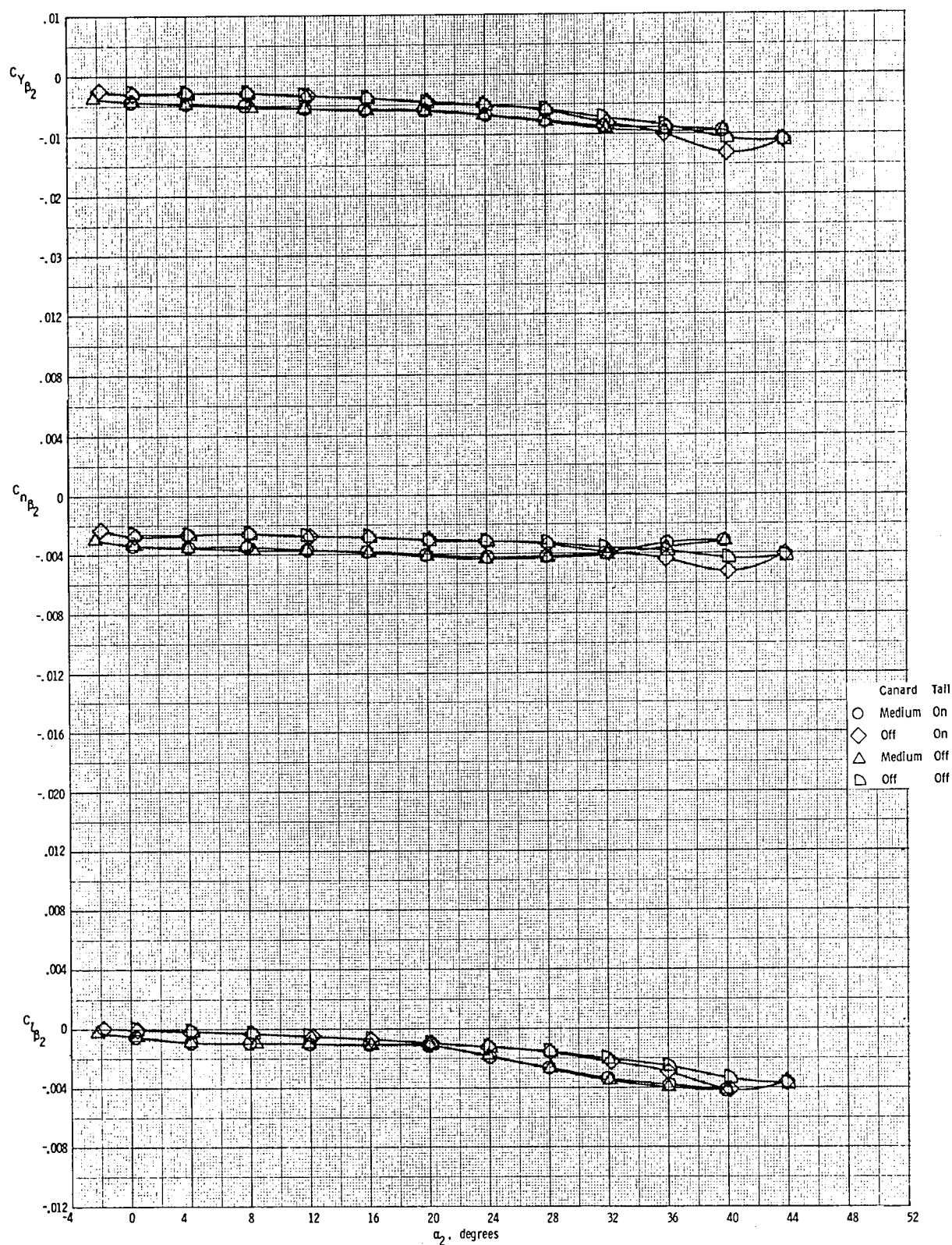


(b) Nose balance data  
Figure II.- Concluded.

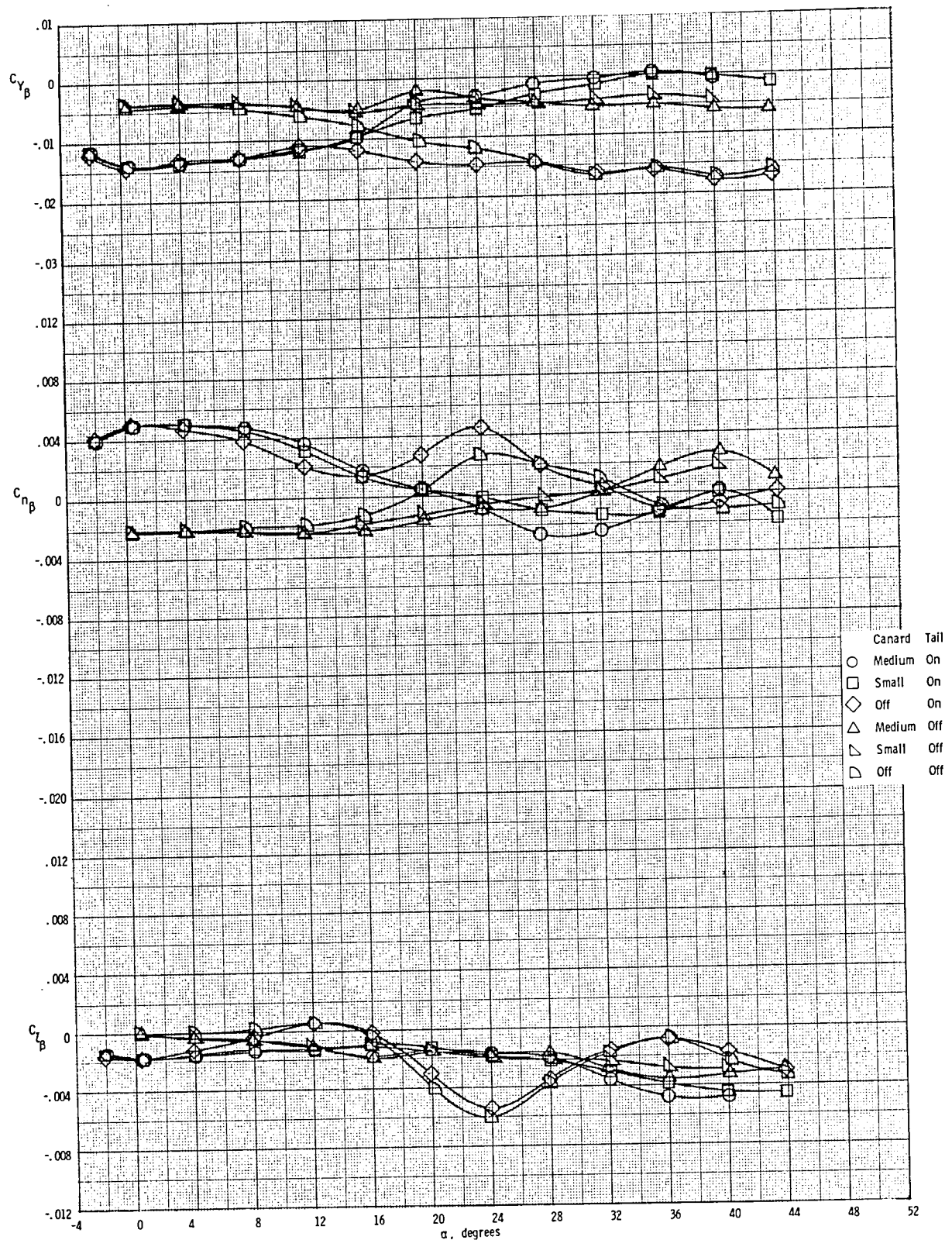




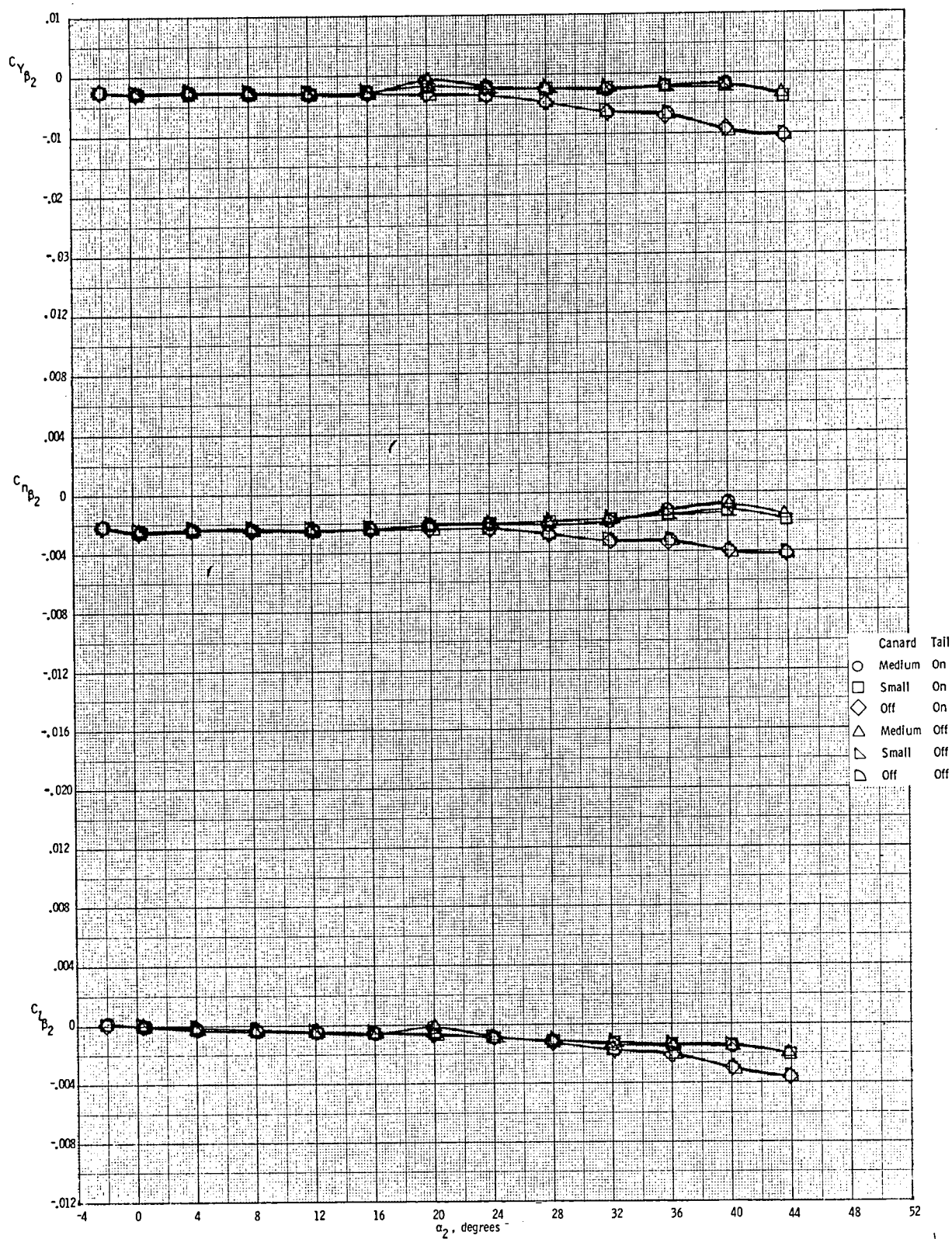
(a) Main balance data  
 Figure 12, - Effect of component breakdown on the lateral-directional aerodynamic stability derivative characteristics of the mid-wing high canard configuration.  $M = 0.3$ .



(b) Nose balance data  
 Figure 12.- Concluded.

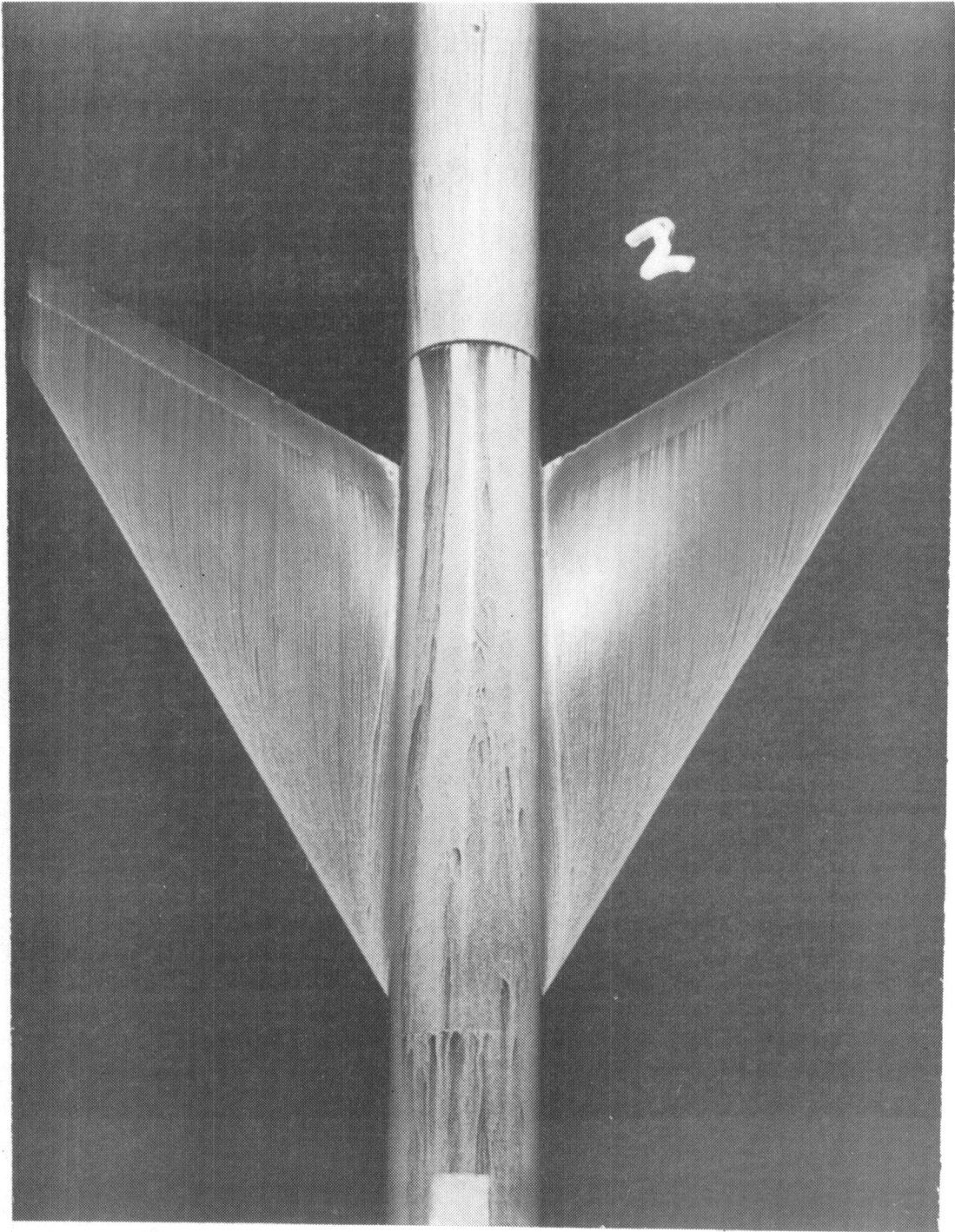


(a) Main balance data  
 Figure 13. - Effect of canard size on the lateral-directional aerodynamic stability derivative characteristics of the mid-wing mid-canard configuration,  $M = 0.3$ .



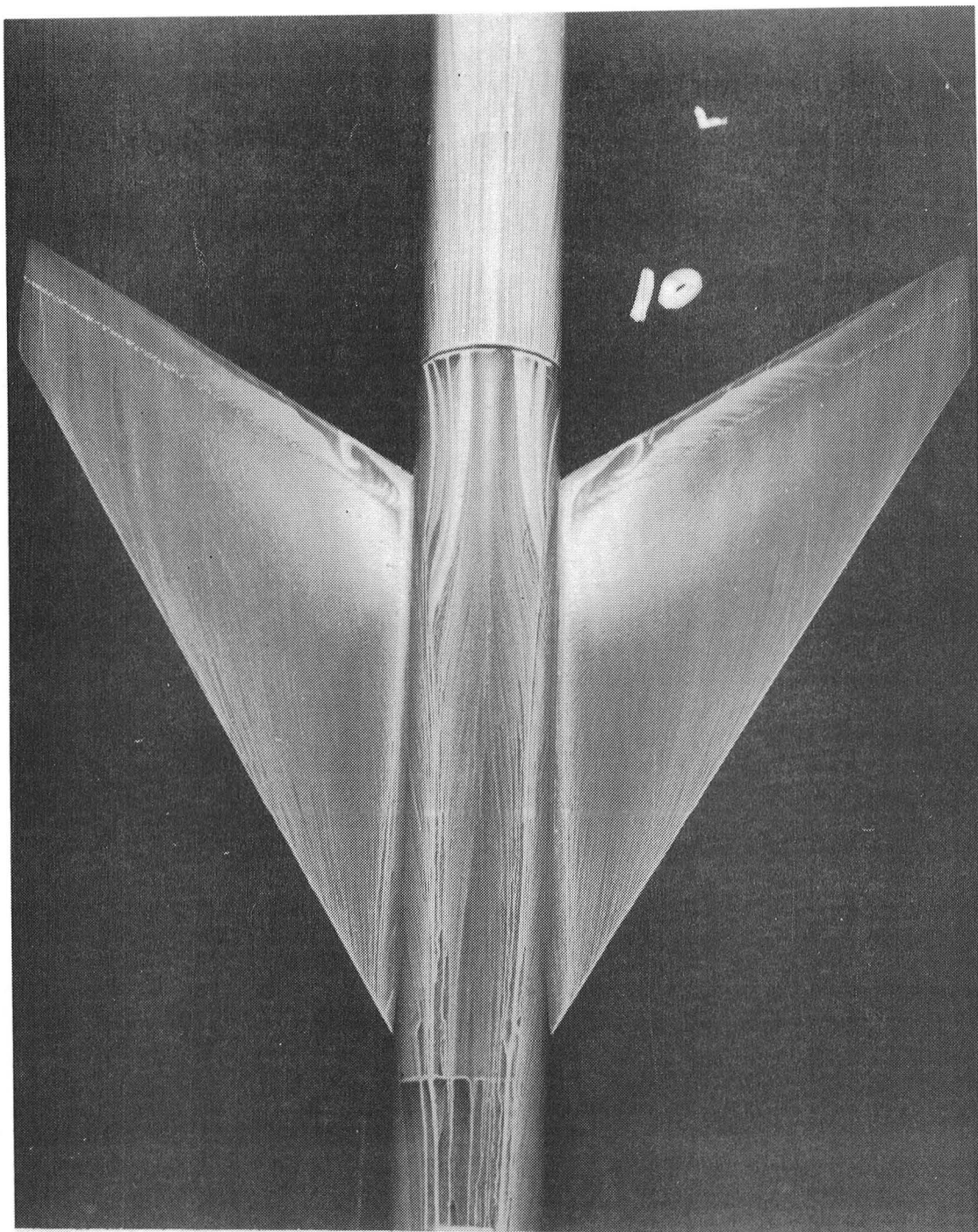
(b) Nose balance data  
Figure 13.- Concluded.



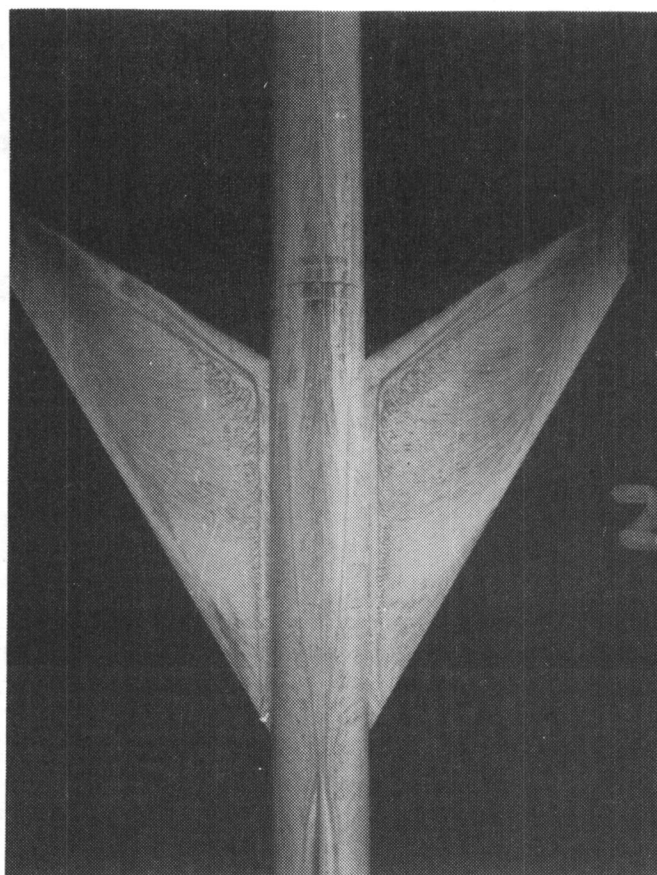


(a)  $\alpha=3^0$ , plan view

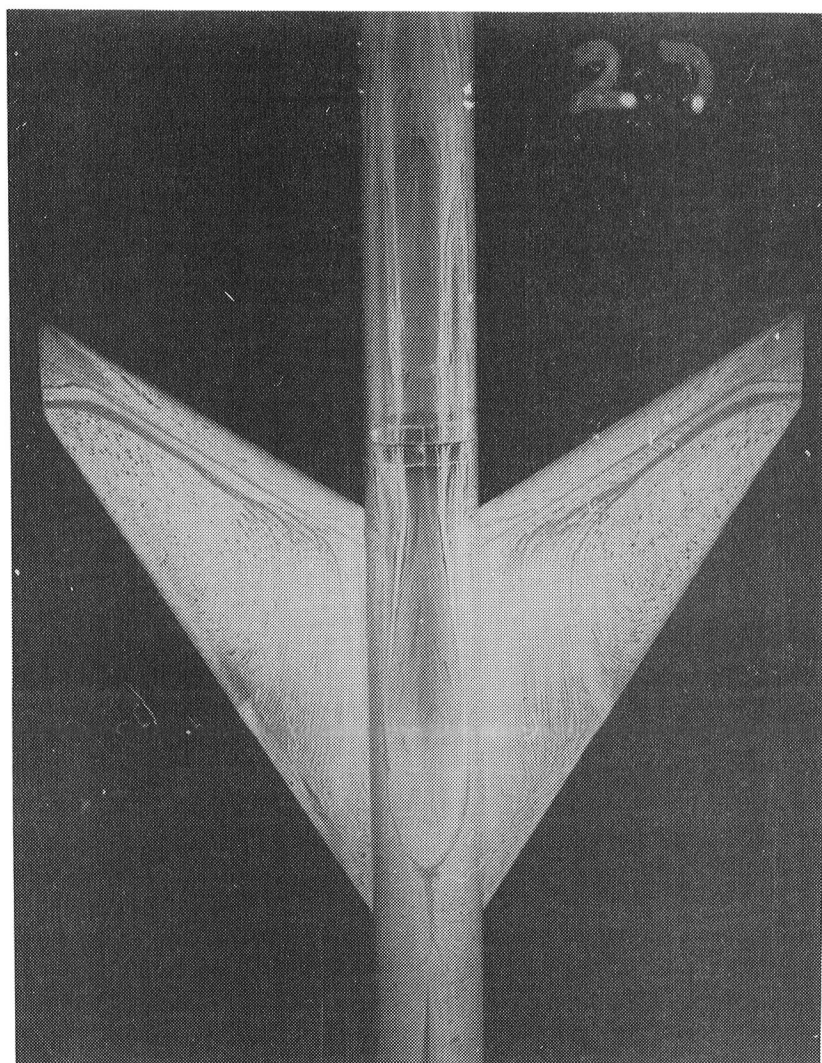
Figure 14.- Surface oil flow photographs of the basic mid-wing configuration.  $M=0.3$ .



(b)  $\alpha=7^\circ$ , plan view  
Figure 14. - Continued.

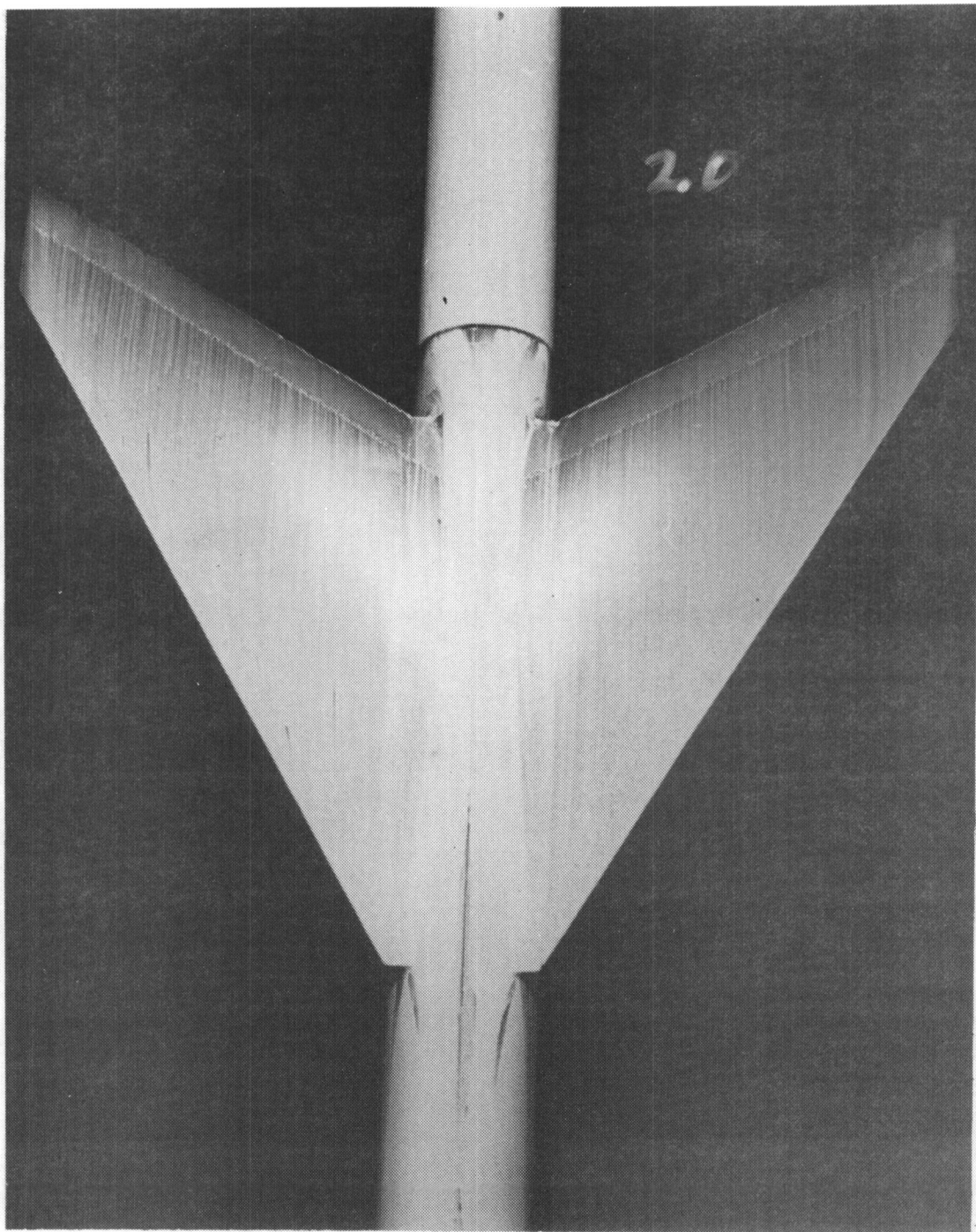


(c)  $\alpha=15^\circ$ , plan view  
Figure 14.- Continued.



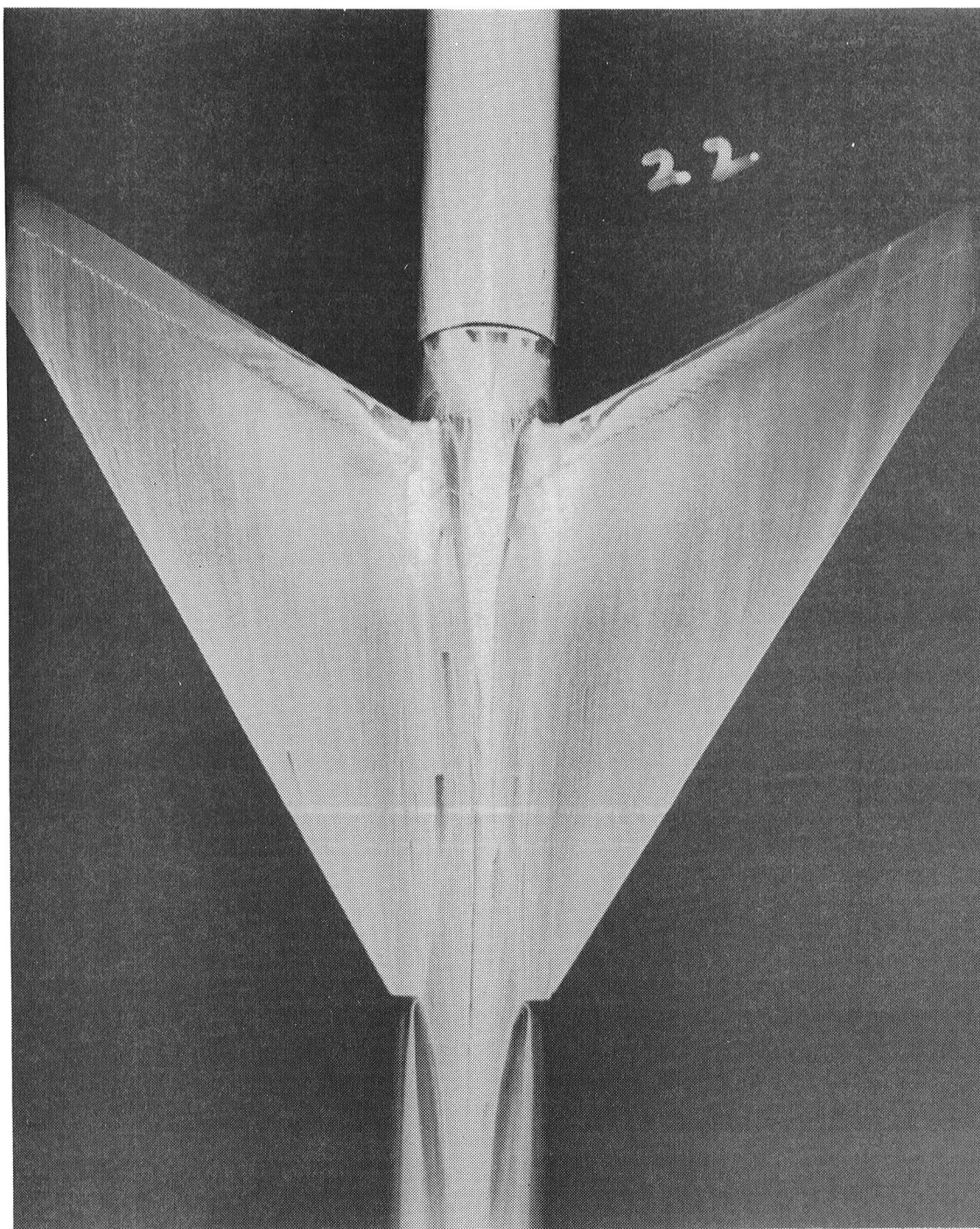
(d)  $\alpha=30^0$ , plan view  
Figure 14.- Concluded.





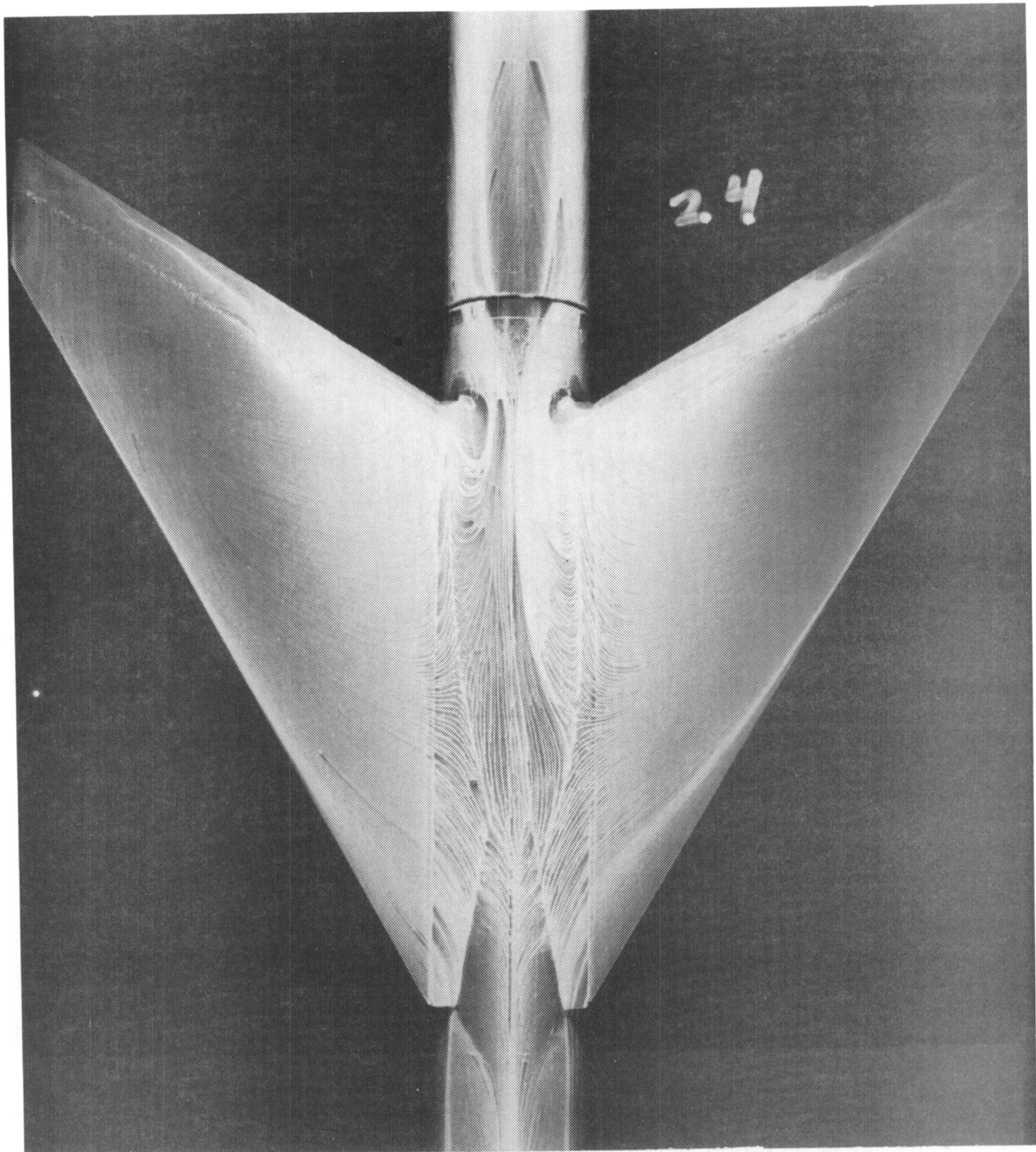
(a)  $\alpha=3^\circ$ , plan view

Figure 15.- Surface oil flow photographs of the basic high-wing configuration.  $M=0.3$ .

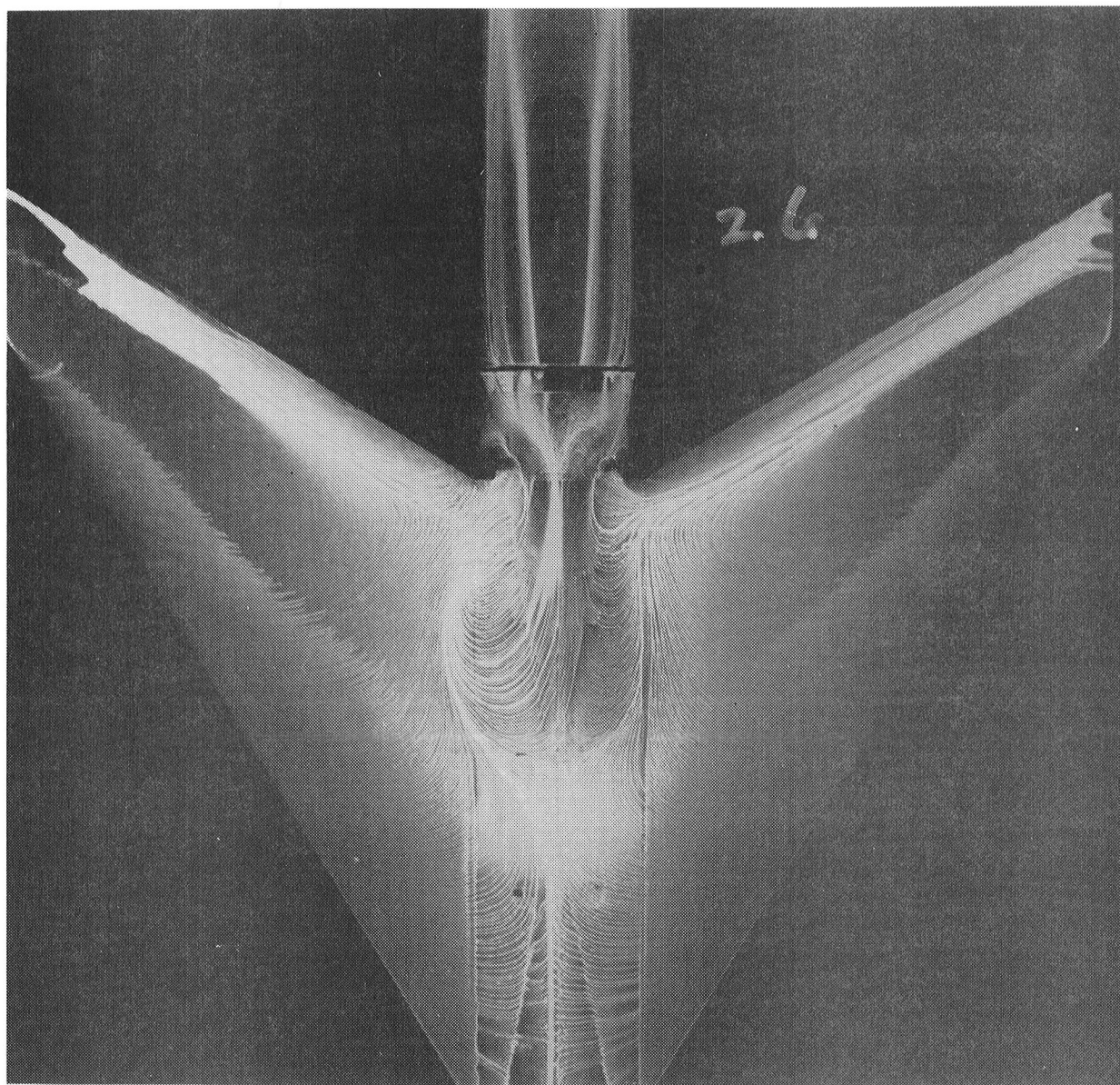


(b)  $\alpha=7^0$ , plan view  
Figure 15.- Continued.

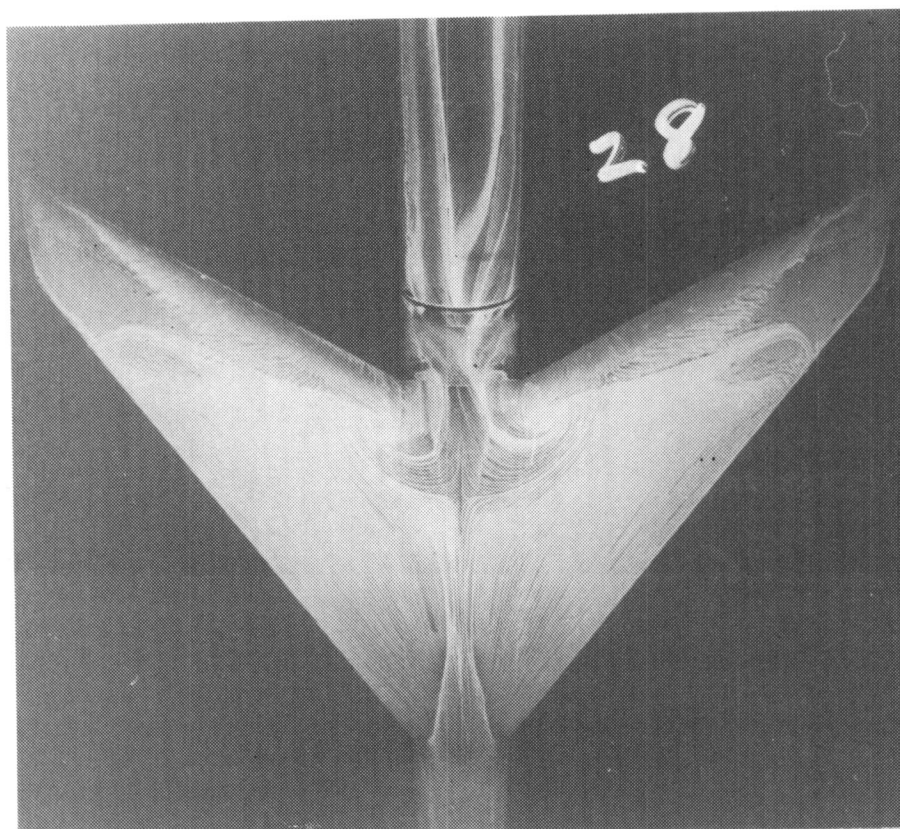




(c)  $\alpha=15^\circ$ , plan view  
Figure 15. - Continued.

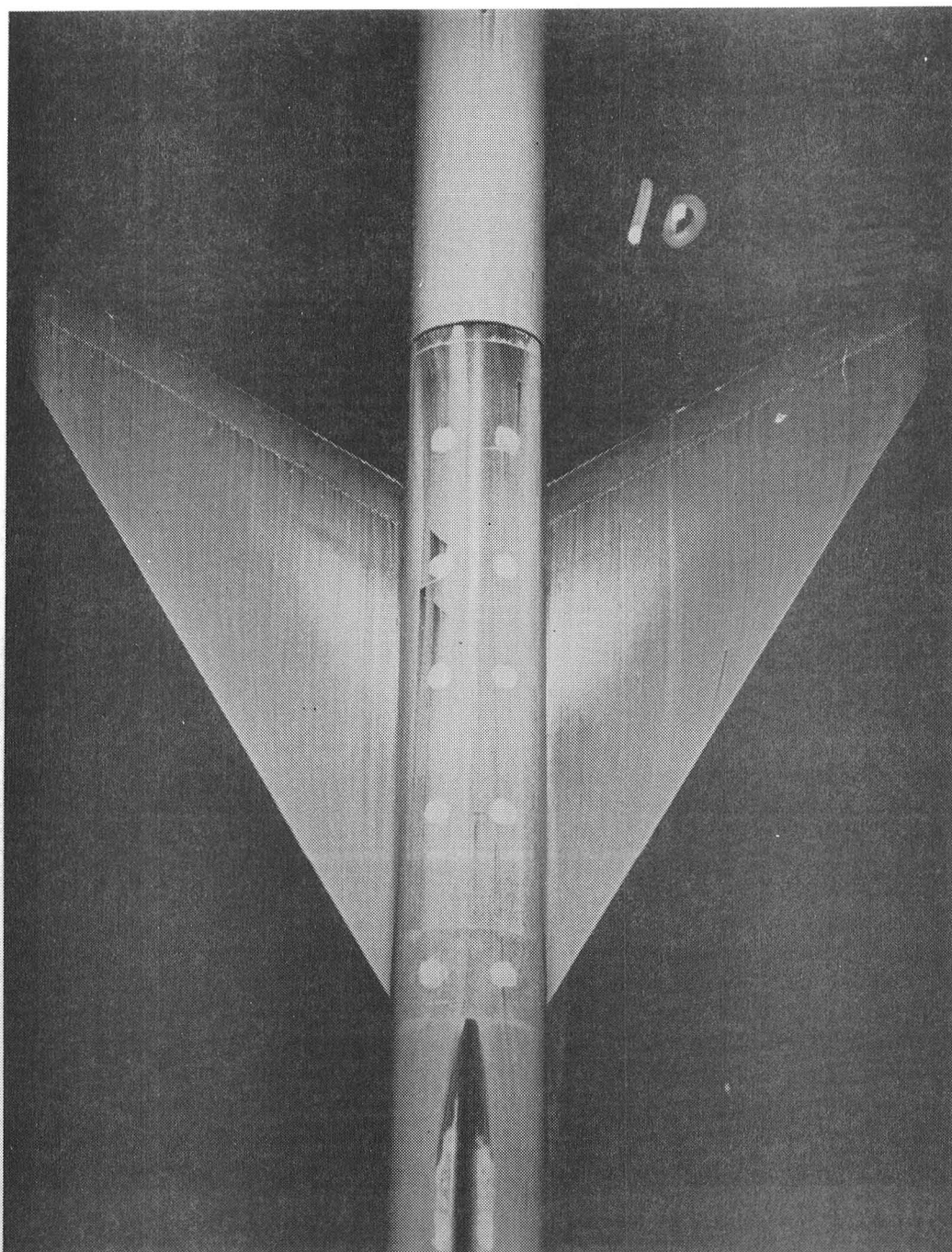


(d)  $\alpha=25^0$ , plan view  
Figure 15. - Continued.



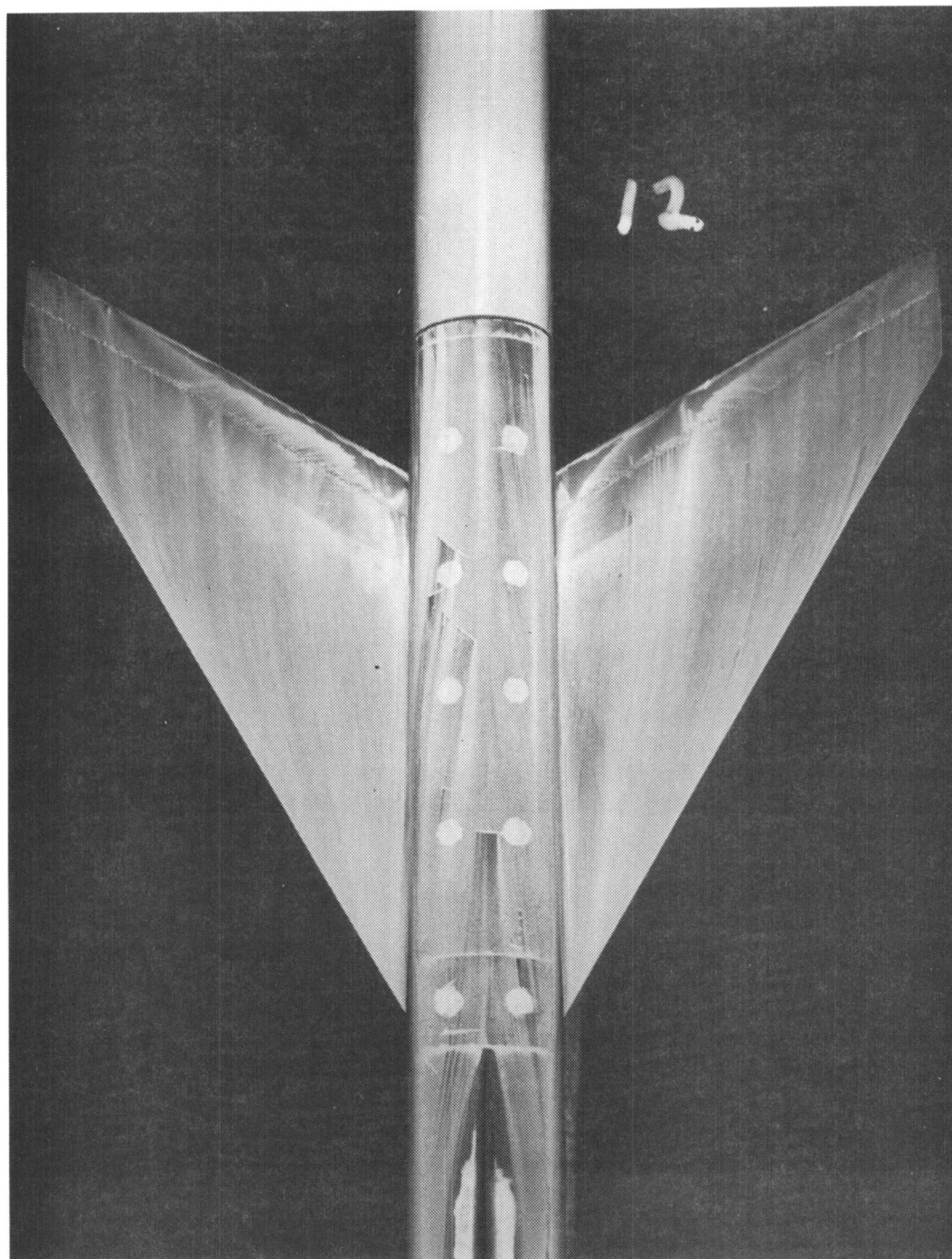
(e)  $\alpha=40^\circ$ , plan view  
Figure 15. - Concluded.





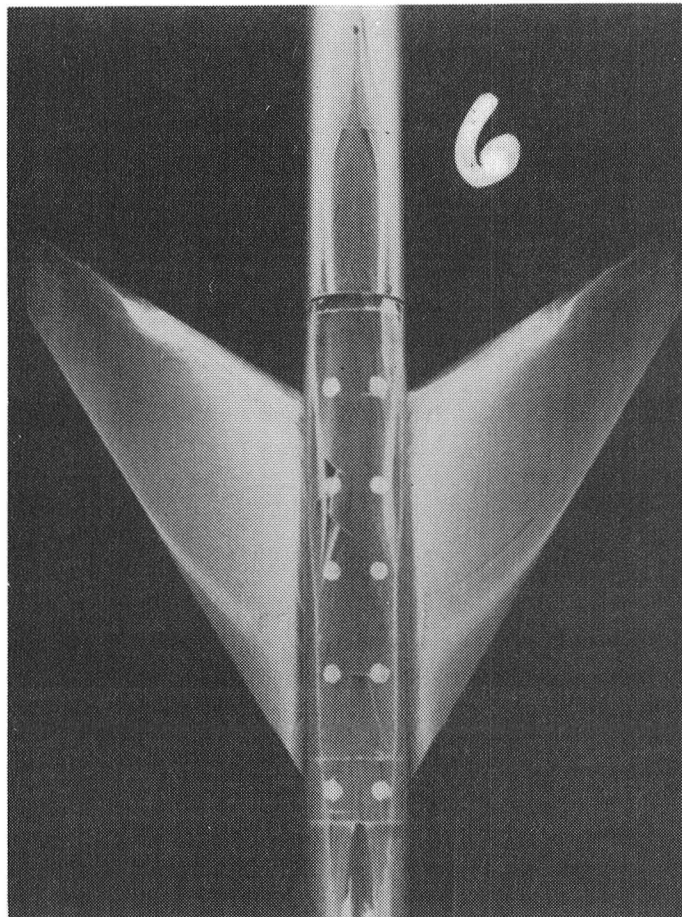
(a)  $\alpha=3^0$ , plan view

Figure 16.- Surface oil flow photographs of the basic low-wing configuration.  $M=0.3$ .

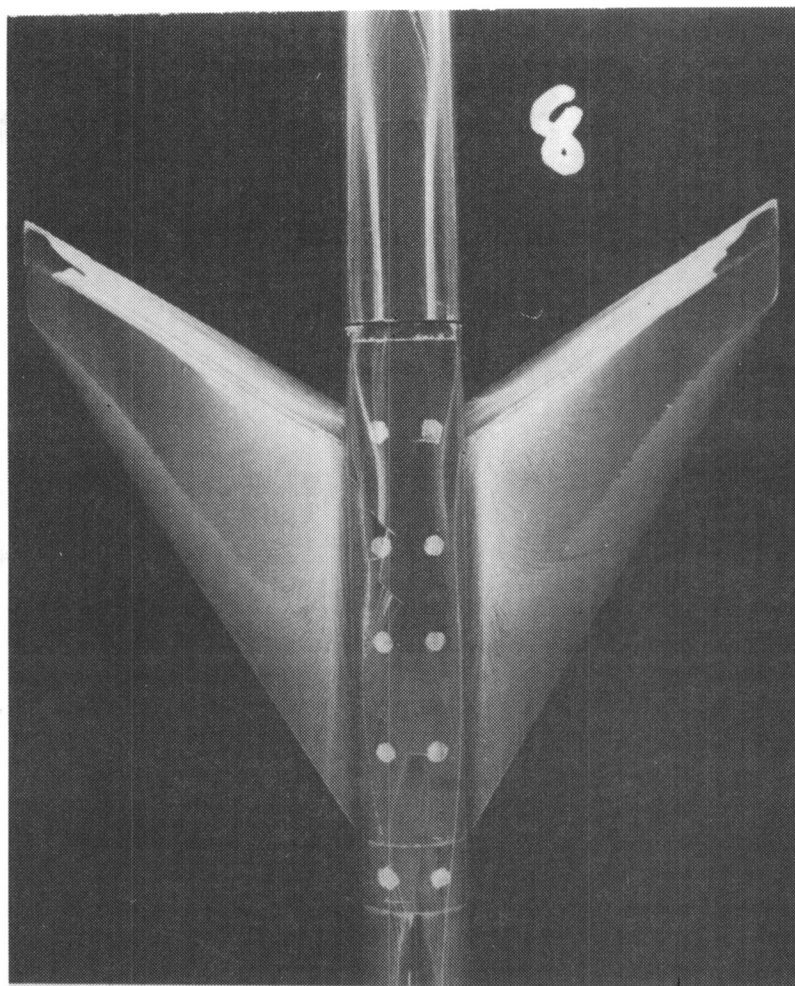


(b)  $\alpha=7^\circ$ , plan view  
Figure 16. - Continued.

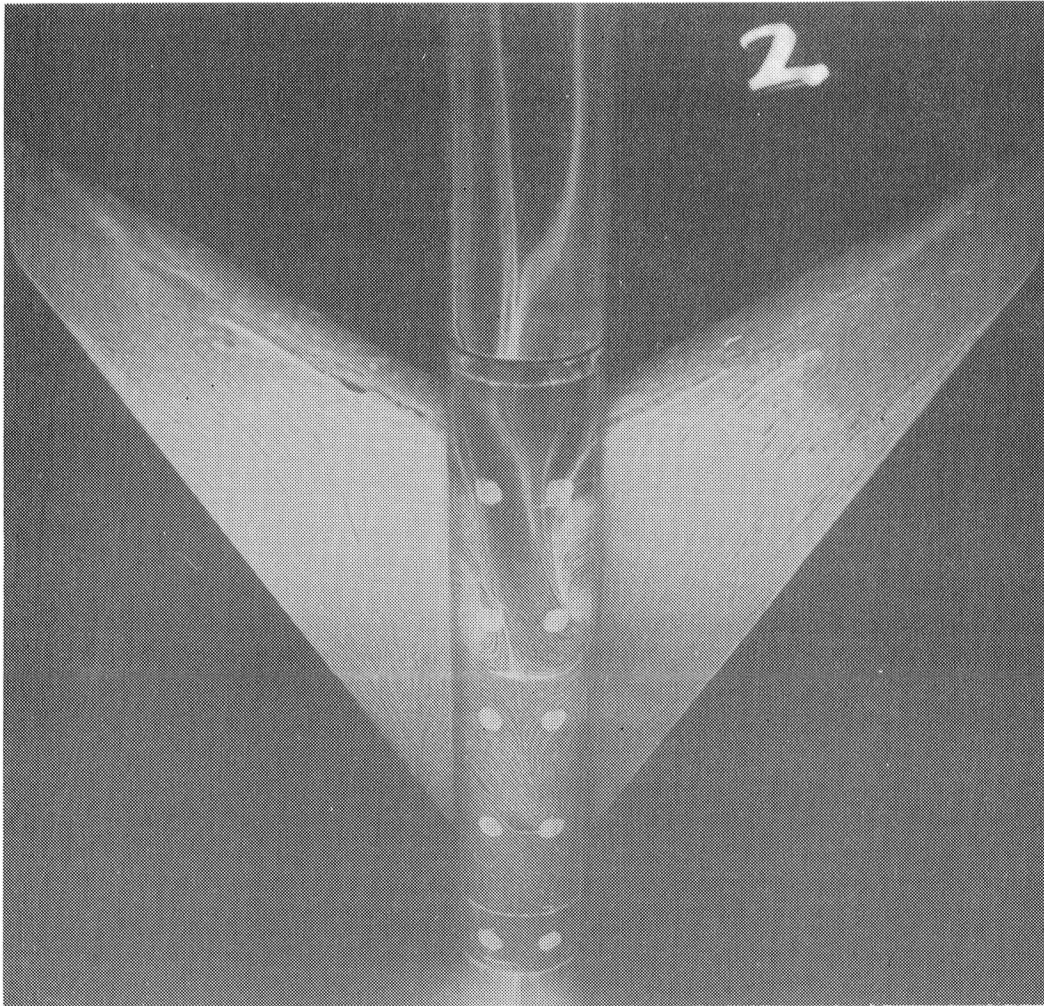




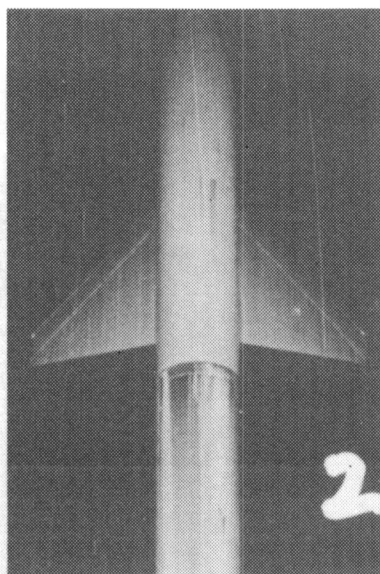
(c)  $\alpha=15^0$ , plan view  
Figure 16. - Continued.



(d)  $\alpha=25^{\circ}$ , plan view  
Figure 16. - Continued.

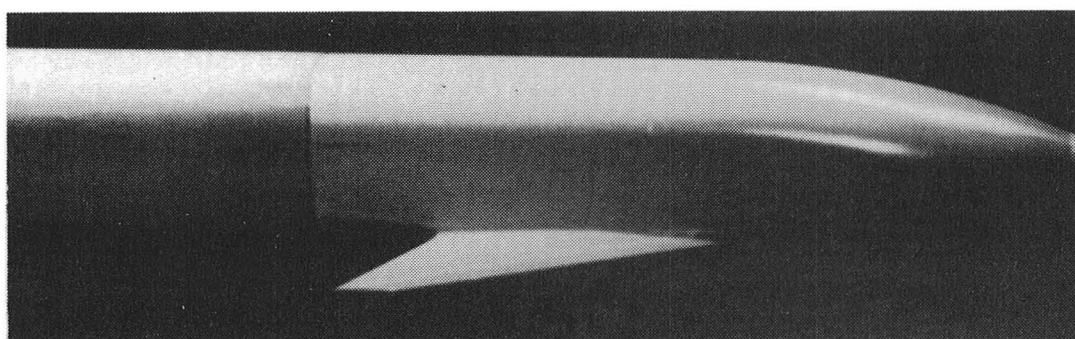


(e)  $\alpha=40^{\circ}$ , plan view  
Figure 16.- Concluded.

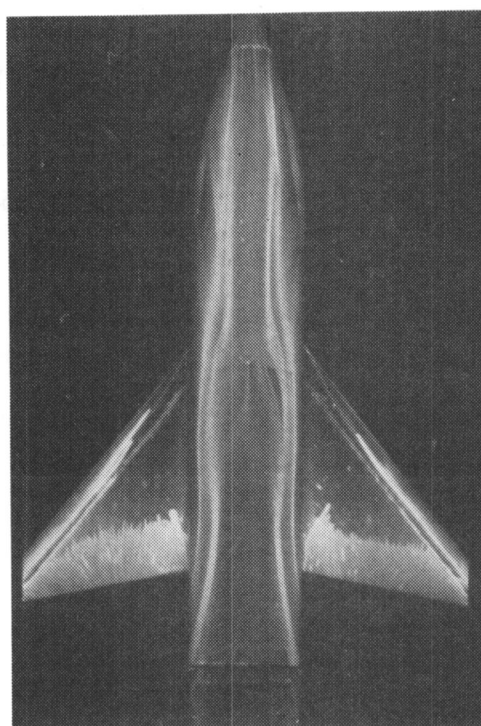


(a)  $\alpha=3^0$ , plan view

Figure 17.- Surface oil flow photographs of the basic medium size low-canard configuration.  $M=0.3$ .

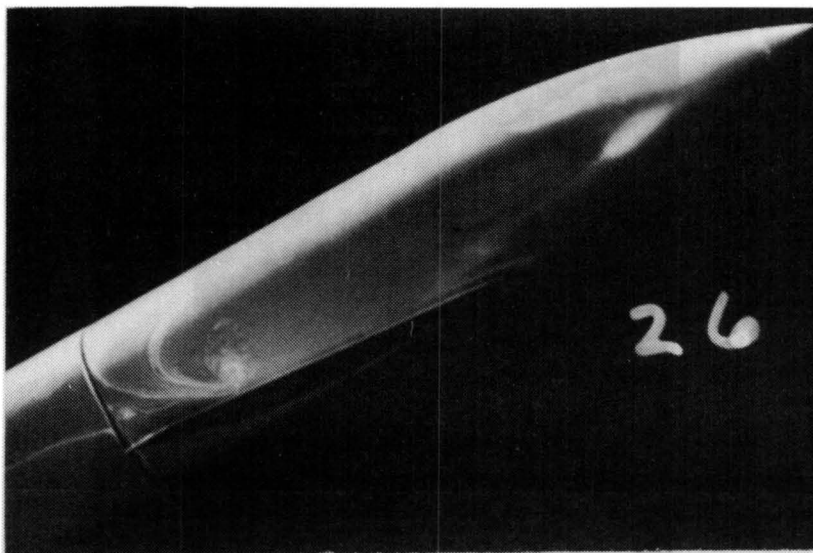


(b)  $\alpha=3^{\circ}$ , side view  
Figure 17.- Continued.



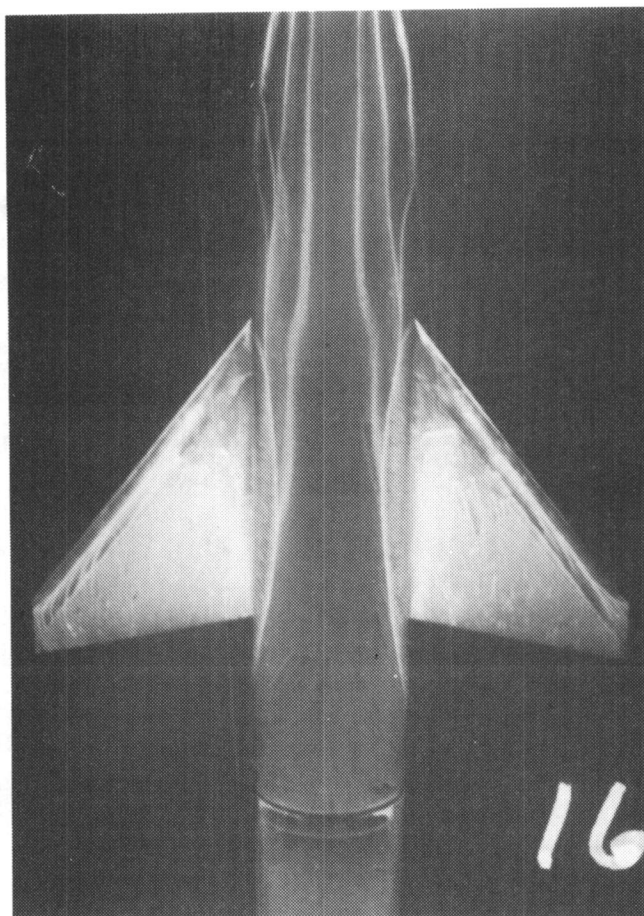
(c)  $\alpha=25^\circ$ , plan view  
Figure 17.- Continued.





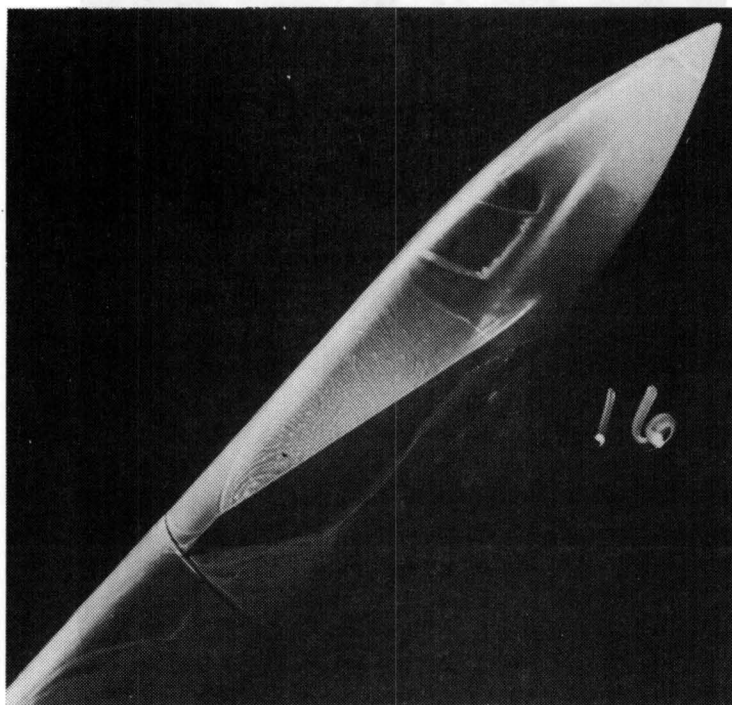
(d)  $\alpha=25^0$ , side view  
Figure 17.- Continued.



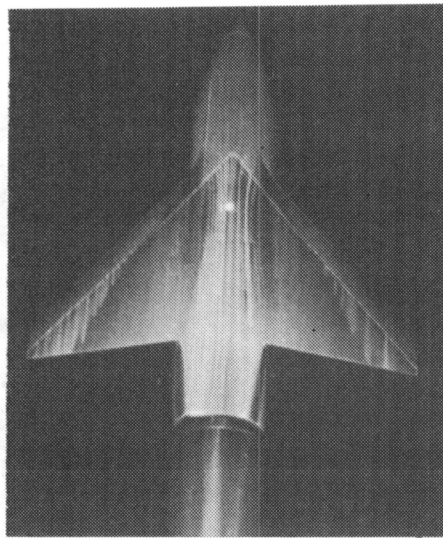


(e)  $\alpha=40^{\circ}$ , plan view

Figure 17. - Continued.

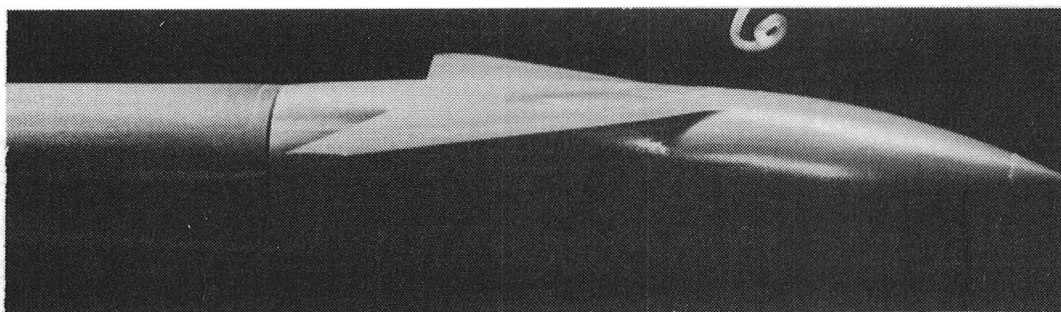


(f)  $\alpha=40^{\circ}$ , side view  
Figure 17. - Concluded.

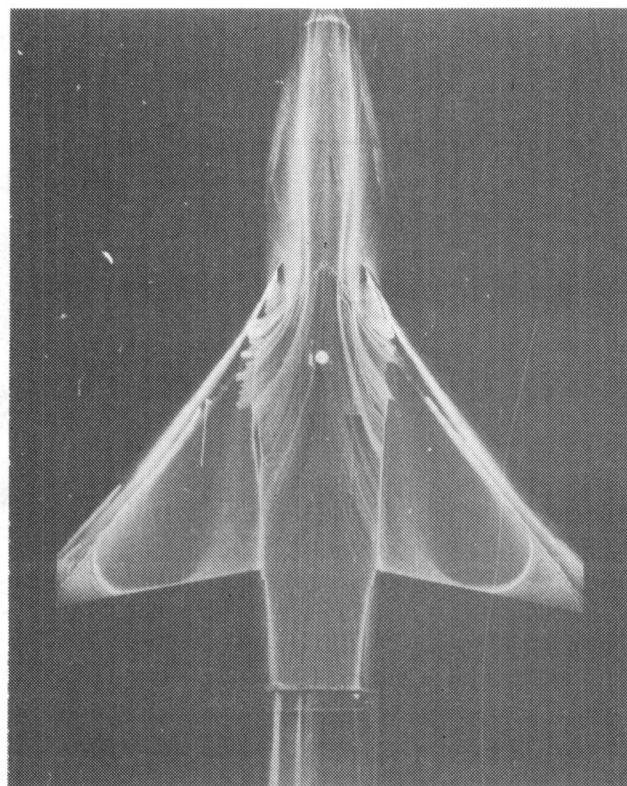


(a)  $\alpha=3^{\circ}$ , plan view

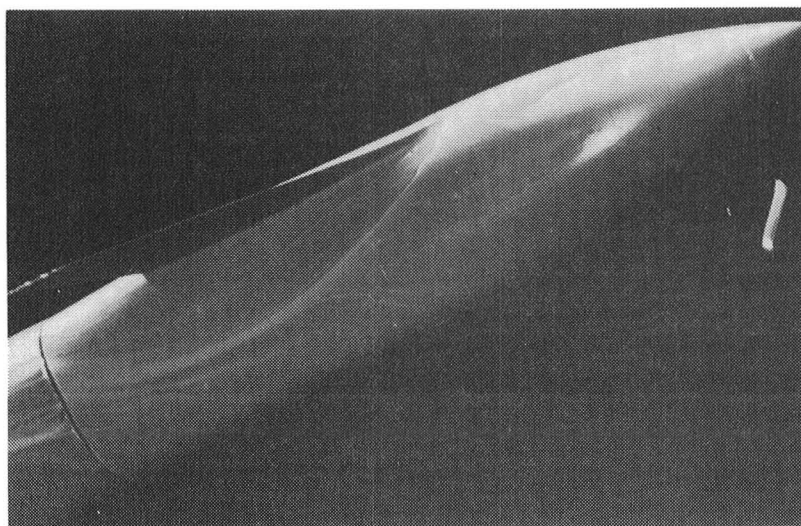
Figure 18.- Surface oil flow photographs of the basic medium size high-canard configuration.  $M=0.3$ .



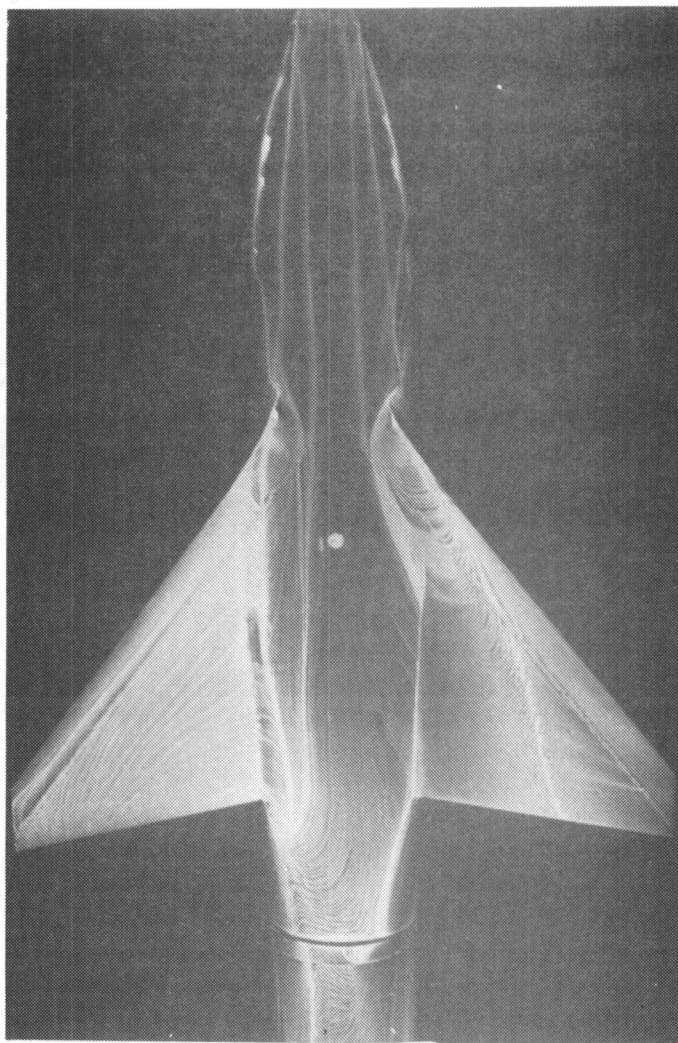
(b)  $\alpha=3^{\circ}$ , side view  
Figure 18. - Continued.



(c)  $\alpha=25^\circ$ , plan view  
Figure 18. - Continued.

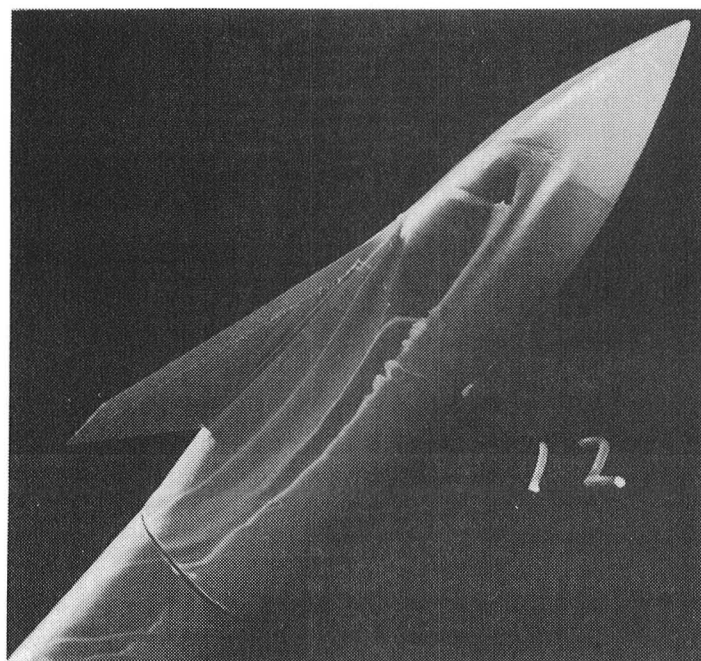


(d)  $\alpha=25^{\circ}$ , side view  
Figure 18.- Continued.

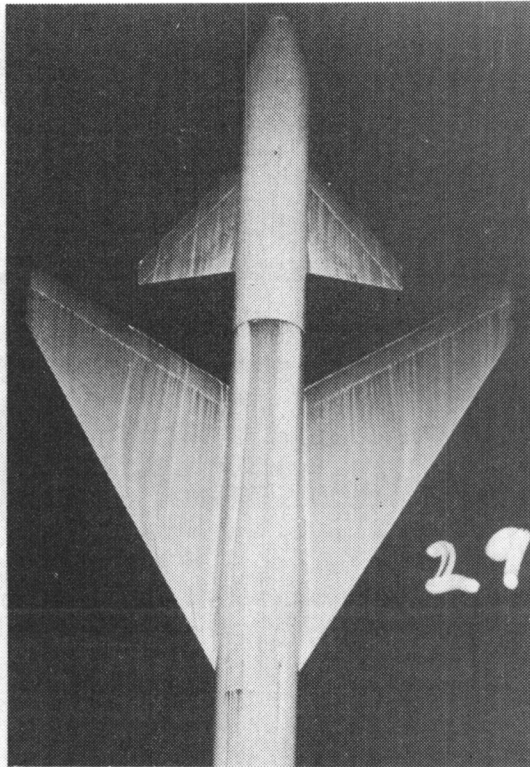


(e)  $\alpha=40^{\circ}$ , plan view  
Figure 18. - Continued.



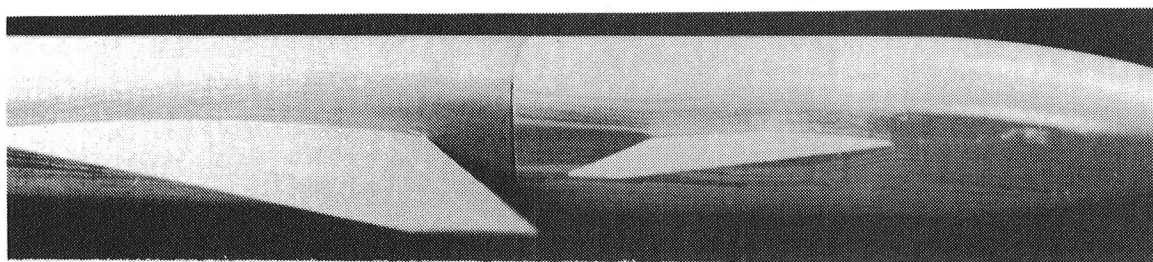


(f)  $\alpha=40^\circ$ , side view  
Figure 18. - Concluded.



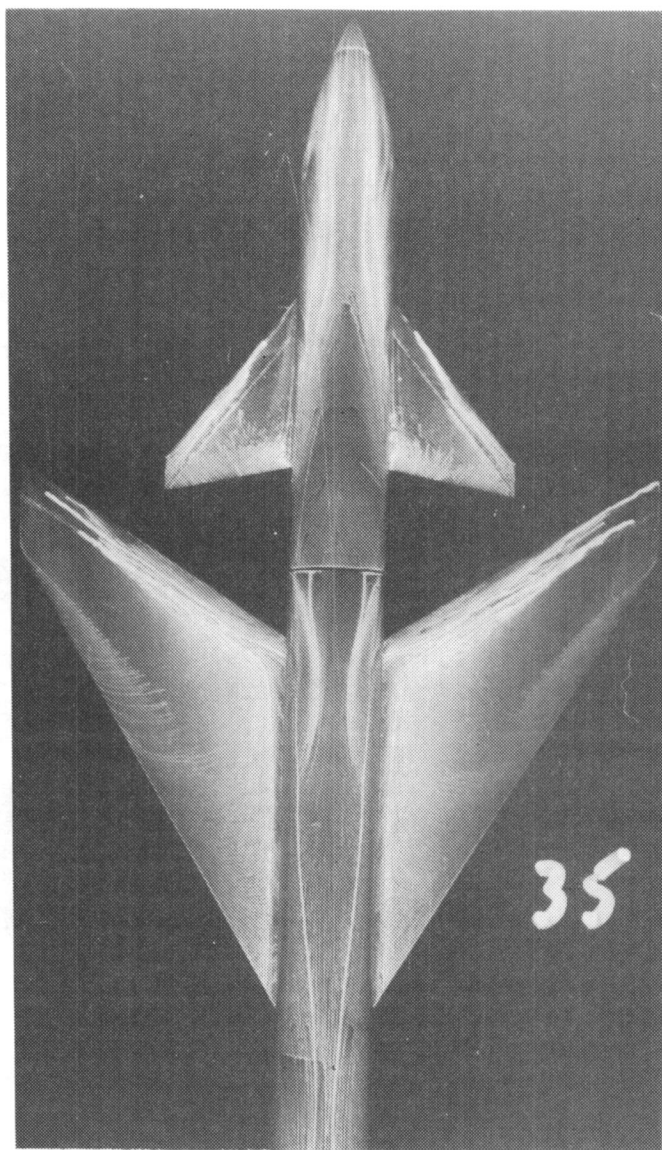
(a)  $\alpha=3^0$ , plan view

Figure 19. - Surface oil flow photographs of the mid-wing  
small size mid-canard configuration.  $M=0.3$ .

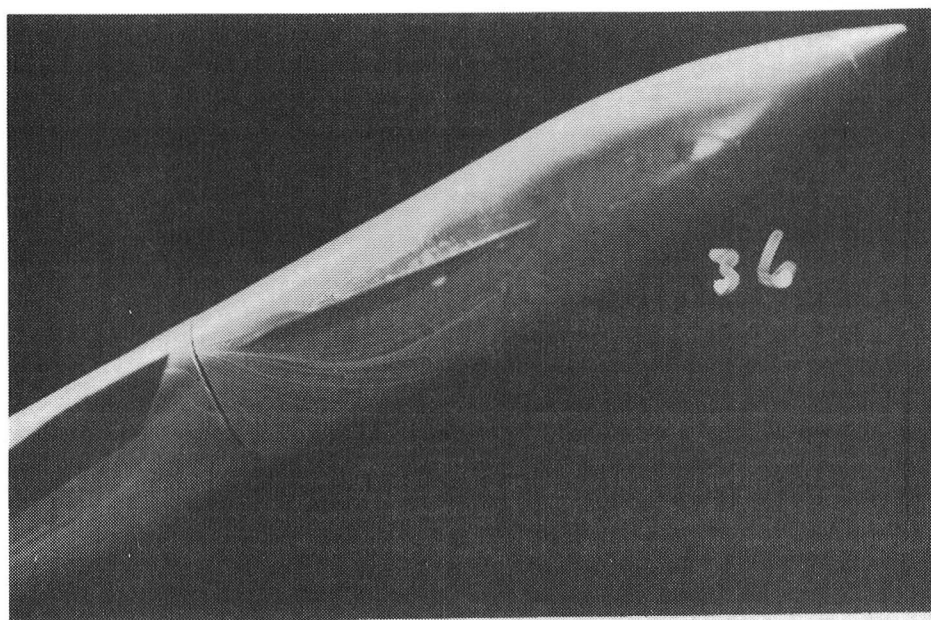


(b)  $\alpha=3^0$ , side view

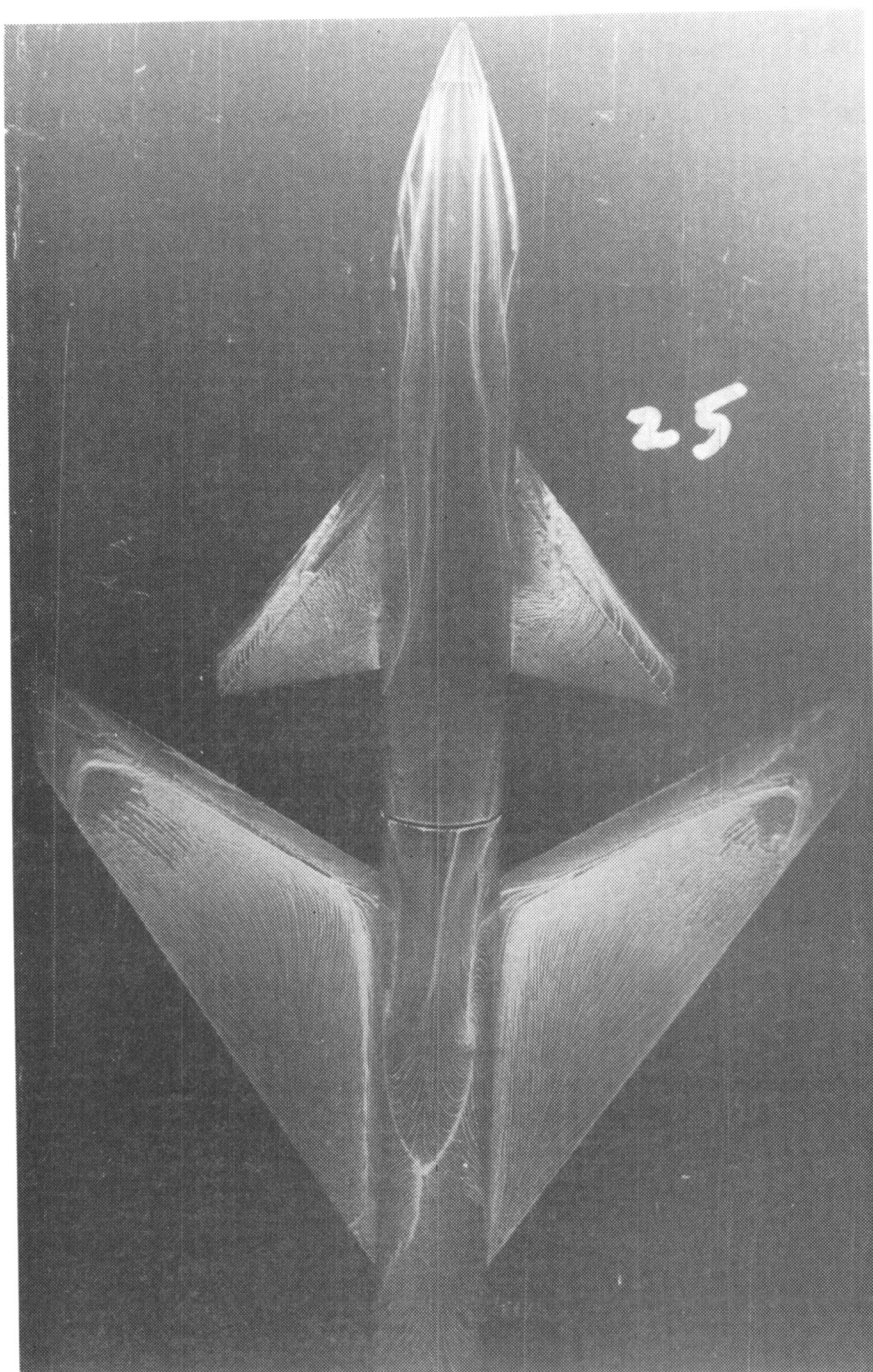
Figure 19. ~ Continued.



(c)  $\alpha=25^0$ , plan view  
Figure 19. - Continued.

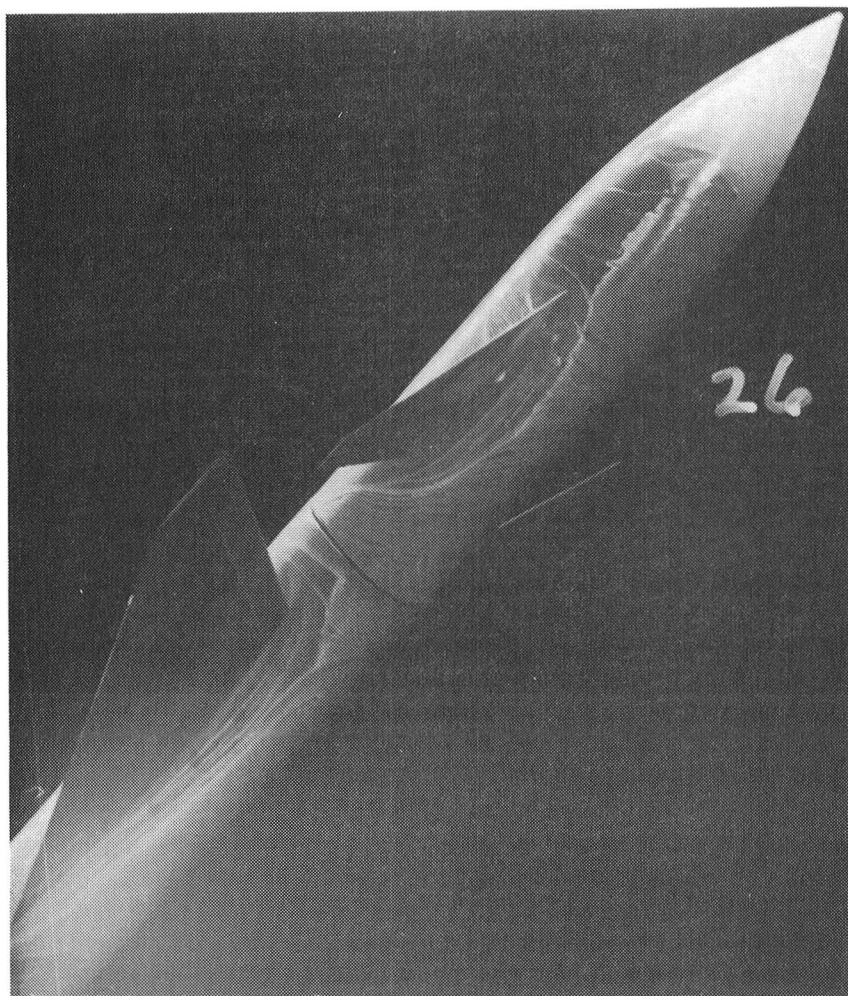


(d)  $\alpha=25^{\circ}$ , side view  
Figure 19. - Continued.

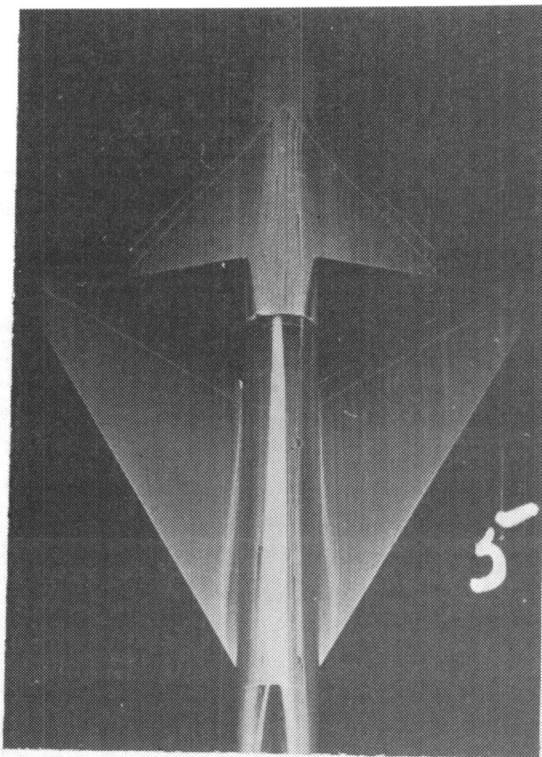


(e)  $\alpha=40^\circ$ , plan view  
Figure 19. - Continued.



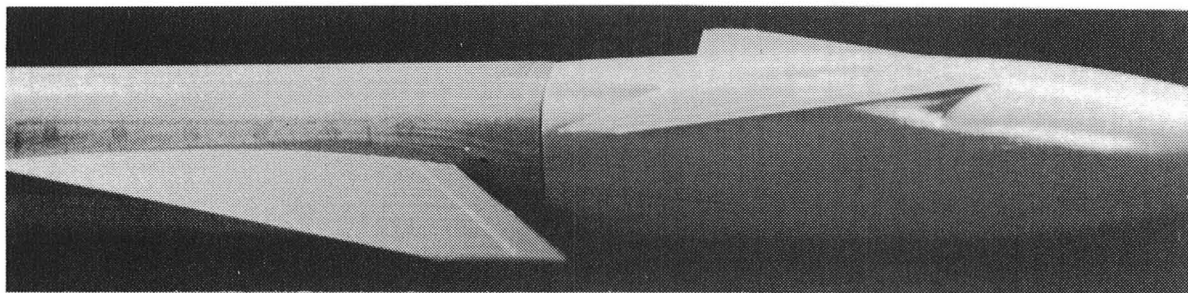


(f)  $\alpha=40^{\circ}$ , side view  
Figure 19. - Concluded.

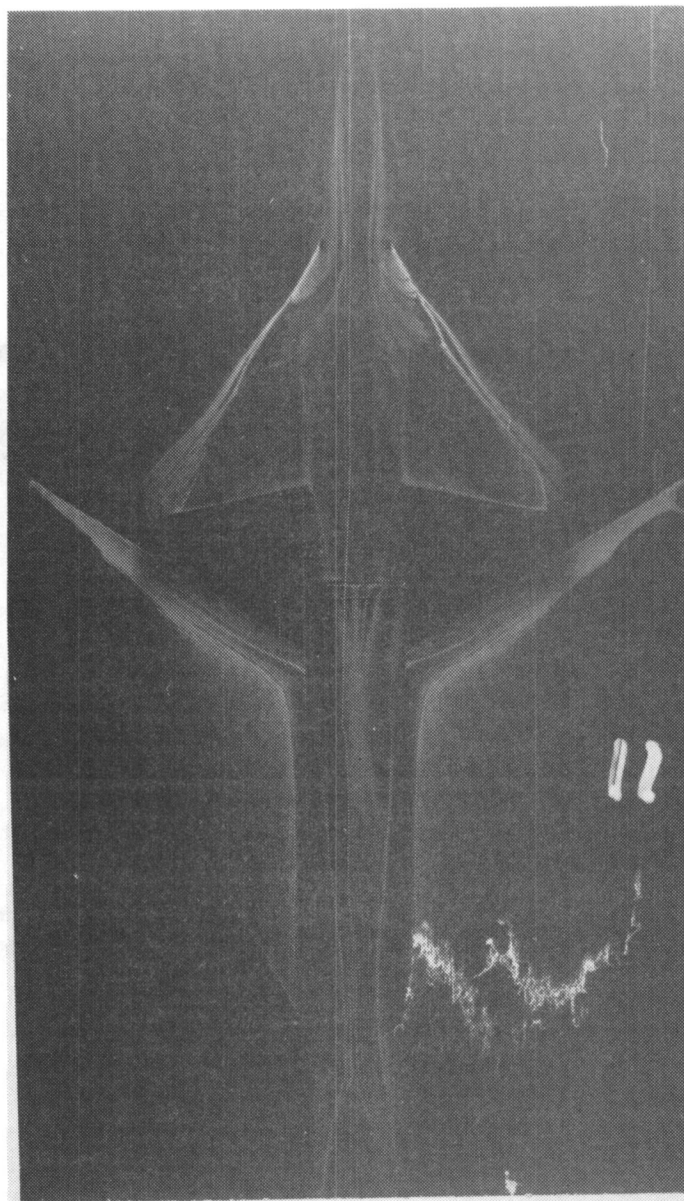


(a)  $\alpha=3^0$ , plan view

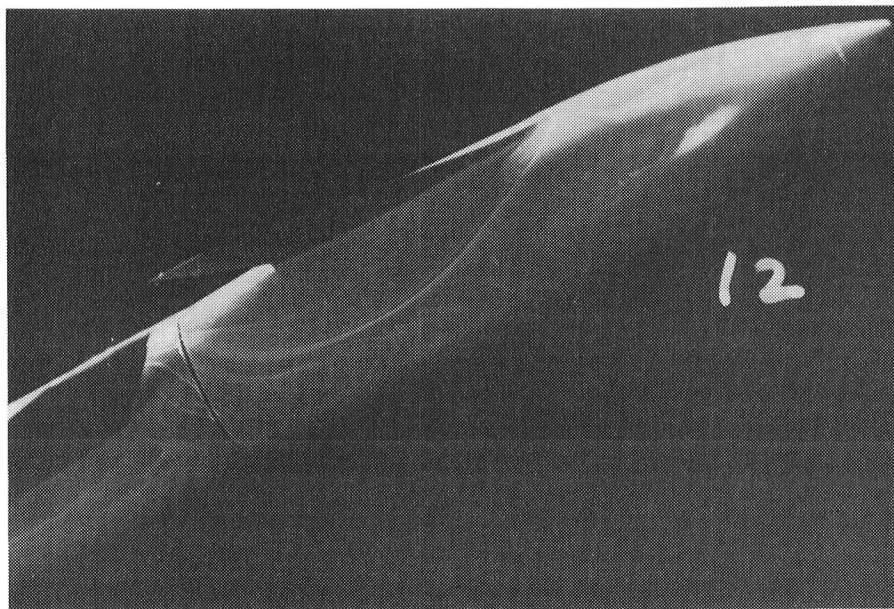
Figure 20.- Surface oil flow photographs of the mid-wing large size high-canard configuration.  $M=0.3$ .



(b)  $\alpha=3^{\circ}$ , side view  
Figure 20.- Continued.

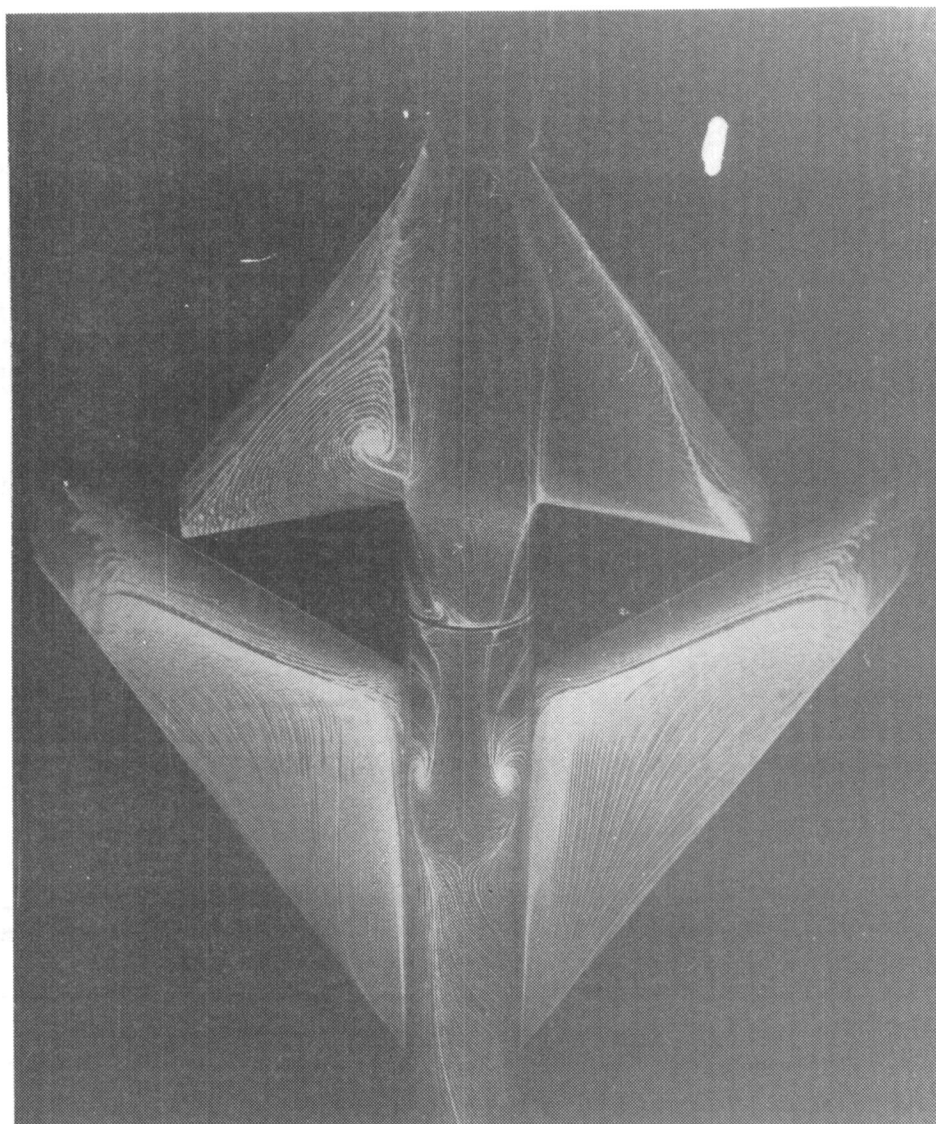


(c)  $\alpha=25^{\circ}$ , plan view  
Figure 20. - Continued.



(d)  $\alpha=25^\circ$ , side view  
Figure 20. - Continued.

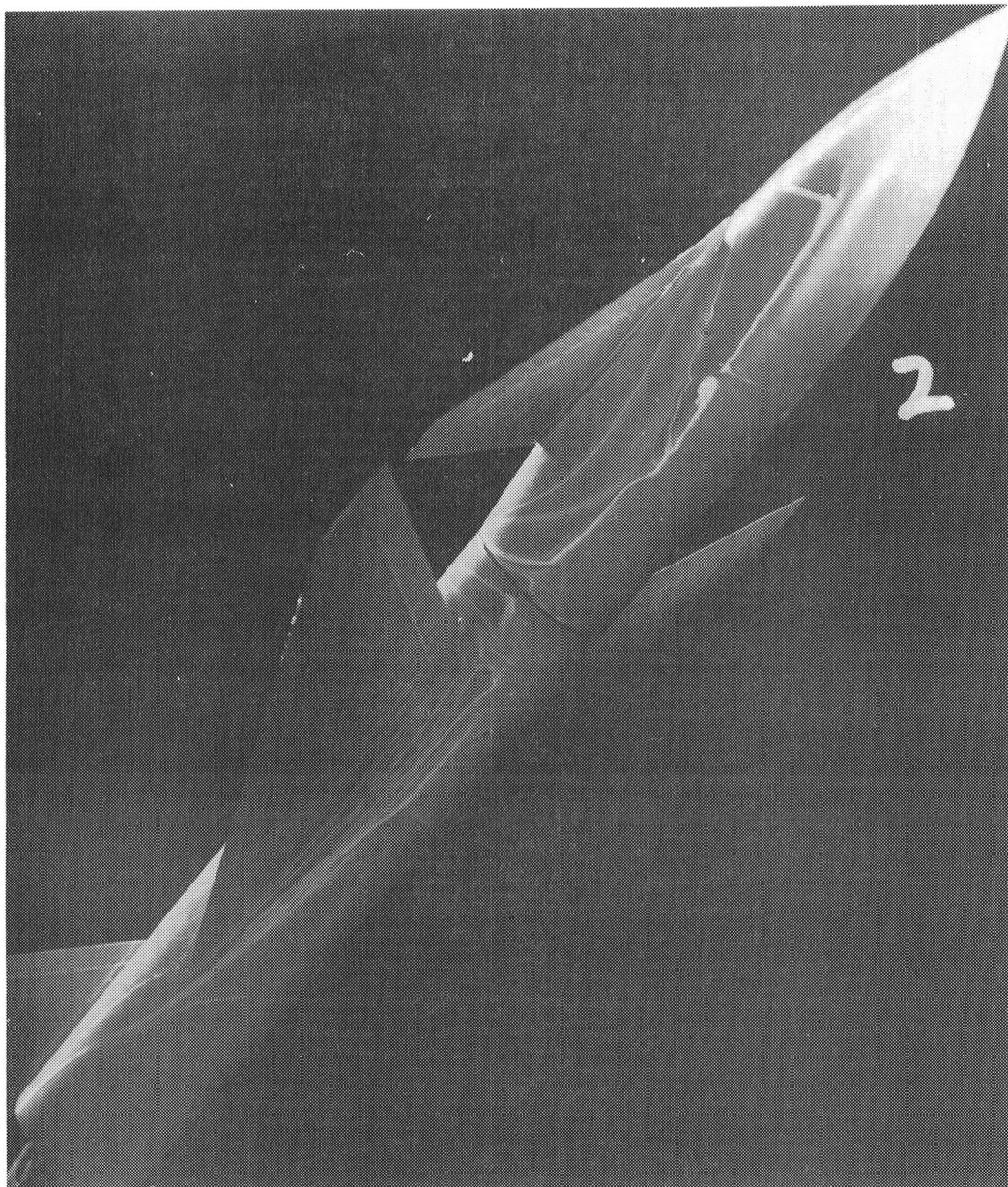




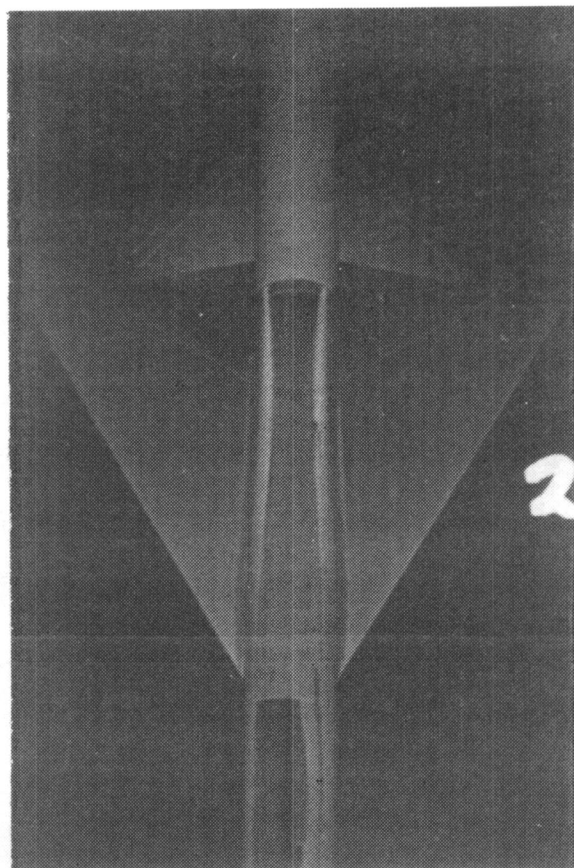
(e)  $\alpha=40^{\circ}$ , plan view

Figure 20. - Continued.



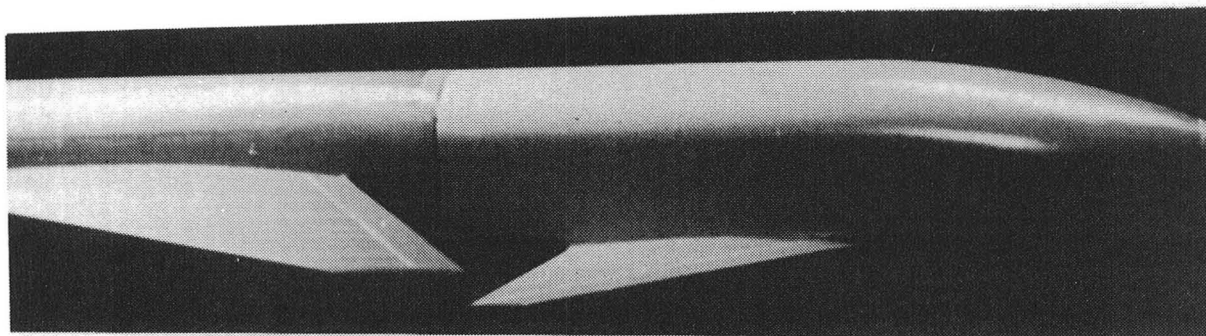


(f)  $\alpha=40^0$ , side view  
Figure 20.- Concluded.



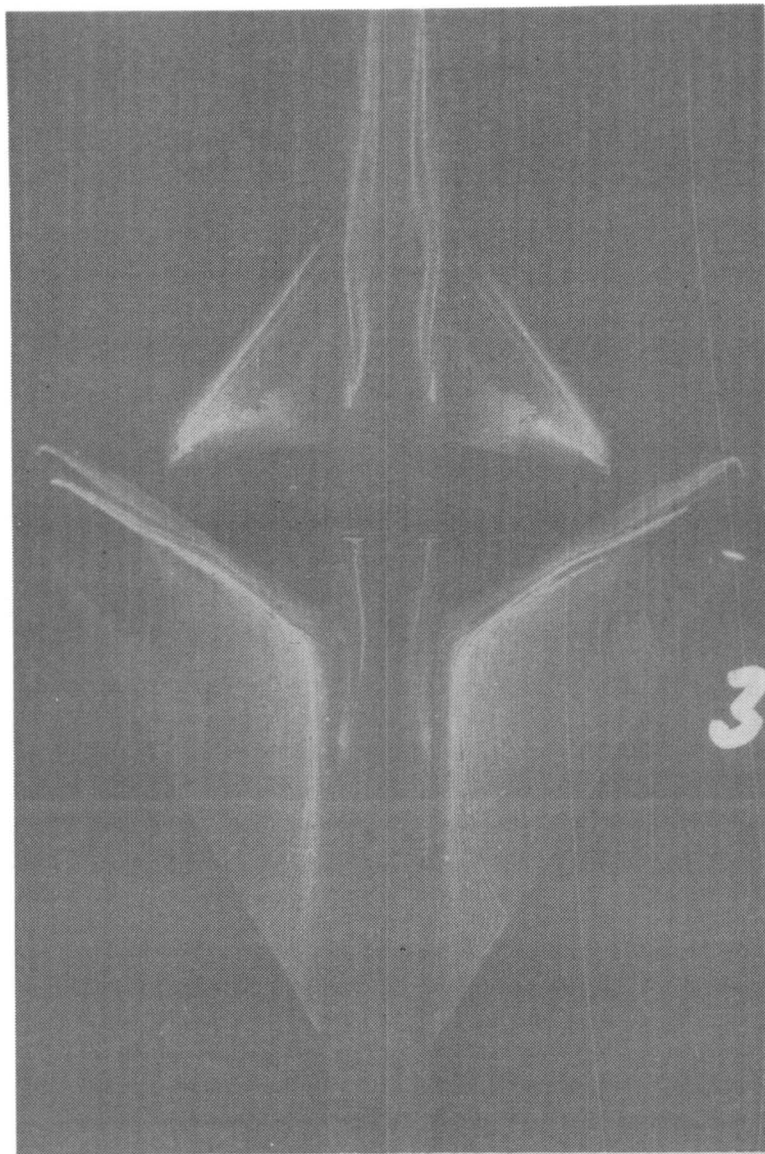
(a)  $\alpha=3^0$ , plan view

Figure 21.- Surface oil flow photographs of the mid-wing large size low-canard configuration.  $M=0.3$ .

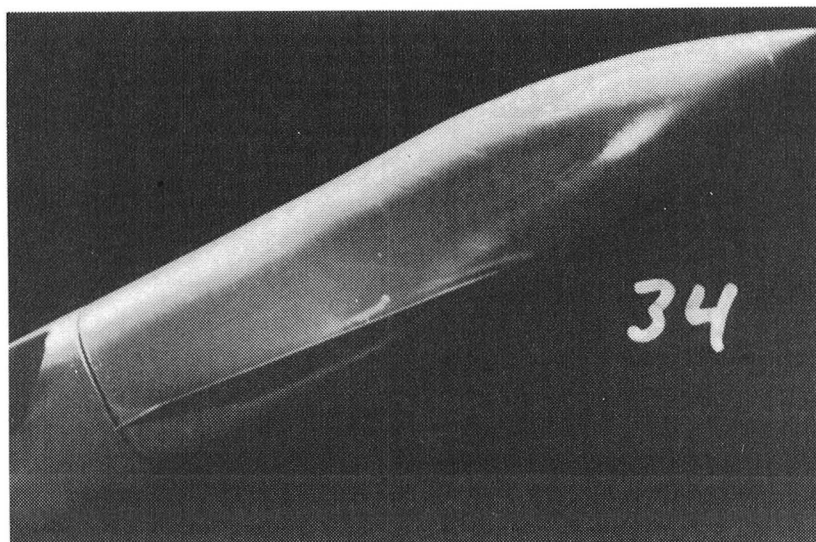


(b)  $\alpha=3^{\circ}$ , side view

Figure 21.- Continued.

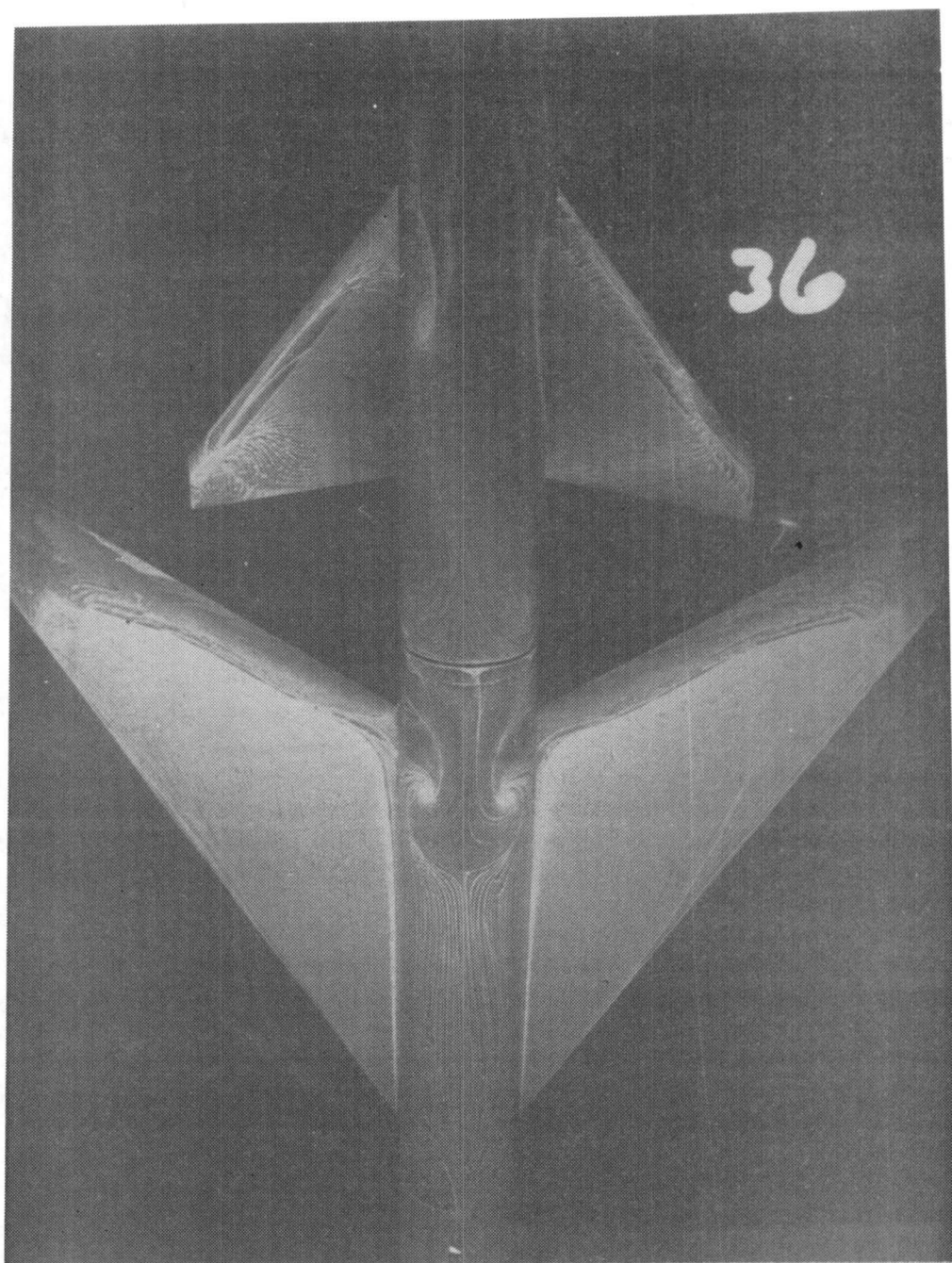


(c)  $\alpha=25^{\circ}$ , plan view  
Figure 21. - Continued.



(d)  $\alpha=25^{\circ}$ , side view  
Figure 21.- Continued.





(e)  $\alpha=40^{\circ}$ , plan view  
Figure 21. - Continued.





(f)  $\alpha=40^{\circ}$ , side view  
Figure 21. - Concluded.

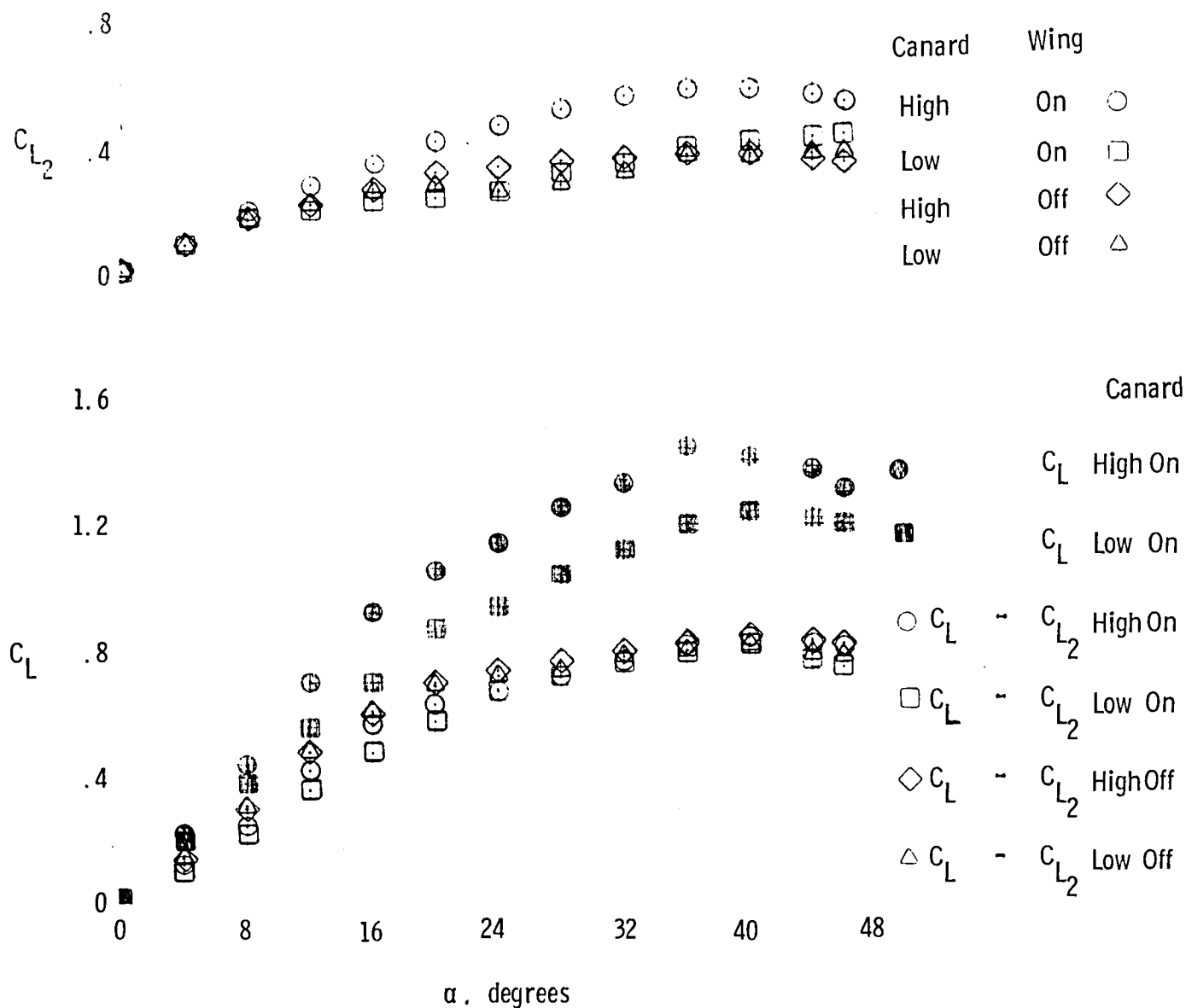


Figure 22.- Lift interference effect for the high and low canard position utilizing the medium size canard.



1. Report No. NASA TM-78739		2. Government Accession No.		3. Recipient's Catalog No.	
4. Title and Subtitle THE EFFECT OF CANARD RELATIVE SIZE AND VERTICAL LOCATION ON THE SUBSONIC LONGITUDINAL AND LATERAL-DIRECTIONAL STATIC AERODYNAMIC CHARACTERISTICS FOR A MODEL WITH A SWEEPED FORWARD WING				5. Report Date July 1979	
				6. Performing Organization Code	
7. Author(s) Jarrett K. Huffman and Charles H. Fox, Jr.				8. Performing Organization Report No.	
9. Performing Organization Name and Address NASA Langley Research Center Hampton, Virginia 23665				10. Work Unit No. 505-06-53-01	
				11. Contract or Grant No.	
12. Sponsoring Agency Name and Address National Aeronautics and Space Administration Washington, DC 20546				13. Type of Report and Period Covered Technical Memorandum	
				14. Sponsoring Agency Code	
15. Supplementary Notes					
16. Abstract A general research fighter model was tested in the Langley 7- by 10-foot high speed tunnel at a Mach number of 0.3. The model was tested with a 32° swept forward wing mounted in mid-, low-, and high-wing positions. For the mid-wing configuration, the model was tested with a 51.7° swept back canard mounted in mid-, low-, and high-canard positions. For the mid-wing mid-canard and the mid-wing high-canard configurations, canards of similar planform having two different areas were tested. The angle-of-attack range was from approximately -4° to 48° at sideslip angles of 0°, -5°, and 5°.					
17. Key Words (Suggested by Author(s)) Longitudinal aerodynamics Lateral-directional aerodynamics Close-coupled wing-canard Swept forward wing-canard Subsonic aerodynamics			18. Distribution Statement  Star Category - 02 Unclassified - Unlimited		
19. Security Classif. (of this report) Unclassified	20. Security Classif. (of this page) Unclassified	21. No. of Pages 104	22. Price* \$6.50		







